

This electronic thesis or dissertation has been downloaded from the King's Research Portal at <https://kclpure.kcl.ac.uk/portal/>



## **Motion Modelling for Respiratory Motion Estimation in Minimally Invasive Cardiac Interventions Using Intraprocedure Ultrasound Data**

Peressutti, Devis

*Awarding institution:*  
King's College London

The copyright of this thesis rests with the author and no quotation from it or information derived from it may be published without proper acknowledgement.

### **END USER LICENCE AGREEMENT**



**Unless another licence is stated on the immediately following page** this work is licensed

under a Creative Commons Attribution-NonCommercial-NoDerivatives 4.0 International

licence. <https://creativecommons.org/licenses/by-nc-nd/4.0/>

You are free to copy, distribute and transmit the work

Under the following conditions:

- Attribution: You must attribute the work in the manner specified by the author (but not in any way that suggests that they endorse you or your use of the work).
- Non Commercial: You may not use this work for commercial purposes.
- No Derivative Works - You may not alter, transform, or build upon this work.

Any of these conditions can be waived if you receive permission from the author. Your fair dealings and other rights are in no way affected by the above.

### **Take down policy**

If you believe that this document breaches copyright please contact [librarypure@kcl.ac.uk](mailto:librarypure@kcl.ac.uk) providing details, and we will remove access to the work immediately and investigate your claim.

KING'S COLLEGE LONDON

DOCTORAL THESIS

---

Motion Modelling for Respiratory  
Motion Estimation in Minimally  
Invasive Cardiac Interventions Using  
Intraprocedure Ultrasound Data

---

*Author:*

Devis PERESSUTTI

*Supervisors:*

Andrew P. KING, Ph.D.

Graeme P. PENNEY, Ph.D.

*A thesis submitted in fulfilment of the requirements  
for the degree of Doctor of Philosophy*

*in the*

Division of Imaging Sciences & Biomedical Engineering  
School of Medicine

February 2014

KING'S  
*College*  
LONDON

---

*“Prediction is very difficult, especially if it’s about the future.”*

Niels Bohr

*“The most exciting phrase to hear in science, the one that heralds new discoveries, is not ‘Eureka!’ but ‘That’s funny...’”*

Isaac Asimov

# *Abstract*

Respiratory motion of the heart limits the utility of image-guided cardiac interventions, causing misalignments between the pre-procedure information used for guidance and the intra-procedure moving anatomy and instruments. As a result, the guidance can be misleading, compromising the accuracy and success of the intervention. Respiratory motion models have been proposed to estimate and correct for respiratory motion, but to date their clinical uptake has been very limited due to a lack of accuracy and robustness, and the interruptions that they typically introduce into the clinical workflow. The scope of this project was to devise methods to address these limitations and foster the clinical translation of respiratory motion models.

A novel Bayesian respiratory motion model was developed in the first part of the project. The Bayesian framework enables the combination of the robustness of a pre-procedure motion model derived from Magnetic Resonance Imaging with the intra-procedure information provided by 3D echography (echo) images. The main novelties of the approach lie in its probabilistic formulation and its ability to adapt to variable breathing patterns. The Bayesian motion model was further evaluated using live 2D echo images, proving to be accurate using both 2D and 3D echo images. Furthermore, a new motion model-driven echo acquisition framework was developed to acquire 2D echo images that automatically compensates for respiratory motion.

The second part of the project addressed the limitations associated with the dynamic calibration scan used to derive the motion model, the acquisition of which causes interruptions to the clinical workflow. A personalisation framework for population-based motion models that uses anatomical features to predict cardiac respiratory motion was developed. Results show an average value for the 50<sup>th</sup> and 95<sup>th</sup> quantiles of the estimation error of 1.6mm and 4.7mm respectively, without the need for a subject-specific dynamic calibration scan.

Finally, the above mentioned parts were combined to produce a personalised Bayesian motion model. The technique is accurate and does not significantly complicate the clinical workflow, thus making it suitable for clinical uptake.



# *Acknowledgements*

I would like to express my deepest gratitude to Andy and Graeme. They have been perfect mentors, constantly guiding and supporting me during these years, and teaching me, besides most of the technical aspects, how to be a good scientist. It has been a great pleasure to work with them. I am very thankful to Andy for his constant presence and never ending patience, and I am glad that we will continue our collaboration in the future. I am also very grateful to Philip, my first contact at KCL, for taking into consideration my candidature.

In these years in the department of Biomedical Engineering, I have learnt most of the things I know about medical imaging, image acquisition and image processing and for this I have to thank all the people who helped me in this learning process, sharing their knowledge and experience. My thanks particularly go to Alberto, Chris Buerger, Christoph, Andy, Jack, Ghislain, Markus and Christian for their help and the inspiring talks we had in the department and in the pubs. I am very thankful to the clinical fellows and radiographers in the department for their precious help and very useful opinions. I had a wonderful time in the Division and for this I have to thank all the awesome people I was lucky to share my time with. In particular, I would like to thank Simo, Fedi, Cata and Nika for the best coffee breaks I had in my life. Special thanks go to Nika for bringing more happiness and love in my life.

I am very lucky to have met so many nice people in my life. I am grateful to Giulia, Massimo and Andrea, for making me feel home in London. I will always be grateful to Baba for being part of my life and for her continuous support in any decision I made. With her, I would like to thank Giacomo, Dario, Michele, i Cherubin, Patrizia, and Carlo for their love and affection. I can not forget to thank Freddy, Lucio, Cristian, Ale, Marco and Federico for keeping our friendship strong, regardless of the distance.

Finally, I want to thank my family. Nothing would have been possible without their infinite love, support and trust. A big thank you also goes to the readers. I hope you will enjoy the reading as much as I enjoyed these three years of my life.

Devis Peressutti, January 2014

# Contents

<b>Abstract</b>	<b>2</b>
<b>Acknowledgements</b>	<b>3</b>
<b>List of Figures</b>	<b>7</b>
<b>List of Tables</b>	<b>9</b>
<b>Abbreviations</b>	<b>10</b>
<b>1 Introduction</b>	<b>13</b>
1.1 Motivation . . . . .	13
1.2 Contributions . . . . .	14
1.3 Outline . . . . .	16
<b>2 Clinical Background</b>	<b>18</b>
2.1 Respiratory Motion . . . . .	18
2.1.1 Respiratory Motion Variability . . . . .	19
2.1.2 Cardiac Respiratory Motion . . . . .	21
2.2 Image-Guided Interventions . . . . .	23
2.2.1 Imaging Technology . . . . .	25
2.2.2 Cardiac Image-Guided Interventions . . . . .	27
2.3 Discussion . . . . .	30
<b>3 Respiratory Motion Modelling</b>	<b>32</b>
3.1 Building and Applying Respiratory Motion Models . . . . .	33
3.2 Subject-Specific Respiratory Motion Modelling . . . . .	36
3.2.1 Modelling of Respiratory Motion Variability . . . . .	39
3.2.2 Echo Image-Driven Modelling . . . . .	44
3.3 Population-Based Respiratory Motion Modelling . . . . .	44
3.4 Discussion . . . . .	45
<b>4 Subject-Specific Bayesian Respiratory Motion Model</b>	<b>48</b>
4.1 Introduction . . . . .	49
4.2 Methods . . . . .	50

4.2.1	Overview . . . . .	50
4.2.2	Bayesian Motion Estimation . . . . .	51
4.2.3	Prior Probability . . . . .	51
4.2.4	Likelihood . . . . .	54
4.2.5	Optimisation of $\sigma_l^2$ . . . . .	55
4.3	Experiments . . . . .	56
4.3.1	MRI Acquisition . . . . .	56
4.3.2	Comparison of Estimation Techniques . . . . .	57
4.3.3	Evaluation Using Real MRI, Simulated Echo Data . . . . .	61
4.3.4	Evaluation Using Real MRI, Real Echo Data . . . . .	63
4.3.5	Determination of the Optimal $\sigma_l^2$ . . . . .	65
4.4	Results . . . . .	67
4.4.1	Simulated Echo Data . . . . .	67
4.4.2	Real Echo Data . . . . .	68
4.5	Discussion . . . . .	73
<b>5</b>	<b>Motion Model Guidance of Echo Imaging Acquisition</b>	<b>77</b>
5.1	Introduction . . . . .	77
5.2	Method . . . . .	78
5.2.1	Respiratory Motion Model . . . . .	79
5.2.2	Model-Driven Image Acquisition . . . . .	79
5.2.3	Bayesian Motion Estimation . . . . .	80
5.3	Evaluation . . . . .	81
5.3.1	Materials . . . . .	81
5.3.2	Evaluation Approach . . . . .	83
5.4	Results . . . . .	85
5.5	Discussion . . . . .	87
<b>6</b>	<b>Personalising Population-Based Respiratory Motion Models using Learnt Anatomical Features</b>	<b>89</b>
6.1	Introduction . . . . .	90
6.2	Overview . . . . .	91
6.3	Materials . . . . .	92
6.4	Methods . . . . .	93
6.4.1	Average Shape Atlas . . . . .	93
6.4.2	Motion Estimates in Atlas Space . . . . .	94
6.4.3	Quantifying Motion Similarity . . . . .	95
6.4.4	Neighbourhood Approximation . . . . .	97
6.4.5	Personalisation . . . . .	99
6.5	Experiments . . . . .	100
6.5.1	Evaluation of Estimation Accuracy . . . . .	101
6.5.2	Evaluation of Correlation Hypothesis . . . . .	102
6.6	Results . . . . .	103
6.6.1	Estimation accuracy . . . . .	103
6.6.2	Correlation hypothesis . . . . .	104
6.7	Discussion . . . . .	105

---

<b>7</b>	<b>Personalised Bayesian Respiratory Motion Model</b>	<b>110</b>
7.1	Introduction . . . . .	110
7.2	Method . . . . .	111
7.2.1	Personalisation . . . . .	112
7.2.2	Bayesian Motion Estimation . . . . .	113
7.3	Evaluation . . . . .	114
7.3.1	Materials . . . . .	114
7.3.2	Experiments . . . . .	115
7.4	Results . . . . .	117
7.5	Discussion . . . . .	119
<b>8</b>	<b>Conclusions</b>	<b>121</b>
8.1	Summary . . . . .	121
8.2	Clinical Impact . . . . .	123
8.3	Current Limitations and Future Directions . . . . .	124
8.4	Conclusions . . . . .	127
<b>A</b>	<b>Data Acquisition</b>	<b>128</b>
A.1	MRI Acquisition . . . . .	128
A.2	Echo Acquisition . . . . .	129
A.3	Datasets . . . . .	131
<b>B</b>	<b>Neighbourhood Approximation Forest</b>	<b>133</b>
	<b>Bibliography</b>	<b>135</b>

# List of Figures

2.1	Hysteresis effect . . . . .	20
2.2	Example of cardiac pre-procedure image and segmentation . . . . .	28
2.3	Example of pre- and intra-procedure imaging registration . . . . .	30
3.1	Subject-specific direct correspondence respiratory motion model . . . . .	34
3.2	Subject-specific indirect correspondence respiratory motion model . . . . .	35
3.3	Population-based direct correspondence motion model . . . . .	47
4.1	Schematic representation of the Bayesian motion estimation . . . . .	50
4.2	Example of Gaussian distribution function for the AP translation . . . . .	53
4.3	Overview of the echo simulation and leave-one-out validation framework . . . . .	59
4.4	Workflow employed to evaluate the technique on real echo imaging data . . . . .	60
4.5	Example of simulated and live 3D echo images . . . . .	64
4.6	Example of evaluation assessment using GIMIAS . . . . .	65
4.7	Distribution of the best values of $\sigma_l^2$ as a function of $SNR_d$ . . . . .	66
4.8	Comparison of motion estimation accuracy for simulated echo images . . . . .	67
4.9	Comparison of motion estimation accuracy for real echo images . . . . .	69
4.10	Example of unrealistic motion estimate . . . . .	70
4.11	Comparison of respiratory motion estimates . . . . .	71
5.1	Overview of the automatic model-driven echo acquisition . . . . .	79
5.2	Example of 3D echo images used for evaluation . . . . .	82
5.3	Block diagram of the evaluation approach . . . . .	83
5.4	Examples of imaging planes and selected points . . . . .	84
6.1	Overview of the personalisation framework for population-based motion models . . . . .	92
6.2	Example of average shape atlas in its natural coordinate system . . . . .	95
6.3	Example of anatomical features . . . . .	98
6.4	Toy example of binary tree training of the Neighbourhood Approximation Forest . . . . .	98
6.5	Estimation accuracy results . . . . .	104
6.6	Correlation hypothesis results . . . . .	106
6.7	Comparison of cardiac features most correlated to similarities in anatomy and respiratory motion . . . . .	107
7.1	Overview of the personalised Bayesian respiratory motion estimation . . . . .	112
7.2	Overview of the evaluation approach . . . . .	116

---

7.3	Example of probability distribution functions of the AP translation . . .	117
A.1	Acquisition setup for live 3D echo images . . . . .	130

# List of Tables

2.1	Typical values of cardiac respiratory motion. . . . .	22
2.2	Imaging modalities in IGIs . . . . .	26
3.1	Key papers on subject-specific respiratory motion modelling . . . . .	38
3.2	Key papers on population-based respiratory motion modelling . . . . .	47
4.1	Values of the acoustic impedance $Z$ and absorption coefficient $\alpha$ used for simulating B-mode echo images. . . . .	62
4.2	Evaluation results of Bayesian estimation using simulated echo images .	72
4.3	Evaluation results of Bayesian estimation using real echo images . . . .	72
5.1	Results of the estimation accuracy evaluation . . . . .	86
6.1	Leave-one-out results for the estimation accuracy experiment . . . . .	104
6.2	Leave-one-out results for the correlation hypothesis experiment . . . . .	105
7.1	Results of the evaluation of estimation accuracy . . . . .	118
A.1	Details of the datasets employed in this thesis . . . . .	132

# Abbreviations

<b>1D</b>	One <b>D</b> imensional
<b>2D</b>	Two <b>D</b> imensional
<b>3D</b>	Three <b>D</b> imensional
<b>4D</b>	Four <b>D</b> imensional
<b>AF</b>	<b>A</b> trial <b>F</b> ibrillation
<b>AP</b>	<b>A</b> ntero- <b>P</b> osterior
<b>B-Mode</b>	<b>B</b> rightness <b>M</b> ode
<b>CMRA</b>	<b>C</b> ardiac <b>M</b> agnetic <b>R</b> esonance <b>A</b> ngiography
<b>CO<sub>2</sub></b>	<b>C</b> arbon <b>D</b> ioxide
<b>CT</b>	<b>C</b> omputed <b>T</b> omography
<b>ECG</b>	<b>E</b> lectrocardiogram
<b>Echo</b>	<b>E</b> chography, <b>ech</b> ocardiography
<b>EP</b>	<b>E</b> lectrophysiology
<b>EPI</b>	<b>E</b> cho <b>P</b> lanar <b>I</b> maging
<b>FFD</b>	<b>F</b> ree- <b>F</b> orm <b>D</b> eformation
<b>FoV</b>	<b>F</b> ield of <b>V</b> iew
<b>GT</b>	<b>G</b> round <b>T</b> ruth
<b>IGI(s)</b>	<b>I</b> mage- <b>G</b> uided <b>I</b> ntervention(s)
<b>LR</b>	<b>L</b> eft- <b>R</b> ight
<b>LV</b>	<b>L</b> eft <b>V</b> entricle
<b>MAP</b>	<b>M</b> aximum <b>A</b> <b>P</b> osteriori
<b>ML</b>	<b>M</b> edio <b>L</b> ateral
<b>MRI</b>	<b>M</b> agnetic <b>R</b> esonance <b>I</b> maging
<b>NAF</b>	<b>N</b> eighbourhood <b>A</b> pproximation <b>F</b> orest
<b>NCC</b>	<b>N</b> ormalised <b>C</b> ross <b>C</b> orrelation



---

<b>O<sub>2</sub></b>	<b>O</b> xigen
<b>PC(s)</b>	<b>P</b> rincipal <b>C</b> omponent(s)
<b>PCA</b>	<b>P</b> rincipal <b>C</b> omponent <b>A</b> nalysis
<b>PET</b>	<b>P</b> ositron <b>E</b> mission <b>T</b> omography
<b>PLSR</b>	<b>P</b> artial <b>L</b> east <b>S</b> quares <b>R</b> egression
<b>RF</b>	<b>R</b> adio <b>F</b> requency
<b>RT</b>	<b>R</b> adiotherapy
<b>RXA</b>	<b>R</b> otational <b>X</b> -ray <b>A</b> ngiography
<b>SI</b>	<b>S</b> upero- <b>I</b> nferior
<b>SNR</b>	<b>S</b> ignal-to- <b>N</b> oise <b>R</b> atio
<b>SVD</b>	<b>S</b> ingular <b>V</b> alue <b>D</b> ecomposition
<b>TE</b>	<b>E</b> cho <b>T</b> ime
<b>TFE</b>	<b>T</b> urbo <b>F</b> ield <b>E</b> cho
<b>TFEPI</b>	<b>T</b> urbo <b>F</b> ield <b>E</b> cho <b>P</b> lanar <b>I</b> maging
<b>TR</b>	<b>R</b> epetition <b>T</b> ime
<b>TOE</b>	<b>T</b> ransoesophageal <b>E</b> cho
<b>TRE</b>	<b>T</b> arget <b>R</b> egistration <b>E</b> rror
<b>TTE</b>	<b>T</b> ransthoracic <b>E</b> cho
<b>US</b>	<b>U</b> ltrasound

*To my family.*

# Chapter 1

## Introduction

### Contents

---

<b>1.1 Motivation . . . . .</b>	<b>13</b>
<b>1.2 Contributions . . . . .</b>	<b>14</b>
<b>1.3 Outline . . . . .</b>	<b>16</b>

---

### 1.1 Motivation

The aim of image-guided interventions (IGIs) on the heart is to provide the surgeon with accurate information about the location of catheters and instruments in relation to the chambers and vessels of the heart. This can be achieved by combining pre-procedure high resolution images of the heart of the subject, normally derived from Magnetic Resonance Imaging (MRI) or Computed Tomography (CT), with intra-procedure real-time imaging.

A major drawback to the use of cardiac IGIs is the respiratory motion of the heart. Respiratory motion causes misalignments between the static pre-procedure images used for guidance and the underlying moving anatomy, resulting in misleading guidance information that can affect the success of the intervention. As will be detailed later on, misalignments due to respiratory motion are subject-specific and can range up to  $30mm$  or more. Respiratory motion is often assumed to be periodic, but is in fact more complex than this, and varies with intra- and inter-cycle variability. Therefore, estimation of respiratory motion is a challenging task.

Respiratory motion modelling techniques have been proposed to estimate and compensate for respiratory motion in image acquisition and IGIs. However, there has been

very limited clinical translation of these techniques. A likely reason for this lack of translation is a lack of accuracy and robustness of the techniques proposed to date. For example, many techniques fail to adequately cope with the complex variability in respiratory motion. A second reason is that the most accurate motion models currently available require the acquisition of a dynamic calibration scan prior to the intervention to estimate and model the subject-specific respiratory motion. Such dynamic calibration scans interrupt and complicate the clinical workflow, and often cannot be acquired at all.

This thesis seeks to address the current limitations of respiratory motion modelling techniques to foster the uptake of such techniques in clinical practice. To achieve this goal, novel and effective methods have been devised first, to improve the accuracy and robustness of the motion model estimates, and second, to obviate the need for a dynamic calibration scan in the clinical workflow. An overview of the original contributions introduced in this thesis is presented in the next Section.

## 1.2 Contributions

The original contributions of this thesis to the field of respiratory motion modelling can be summarised as follows:

**Accuracy improvement.** Technological advances are leading to increased availability of real-time imaging which can be used during interventions. In particular, advances in 3D echo technology and its relatively low cost have resulted in a real-time, non-ionising 3D imaging modality suitable for intra-procedure guidance. However, for a number of cardiac interventions, echo imaging is not typically of high enough quality to use for guidance on its own, but is nevertheless a rich source of real-time information about organ motion. This opens up the possibility of incorporating echo data into a respiratory motion modelling framework, enabling it to better cope with complex motion variability. To date, a sound theoretical framework to base the incorporation of echo data into a respiratory motion model has been lacking. This thesis presents such a framework. A novel Bayesian approach for subject-specific motion estimation is presented, which is able to produce more accurate motion estimates using a pre-procedure motion model and intra-procedure echo data. The Bayesian motion estimates can be used

intra-operatively to update the position of pre-procedure data, thus maintaining the accuracy of the guidance. The technique uses a probabilistic formulation to combine the robustness of a subject-specific MRI-derived motion model with the real-time information provided by intra-procedure echo imaging. The probabilistic formulation allows incorporation of a measure of uncertainty into the modelling process, and the uncertainty is subsequently resolved by the real-time intra-procedure echo images. Furthermore, the Bayesian motion estimation is able to model and estimate the complex variability in respiratory motion. In this thesis, the technique is evaluated using 3D and 2D echo images acquired from healthy volunteers. Results show the motion estimates to be more accurate than previously published state-of-the-art techniques. To further improve the estimation accuracy of the Bayesian motion estimation using intra-procedure 2D echo images, a novel motion model-driven echo acquisition framework is proposed. The model-driven echo acquisition allows the automatic acquisition of 2D echo images which are compensated for respiratory motion.

**Clinical workflow impact.** A major limitation of subject-specific respiratory motion models is the need to acquire the dynamic calibration scan used to estimate and model the respiratory motion prior to the intervention. The acquisition of this scan is often impractical, complicating the clinical workflow. In some cases, the acquisition is not possible at all, due to subject considerations, acquisition time and costs. To overcome the need for this scan, a novel personalisation framework for population-based motion models is proposed. The proposed personalised motion model is able to produce accurate respiratory motion estimates using information about the static cardiac anatomy of the subject only. The personalised motion model estimates are, for some subjects, as accurate as subject-specific motion model estimates with no need for a subject-specific dynamic calibration scan.

The next Section outlines how this thesis is organised and where each proposed method is described and evaluated.

### 1.3 Outline

The thesis is organised in 8 Chapters. Chapter 2 provides clinical background on respiratory motion and image-guided interventions, focusing in particular on the heart. Respiratory motion modelling techniques are presented and reviewed in Chapter 3. The novel methods proposed in this thesis are presented in Chapters 4, 5, 6 and 7. Chapter 8 provides a summary of the contributions with particular focus on their potential clinical impact as well as future directions.

Each Chapter is organised as follows:

**Chapter 2** introduces the physiology of respiratory motion, describing the main characteristics of the respiratory motion of the heart. In the second part of the Chapter, clinical background on image-guided interventions is provided, presenting aims and state-of-the-art techniques. The objective of this Chapter is to provide a clear description of the problem that this thesis seeks to address, namely the estimation and compensation of respiratory motion during IGIs on the heart.

**Chapter 3** provides an overview of currently available techniques for respiratory motion estimation and compensation in image acquisition and IGIs, focusing on respiratory motion modelling techniques. The most relevant works on respiratory motion modelling proposed in the literature are reviewed, emphasising the key contribution of each work. The scope of this Chapter is to provide background knowledge on the topic and to highlight the limitations of respiratory motion models proposed to date that this thesis seeks to overcome.

**Chapter 4** presents the novel subject-specific Bayesian respiratory motion model. The technique aims to address the lack of accuracy and robustness of state-of-the-art motion estimation techniques. In this Chapter, live 3D echo images are employed to resolve the uncertainty in motion estimation. Detailed explanation of the method and an extensive accuracy evaluation are provided.

**Chapter 5** presents further evaluation of the subject-specific Bayesian motion model, but employing live 2D echo images instead of 3D images. In addition, for the first time, a framework is proposed for using a respiratory motion model to automatically guide the acquisition of the intra-procedure 2D echo images. The resulting

motion model estimates are more accurate due to the partial compensation for respiratory motion provided by the model-driven acquisition.

**Chapter 6** presents the novel personalisation framework for population-based respiratory motion models. This framework is applicable to any organ affected by respiratory motion, although this Chapter presents results on the respiratory motion of the heart. The personalisation framework selects a subset of subjects from the population sample that is more likely to represent the cardiac respiratory motion of the subject under investigation. The selection is based on static cardiac anatomical features only and uses a neighbourhood approximation technique to learn the correlation of these features with cardiac respiratory motion. This is the first work that has investigated the hypothesis of correlation between the anatomy and position of the heart and its motion due to respiration.

**Chapter 7** presents an accurate and robust Bayesian respiratory motion model that does not employ a subject-specific dynamic calibration scan. The method presented in this Chapter combines the novel techniques proposed in Chapter 4 and Chapter 6. The resulting method is a proof of principle that demonstrates how accurate and robust respiratory motion estimates can be made using intra-procedure echo imaging with no significant interruptions to the clinical workflow.

**Chapter 8** summarises the main contributions presented in this thesis and describes some limitations of the proposed methods. Moreover, a discussion on the clinical impact of the methods is provided along with an overview of future directions. Finally, conclusions are drawn.

A detailed description of the data acquired and used to evaluate the methods proposed in this thesis is provided in Appendix A.

## Chapter 2

# Clinical Background

### Contents

---

<b>2.1</b>	<b>Respiratory Motion . . . . .</b>	<b>18</b>
2.1.1	Respiratory Motion Variability . . . . .	19
2.1.2	Cardiac Respiratory Motion . . . . .	21
<b>2.2</b>	<b>Image-Guided Interventions . . . . .</b>	<b>23</b>
2.2.1	Imaging Technology . . . . .	25
2.2.2	Cardiac Image-Guided Interventions . . . . .	27
<b>2.3</b>	<b>Discussion . . . . .</b>	<b>30</b>

---

This Chapter provides background on respiratory motion and IGIs. The physiology of respiratory motion is introduced in Section 2.1, while the concepts of variability in respiratory motion are presented in Section 2.1.1. Details of the respiratory motion of the heart are reported in Section 2.1.2. IGIs for minimally invasive procedures are introduced in Section 2.2, describing a typical clinical framework, along with the imaging modalities commonly employed (Section 2.2.1). Section 2.2.2 presents some applications of IGIs on the heart. Section 2.3 summarises key concepts and issues that this work seeks to address.

## 2.1 Respiratory Motion

The process of respiration occurs mainly in the lungs, where oxygen ( $O_2$ ) and carbon dioxide ( $CO_2$ ) are exchanged between air and blood, keeping the partial pressure of



$O_2$  and  $CO_2$  in the alveolar arteries at a constant level. The circulating blood supplies  $O_2$  to the body, removing the excess  $CO_2$  (Hicks, 2000; Keall et al., 2006).

The respiratory cycle consist of the inhalation and exhalation phases. Defining as alveolar pressure the pressure within the alveoli of the lungs, during inhalation fresh air flows into the lungs as a consequence of a negative alveolar pressure relative to the atmospheric pressure, and  $O_2$  and  $CO_2$  are exchanged; during exhalation, a positive alveolar pressure relative to the atmospheric pressure causes the air in the lungs to flow out. The changes in alveolar pressure are caused by changes in the lung volume, as a result of muscle activity. Several muscles are involved in normal inhalation, the main one being the diaphragm. As the diaphragm contracts, it moves in a predominantly inferior direction, with some anterior motion, increasing the volume of the lungs. This breathing motion is referred to as abdominal breathing. Other muscles normally involved are the intercostal muscles, which connect adjacent ribs of the thorax. During inhalation, intercostal muscles also contract, increasing the thorax volume in the antero-posterior (AP) and medio-lateral (ML) directions. This is referred to as chest breathing. Exhalation at rest is normally a passive process, while active exhalation also involves the activation of muscles in the abdomen and back. The *functional residual capacity* denotes the lung volume at the end of exhale and represents an equilibrium state which is the most relaxed. It is also the most repeatable in terms of the position of the organs affected by respiration. Therefore, as detailed later on, end-exhale is commonly used for respiratory gating in image acquisition and image-guided treatments.

### 2.1.1 Respiratory Motion Variability

In this Section, a brief description of variability in respiratory motion is provided, since the novel methods proposed in this thesis aim at modelling such variability.

#### Intra-cycle Variability

Defining the intra-pleural pressure as the pressure in the pleural cavity, which is the space between the layers of the membrane lining the lung and the chest, the transpulmonary pressure can be defined as the difference between the alveolar pressure and the intra-pleural pressure. The relationship between transpulmonary pressure and lung

volume changes from exhalation to inhalation. This characteristic is known as *hysteresis* and hereafter is referred to as *intra-cycle variability*, emphasising the difference in respiratory mechanisms during exhalation and inhalation. As shown in Figure 2.1(a), the difference in pressure/volume curves (a.k.a. compliance) is due to the additional energy required during inhalation to inflate more alveoli (Escolar and Escolar, 2004). Furthermore, the time employed to breathe in is normally longer than the time to breathe out. As a consequence, the respiratory motion of organs in the chest and abdomen varies between the exhalation and the inhalation phases (see Figure 2.1(b)).

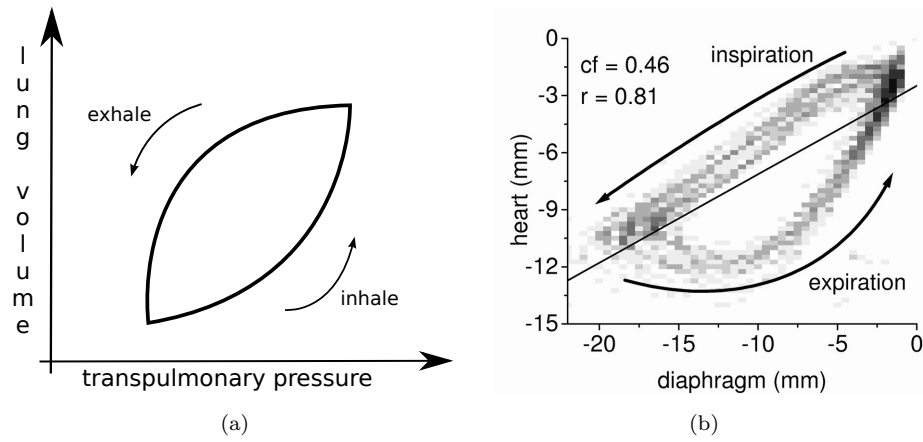


FIGURE 2.1: Hysteresis effect. (a) shows the different relationship between lung volume and transpulmonary pressure from exhalation to inhalation. Nehrke et al. (2001) showed the intra-cycle variability in cardiac respiratory motion by plotting the superior-inferior displacement of the heart against diaphragm displacement (b).

Intra-fraction variability has a different meaning than intra-cycle variability, and refers to the difference between breathing cycles within a fraction of time, usually referring to fractions of lung radiotherapy (McClelland et al., 2011, 2013).

### Inter-cycle Variability

*Inter-cycle variability* refers to differences in respiratory motion of the organ from one respiratory cycle to another. Several factors, such as auto regulatory mechanisms, posture and coordination between abdominal and chest breathing, determine the type of respiration performed in each breathing cycle. These factors can vary in their contributions from cycle to cycle causing variations in the motion.

Since the forces acting on the thorax and abdomen vary between the upright, prone, supine or lateral side postures (Vellody et al., 1978), image acquisition for IGIs

and the interventions themselves are typically carried out in the same body posture, normally supine (Scott et al., 2009).

Several studies (Konno and Mead, 1967; Sharp et al., 1975; Troyer and Estenne, 1984) have investigated the influence of abdominal and chest breathing on the resulting respiratory pattern, showing that in normal breathing there is coordination between the two mechanisms, with abdominal breathing being normally dominant over chest breathing. However, during deep and fast breathing, the contribution of the intercostal muscles increases and the coordination between diaphragm contraction and rib cage movement diminishes. This varying correlation makes the breathing motion unpredictable. Despite such investigations on the roles of abdominal and chest breathing, the formation of clear conclusions is hindered by the high inter-subject variability in respiratory motion, as reported in Tobin et al. (1983) and Benchetrit (2000).

Inter-cycle respiratory motion variability is typically observed during cardiac IGIs performed while the patient is awake, e.g. during cardiac ablation procedures.

### 2.1.2 Cardiac Respiratory Motion

Like the lungs, liver, bowels, kidneys and pancreas, the heart is subject to respiratory motion. Due to its anatomical position, the heart is affected by both the rib cage and diaphragm motion, making cardiac respiratory motion<sup>1</sup> unpredictable and challenging to compensate for.

A common technique for dealing with cardiac respiratory motion is breath-holding. Healthy individuals may comfortably suspend their breath for 10 to 40 seconds, allowing imaging data to be acquired with minimal effects from respiratory motion. However, breath-holding cannot be easily performed by patients with cardiovascular or pulmonary diseases, and often the time required for imaging or treatment is longer than a typical breath-hold duration. Furthermore, Holland et al. (1998) showed that the diaphragm is subject to drifts during breath-holding at end-inhale and end-exhale, meaning that motion cannot be completely eliminated.

Early investigations (Wang et al., 1995) showed a linear relationship between the supero-inferior (SI) translation of the heart and the right hemi-diaphragm displacement. Since the displacement of the diaphragm can sometimes be easily measured

---

<sup>1</sup>Hereafter, the wording *cardiac respiratory motion* refers to motion of the heart due to respiration only, and not to the contractile motion of the heart.

during image acquisition (e.g. using MRI pencil-beam navigators, Ehman and Felmlee (1989)), this opened up the possibility of calibrating this relationship and using it to estimate the cardiac respiratory motion. This can be seen as the earliest and simplest type of motion model (McClelland et al., 2013). More details will be given in Chapter 3. As shown in Figure 2.1(b), Nehrke et al. (2001) reported the hysteretic behaviour of the SI translation of the heart, highlighting how this intra-cycle variability is strongly subject dependent. Manke et al. (2002a) compared three different motion correction methods for Cardiac Magnetic Resonance Angiography (CMRA), showing a 3D affine motion correction to be more accurate than SI and 3D translational motion corrections. High inter-subject variability of the model parameters was also reported. In McLeish et al. (2002), the non-rigid motion of the heart at the right coronary artery, right atrium, and left ventricle (LV) was assessed during breath-holds at different respiratory positions. The rigid-body motion of the heart was found to be mostly in the SI direction, while significant non-rigid deformations were found for the free wall of the right atrium and the LV. Shechter et al. (2004) investigated cardiac respiratory motion during normal free-breathing as opposed to breath-holds, suggesting that free-breathing and breath-hold respiratory motion differ. This was later demonstrated in Blackall et al. (2006). The values of cardiac respiratory motion reported in McLeish et al. (2002) and Shechter et al. (2004) are summarised in Table 2.1.

<b>Parameters</b>	Mean $\pm$ Std. Dev.	
	McLeish et al. (2002)	Shechter et al. (2004)
SI translation (mm)	16.4 $\pm$ 4.2	4.9 $\pm$ 1.9
AP translation (mm)	7.1 $\pm$ 2.9	1.3 $\pm$ 1.8
LR translation (mm)	-3.8 $\pm$ 2.1	0.4 $\pm$ 2.0
SI rotation ( $^\circ$ )	-0.6 $\pm$ 3.3	-0.7 $\pm$ 1.5
AP rotation ( $^\circ$ )	3.8 $\pm$ 1.8	1.2 $\pm$ 1.3
LR rotation ( $^\circ$ )	-1.8 $\pm$ 1.7	-1.5 $\pm$ 0.9
Right atrium midpoint (mm)	16.0 $\pm$ 4.2	-
Right coronary midpoint (mm)	17.0 $\pm$ 4.0	-
LV apical point (mm)	22.5 $\pm$ 4.2	-
Right diaphragm (mm)	42.7 $\pm$ 11.2	-

TABLE 2.1: Motion deformation of the heart from end-exhale to end-inhale. In McLeish et al. (2002), the six rigid deformations and displacements at four cardiac locations were measured for 8 volunteers during breath-hold between maximum exhale and maximum inhale. In Shechter et al. (2004), the six rigid body deformations were measured in 10 patients during normal free-breathing angiography.

## 2.2 Image-Guided Interventions

In this Section, a brief overview of the aims and general framework of minimally invasive image-guided procedures is provided. In the last few decades, a significant move from open surgery to minimally invasive surgery has occurred in the performance of surgical procedures (Peters and Cleary, 2008; Perrin et al., 2009). The main advantage of minimally invasive surgery over open surgery is a much reduced damage of surrounding tissues which results in a lower patient mortality, faster recovery and shorter hospital stay. The advances in medical technology and imaging technology have played a key role in adopting minimally invasive interventions as standard clinical procedures (Peters and Cleary, 2008; Perrin et al., 2009; Linte et al., 2013), providing surgeons with accurate steerable instruments and real-time imaging modalities that reduce the need for direct access to the target structures.

Given the increasing complexity of minimally invasive procedures, more rich and accurate information is required to compensate for the lack of direct vision and thus carry out successful procedures. To this end, minimally invasive interventions that use pre-procedure data during the procedure to provide surgeons with such information have been increasingly adopted. In this thesis, the term IGIs refers to minimally invasive procedures that combine pre-procedure and intra-procedure data.

Although the exact workflow of image-guided systems depends on the application, some features and techniques are common, regardless of the specific use. According to Cleary and Peters (2010), a typical sequence for computer-assisted IGIs is given by:

1. acquisition of pre-procedure imaging data. Typically, these are 3D images acquired using Computed Tomography (CT), Rotational X-ray Angiography (RXA) and Magnetic Resonance Imaging (MRI). The aim of pre-procedure imaging is to provide high spatial resolution information about the target anatomy;
2. tracking of surgical tools and catheters relative to the patient anatomy. Typically this is achieved by using external tracking and/or image-based tracking;
3. registration of the pre-procedure imaging data to the patient anatomy, a.k.a. image-to-physical registration. Registration refers to the process of bringing two or more coordinate systems into spatial alignment (Hajnal et al., 2001). This normally means determining the spatial alignment of the pre-operative images, often acquired with different imaging modalities, with respect to the intra-procedure

position of the patient. In order to correctly perform the registration, anatomical features or fiducial markers common to the coordinate systems are identified. Point and/or surface matching can be used to align the corresponding features represented in the different coordinate systems. The accuracy of the alignment can be assessed using Target Registration Errors (TRE) (Fitzpatrick et al., 1998). Image-to-image registration can also be employed to align the 3D pre-procedure imaging data to the 2D or 3D intra-procedure imaging data (Markelj et al., 2012). Given the higher information content of 2D/3D images compared to single features or fiducial markers, image-to-image registration can play a significant role in image-to-physical alignment. To this end, new and efficient similarity measures for the registration of multi-modality images have been proposed (Penney et al., 2008; Wein et al., 2008; Heinrich et al., 2013), as well as image denoising and segmentation algorithms. Image-to-image registration also allows the alignment of atlases or biomechanical models of the target structures to intra-procedure imaging data (Hawkes et al., 2007; Edwards and Bello, 2010; Hu et al., 2012);

4. visualisation of the intra-procedure instruments with respect to the pre-procedure imaging data. Surgeons can use this visualisation to carry out the intervention. The accuracy requirements vary according to the procedure (Linte et al., 2010, 2012), however poor instrument tracking or image-to-physical registration inaccuracies and errors can lead to inaccurate guidance information and failure of the procedure;
5. image confirmation upon procedure completion. Depending on the type of procedure performed, a high spatial resolution image is usually acquired to assess the success of the procedure.

The aforementioned IGI framework can change slightly according to the application. However, although the specific image modalities and surgical instruments will vary depending on the procedure, the sequence of pre-procedure image acquisition, instrument tracking, intra-procedure imaging and image-to-physical registration is performed in most IGIs.

### 2.2.1 Imaging Technology

As mentioned in Section 2.2, the purpose of pre-procedure imaging is to gain the information the surgeon needs to diagnose, accurately plan and carry out the intervention. Usually this means anatomical information about the structure to treat, as well as functional information that can characterise infarcted tissues, lesions or tumours. High spatial resolution is normally a requirement for pre-procedure imaging. On the other hand, intra-procedure imaging should have high temporal resolution to provide real-time information about the position of surgical instruments and the target anatomy. In selecting a suitable imaging modality to use for pre-procedure and intra-procedure imaging, the following characteristics are normally considered:

- spatial resolution; i.e. the ability to detect the smallest possible feature of interest;
- temporal resolution;
- image contrast; i.e. the ability to differentiate tissue boundaries;
- ability to characterise different tissues;
- degree of tissue penetration;
- use of ionising or non-ionising radiations;
- cost associated with the image acquisition.

The main characteristics of the imaging modalities commonly used for pre- and intra-procedure imaging are summarised in Table 2.2. Below, these modalities are briefly described in general terms rather than technical. See Dowsett et al. (2006) for a complete description of the physics underlying each imaging modality.

Echography (echo) uses ultrasound (US) acoustic waves to map the interfaces between tissues. In particular, waves that are reflected by tissue boundaries (echo waves) are measured and displayed as an image. The higher the difference in acoustic impedance between neighbouring media, the stronger the reflected echo wave. In Brightness-mode (B-mode), the brightness of the pixel/voxel is directly proportional to the intensity of the measured echo wave. US waves are affected by mechanical absorption and diffraction and scattering effects, that cause loss of energy and characteristic image artefacts, such as the *speckle* effect (Thijssen, 2003), tissue inhomogeneities, multiple and off-axis reflections and shadowing (Kremkau and Taylor, 1986; Noble and

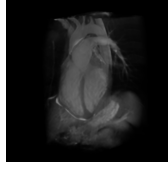

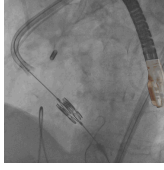
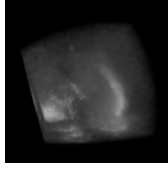
Modality	MRI	CT	Fluoroscopy	Echo
				
Dimensionality	2D/3D	2D/3D	2D	2D/3D
Ionising energy	No	Yes	Yes	No
Advantages	Soft-tissue contrast, spatial resolution	Spatial resolution, image contrast	Temporal resolution, instrument visualisation	Temporal and spatial resolution, cost
Disadvantages	Cost, temporal resolution	Radiation dose, contrast agent	Radiation dose, soft-tissue contrast	Limited FoV, image artefacts
Use in IGIs	Pre-, (Intra-) procedure	Pre-, (Intra-) procedure	Intra-procedure	Intra-procedure

TABLE 2.2: Summary of the characteristics of the imaging modalities commonly employed in IGIs.

Boukerroui, 2006). For cardiac applications, 2 – 4 MHz US waves with spatial resolution of 0.6 – 2 mm are used. Tissue penetration is usually 12 – 15 cm, generating a limited field of view (FoV). The temporal resolution of 2D/3D echo imaging is lower than a hundred *ms*. Despite the characteristic imaging artefacts, the use of mechanical waves makes echo a safe and low-cost imaging technique that provides 2D and 3D real-time intra-procedure images in IGIs (Noble et al., 2011).

X-rays are ionising electromagnetic radiation that penetrates bone and soft tissues and can either be absorbed, scattered or remain unchanged depending on the density of the tissues. The variation in absorption of different tissues is what is detected and depicted in the resulting image. X-ray imaging can be used for single static images or for real-time sequences, a.k.a. fluoroscopy imaging. Fluoroscopy is currently the preferred imaging modality in cardiac interventions, since it allows visualisation, tracking and guidance in real-time of surgical tools and catheters. However, because of its projective nature, X-ray imaging generates 2D images only. Furthermore, due to a low soft-tissue contrast, contrast agents need to be used to visualise vessels. Spatial resolution is normally  $< 1mm$ , depending upon the energy of the X-rays.

CT imaging provides volumetric information by combining multiple X-ray projections. The physical principles concerning energy sources, ionising issues and tissue



penetration are the same as for X-ray imaging. Most of the common CT machines have rotating gantries that quickly rotate around the subject and use algorithms such as filtered back projection or iterative reconstruction to accurately reconstruct the corresponding transverse slices. CT images have high spatial resolution ( $\sim 0.8\text{mm}^2$  in-plane) and boundary contrast, particularly in bony areas. Soft-tissue contrast can be improved further by using intravenous contrast agents. CT is mainly employed as a pre-procedure imaging technique, although intra-procedure uses have been investigated (Masamune et al., 2001). The main drawback of this modality for interventional use is the high radiation dose delivered to the patient and clinical staff.

RXA (a.k.a. flat panel C-arm CT or cone-beam CT) is an emerging modality that allows pre- and intra-procedure 3D imaging for minimally-invasive surgery and interventional cardiology (Orth et al., 2009). By rotating the X-ray source and detector (typical rotation  $\sim 190^\circ$ ) and acquiring a few hundred 2D X-ray images over a time period of 5 to 20 seconds, a C-arm cone-beam CT system reconstructs a complete volumetric image. This image modality provides 3D images with lower contrast resolution than CT imaging.

MRI uses a high static magnetic field and radio frequency (RF) energy to image the content of hydrogen in tissue. Both magnetic and RF energies are non-ionising. MRI provides high soft-tissue contrast that can be improved further by using contrast agents. However, for adequate signal-to-noise ratios (SNR), multiple applications of the RF energy are necessary, increasing the acquisition time and the likelihood of image artefacts due to motion occurring between subsequent RF applications. Respiratory and cardiac gating techniques need to be employed to acquire high spatial resolution images of the heart, leading to image acquisition times of several minutes. For these reasons, MRI is typically used as a pre-procedure imaging modality, although its use as an intra-procedure modality has successfully been reported (Razavi et al., 2003). Compared to other imaging modalities, MRI has the highest image acquisition costs.

### 2.2.2 Cardiac Image-Guided Interventions

The main application for the methods developed in this thesis is minimally-invasive cardiac IGIs, therefore an overview of the aims and of the state-of-the-art is provided in this Section.

Clinical applications of IGIs on the heart have been investigated by a large number of groups, leading in some cases to the acceptance of the procedure as a clinical standard (Peters, 2006; Perrin et al., 2009; Cleary and Peters, 2010). This is the case for electrophysiology (EP) studies. The aim of EP studies is to reconstruct a map of the electrical conduction system of the heart by inserting catheters into the cardiac chambers, allowing the location and treatment of abnormal conduction regions that might cause cardiac arrhythmias. Cardiac arrhythmias are typically treated using ablation therapy or pacemaker implantation.

Cardiac image-guided interventions normally involve the use of fluoroscopic images to guide the insertion and movement of catheters, while MRI, CT and RXA can be used to image patients prior to the intervention. Pre-procedure imaging can be used to derive cardiac geometry, the distribution of myocardial scarring, the myocardial motion and blood flow (Rhode and Sermesant, 2011; Rhode et al., 2012). An example of a pre-procedure image and corresponding cardiac segmentation is shown in Figure 2.2.

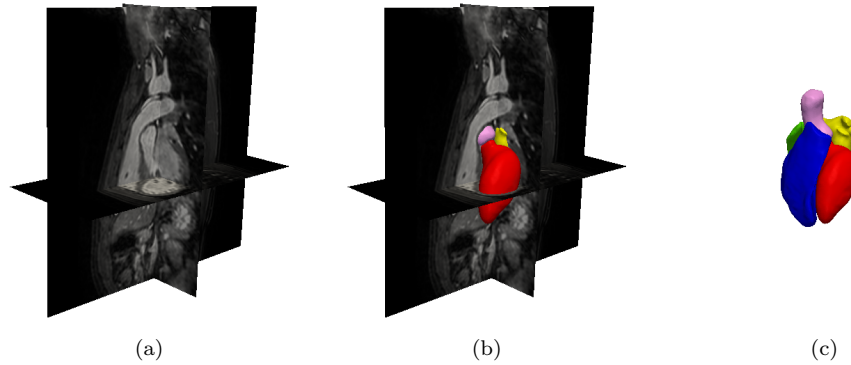


FIGURE 2.2: Example of a 3D MRI pre-procedure image and cardiac segmentation obtained by using a Philips segmentation toolkit. Three orthogonal views of the high resolution 3D MRI are shown in Figure 2.2(a). Image processing is used to derive an anatomical segmentation of the main cardiac chambers (Figures 2.2(b)-2.2(c)). The segmentation corresponding to the target structure can be overlaid onto intra-procedure images for guidance purposes.

Depending upon the cardiac procedure, the patient conditions and the clinical centre guidelines, sedation or anaesthesia is used. Sedation is typically chosen for long and low-risk procedures, such as some EP procedures, or for procedures requiring patient feedback, i.e. cardiac ablation therapy. The patient is free-breathing during sedation, while anaesthetised patients are mechanically ventilated.

MRI has been used as a pre-procedure imaging modality, which is subsequently registered to the intra-procedure fluoroscopy images or EP data (De Buck et al., 2005).

Such techniques can be performed in an XMR suite (Rhode et al., 2003, 2005; Yu et al., 2005), where an X-ray system is coaxially aligned with an MRI system in the operating room, allowing rigid-body registration of the MRI and fluoroscopy images during the same acquisition session. The X-ray system can also be embedded within the MRI scanner, which allows the simultaneous acquisition of fluoroscopy and MRI data (the closed-bore XMR system (Brzozowski et al., 2006)). The use of MRI alone as a real-time intra-procedure imaging modality has also been investigated by several groups (Razavi et al., 2003; Guttman et al., 2007).

3D pre-procedure cardiac roadmaps can be derived from CT. In Sra et al. (2007) and Knecht et al. (2008), atrial fibrillation (AF) treatment was performed by overlaying 3D CT images of the left atrium onto the real-time intra-procedure fluoroscopy images, while Ector et al. (2008) used a CT-based 3D model of the heart in combination with biplane fluoroscopy to guide instrument navigation.

Some of the techniques for overlaying 3D MRI or CT imaging data onto intra-procedure fluoroscopy are commercially available. However, the ionising energy delivered by RXA and CT and the high costs associated with MRI hamper the use of such techniques as intra-procedure imaging modalities in clinical routine for the majority of cardiac procedures. To overcome some of these limitations, echo has been proposed as an additional and/or alternative imaging modality for intra-procedure guidance. Yuen et al. (2008) used echo imaging alone to perform intra-cardiac procedures. They proposed a 3D echo-guided system that synchronises the instrument motion with the cardiac beating motion. Other works proposed the use of echo imaging as an extra intra-procedure modality, adding soft-tissue information to the fluoroscopy imaging. Wein et al. (2009) proposed the fusion of intra-cardiac echo imaging with CT images, while in Ma et al. (2009), King et al. (2009b) and King et al. (2010b) pre-procedure MRI volumes were registered to intra-procedure echo images. In Gao et al. (2010), a rapid algorithm for the registration of transoesophageal echo (TOE) and fluoroscopy images was proposed, while Housden et al. (2013) proposed a framework for the registration of pre-procedure cardiac segmentations and intra-procedure fluoroscopy and TOE. An example of this registration framework is shown in Figure 2.3. In Ma et al. (2010), a hybrid echo and X-ray guidance system that used a robotic arm to automatically acquire the echo imaging data was proposed. Furthermore, in Linte et al. (2008),

real-time intra-procedure echo imaging was fused with pre-procedure images, electrophysiological data and magnetically tracked surgical instruments for cardiopulmonary bypass surgery.

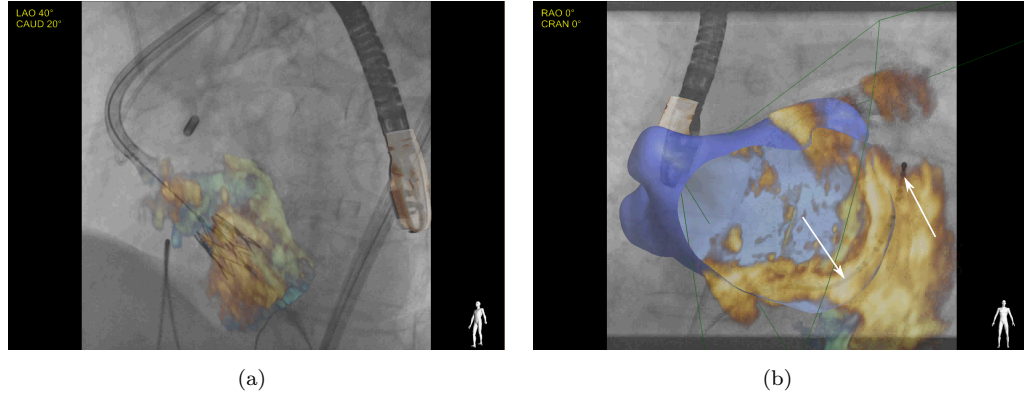


FIGURE 2.3: Example of multi-modality registration in a cardiac IGI. In Figure 2.3(a), intra-procedure TOE images are automatically overlaid onto X-ray fluoroscopy images. Despite the limited FoV, TOE provides the 3D soft-tissue information lacking in X-ray images. As shown in Figure 2.3(b), a much richer source of information is provided by overlaying pre-procedure information onto the intra-procedure modalities. In this case, a segmentation of the left atrium (see Figure 2.2), is overlaid onto TOE and X-ray images. The white arrows show misalignments due to motion.

During many cardiac procedures, electro-anatomical mapping systems are routinely used to collect cardiac electrical data, deliver ablation therapy and pace the heart (Rhode et al., 2012). Such electro-anatomical data can be obtained using commercially available systems such as CARTO (Biosense Webster), EnSite NavX (St. Jude Medical), or LocaLisa (Medtronic). Cardiac roadmaps derived from pre-procedure CT/MRI/RXA can be fused to the electro-anatomical maps using integrated approaches such as CARTO-Merge or Ensite-Fusion, reducing procedure time, radiation dose and improving patient outcome in ablation therapies (Earley et al., 2006). Examples of commercially available systems to overlay pre-procedural images onto X-ray fluoroscopy are EP Navigator (Philips Healthcare) and syngo iPilot (Siemens Healthcare).

## 2.3 Discussion

The potential of IGIs for minimally-invasive cardiac procedures is very high and is quickly growing as a consequence of the recent advances in imaging and tracking system technology. Clinical accuracy requirements depend on the complexity of the procedure.

In Linte et al. (2010, 2012), some examples are provided for EP procedures, coronary artery bypass grafting, aortic valve implantation and atrial septal defect repair, where an indicative overall accuracy of  $5mm$  is considered sufficient for successful guidance. However, other cardiac applications, such as stem cell implantation therapy, or the assessment of ablation points can have higher accuracy requirements.

Any motion that occurs between the underlying anatomy and the static pre-procedure images used for guidance causes misalignments that can compromise the accuracy and success of the procedure. For instance, as shown in Figure 2.3(b), residual misalignments can be noticed between the static segmentation of the left atrium and the positions of the catheters. These misalignments are caused by the contractile and respiratory motion of the heart. Since the cardiac contractile motion is typically periodic and more repeatable than cardiac respiratory motion, it can normally be compensated for using a gating-based approach, i.e. by acquiring the images at the same contraction phase, for instance by synchronising image acquisition to the electrocardiogram (ECG) signal. Compensation for cardiac respiratory motion is more challenging. A similar gating-based approach would not be feasible due to the longer length of a breathing cycle. Therefore, the motion must be corrected, which involves the estimation of an aperiodic and significantly variable motion, as detailed in Section 2.1.1. Furthermore, given the magnitude of cardiac respiratory motion (see Table 2.1), estimation and compensation of such deformations is paramount to meet accuracy requirements in free-breathing sedated patients.

Respiratory motion modelling represents a promising and viable solution for robust respiratory motion estimation and compensation, and is the focus of this thesis. The following Chapter provides a description of the aims and methodologies of respiratory motion modelling, along with an overview of the state-of-the-art on this topic.

## Chapter 3

# Respiratory Motion Modelling

### Contents

---

<b>3.1</b>	<b>Building and Applying Respiratory Motion Models . . . . .</b>	<b>33</b>
<b>3.2</b>	<b>Subject-Specific Respiratory Motion Modelling . . . . .</b>	<b>36</b>
3.2.1	Modelling of Respiratory Motion Variability . . . . .	39
3.2.2	Echo Image-Driven Modelling . . . . .	44
<b>3.3</b>	<b>Population-Based Respiratory Motion Modelling . . . . .</b>	<b>44</b>
<b>3.4</b>	<b>Discussion . . . . .</b>	<b>45</b>

---

As mentioned in Section 2.1.2, several solutions have been proposed to deal with respiratory motion. The most common alternative techniques to motion models are breath-holding, respiratory gating and motion tracking (McClelland et al., 2013). Breath-holding represents the simplest solution, but the time required for imaging or treatment is normally longer than a typical breath-hold duration ( $< 30s$ ). Respiratory gating consists of the acquisition/use of images only during a limited window of time, typically end-exhale. This results in longer acquisition/treatment durations, and the long duration of respiratory cycles makes such approaches unsuitable for IGI applications. Motion tracking normally requires markers to be implanted into or nearby the region of interest, so that the markers can be subsequently tracked, for instance, by using fluoroscopy imaging. Implantation of the markers is an invasive procedure, and motion information is not available for whole organs but is limited to the markers only. To overcome the limitations of such techniques, respiratory motion modelling has been investigated.

Motion modelling has been proposed to estimate and compensate for respiratory motion in image acquisition and IGIs on organs in the chest and abdomen. The underlying idea is to build a model of the subject's respiratory motion that can be subsequently applied for motion estimation and correction. A thorough review on respiratory motion models can be found in McClelland et al. (2013). The scope of this Chapter is to provide an overview of respiratory motion modelling for image acquisition, IGIs and image-guided treatments, highlighting the limitations of many current approaches that this thesis seeks to address. In particular, this thesis seeks to overcome the lack of accuracy of current motion models used in IGIs by developing novel methods to deal with the intra- and inter-subject motion variability by using intra-procedure echo imaging. Therefore, respiratory motion models able to deal with intra-subject variability in motion are reviewed in Section 3.2.1, while the use of echo images to guide motion models is discussed in Section 3.2.2. Motion models aiming to model inter-subject variability are analysed in Section 3.3. Where possible, the same notation and terminology as in McClelland et al. (2013) is used.

### 3.1 Building and Applying Respiratory Motion Models

The aim of respiratory motion modelling is to parametrise the motion as a function of some measurable surrogate data. The model parameters are subsequently employed to estimate respiratory motion, given measurements of the same or similar surrogates.

The typical workflow associated with motion modelling consists of two phases: model building and model application. An example of a respiratory motion modelling workflow is shown in Figure 3.1.

Hereafter,  $\Phi$  denotes the respiratory motion model,  $s$  the surrogate data and  $\mathbf{M}$  the motion estimate of the model. The motion model  $\Phi$  can represent 1D or 3D translations, rigid-body, affine or non-rigid deformations. The choice of the motion description used by  $\Phi$  affects the estimation accuracy achievable and the overall computational complexity. This choice is normally based on knowledge of the expected motion of the organ(s) being targeted.

When building the model, the motion of the structures of interest is normally estimated from a dynamic calibration scan using image registration. The dynamic

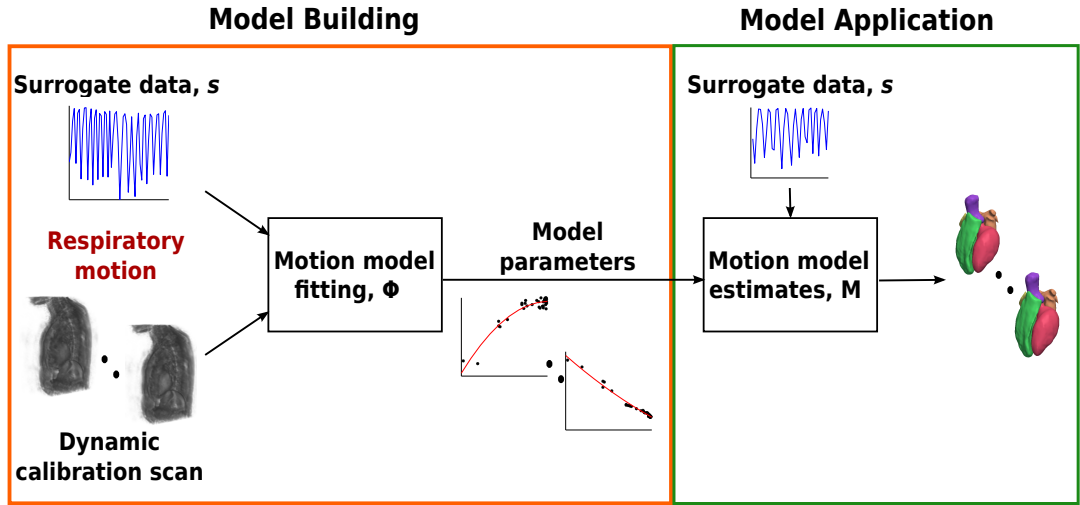


FIGURE 3.1: Example of direct correspondence respiratory motion model.

calibration scan and the surrogate data are simultaneously acquired prior to the procedure. According to the chosen motion description, model parameters are fitted to the motion estimates as a function of  $s$ . Several methods to derive the model parameters, such as fitting techniques or statistical methods, can be used. Some instances of respiratory surrogates are the respiratory bellows (Santelli et al., 2011), spirometry (Lu et al., 2005), MRI navigator echoes (Manke et al., 2002a), and optical tracking of chest movement (Hughes et al., 2009). Ideally, surrogate data should be easily acquirable with high temporal resolution during the building and application of the model. However, this is not always the case, especially in IGIs, where the use of MRI or spirometry during the procedure is often not possible. In such cases, surrogate data different from the surrogates used to build the model can be used during model application, e.g. intra-procedure images. Depending on whether the surrogate acquired during model building and application are the same or different, two distinct approaches to model application are possible, as described below.

In *direct correspondence models* (see Figure 3.1), the surrogate data used for model building and application are of the same form and the model estimates are computed directly as a function of  $s$

$$\mathbf{M} = \Phi(s). \quad (3.1)$$

In *indirect correspondence models*, the surrogates used for model building are typically different from the surrogate data in the application phase. In some cases, no surrogate data are acquired during model building, and instead, internal variables are



derived from the motion estimates (King et al., 2012). Often, surrogate data in the application phase are intra-procedure images and, for this reason, indirect correspondence models have also been referred to as *image-driven models*. As shown in Figure 3.2, the internal variables of the indirect correspondence model (e.g. position in the respiratory cycle (Blackall et al., 2005) or parameters representing reduced dimensions in a statistical model (King et al., 2012)) are optimised to find the best match between the intra-procedure surrogate  $I$  (e.g. intra-procedure image) and the estimates of  $I$  made by the motion model

$$\mathbf{M} = \Phi(\tilde{\mathbf{x}}), \quad \tilde{\mathbf{x}} = \arg \max_{\mathbf{x}} \text{Sim}(T(I_{ref}, \Phi(\mathbf{x})), I), \quad (3.2)$$

where  $\mathbf{x}$  are the internal variables,  $\Phi(\mathbf{x})$  are the motion parameters estimated by the model,  $I_{ref}$  is a reference image,  $T$  is a function that transforms  $I_{ref}$  given  $\Phi(\mathbf{x})$  and  $\text{Sim}$  is a similarity measure (McClelland et al., 2013).  $I_{ref}$  and  $I$  can be acquired using different modalities, so  $\text{Sim}$  might involve feature enhancement or image simulation (King et al., 2001; Blackall et al., 2005; King et al., 2010b) to compute an inter-modality similarity measure. In model application, given the model  $\Phi$  and the optimised internal variables,  $\tilde{\mathbf{x}}$ , the model outputs an estimate of the respiratory motion,  $\mathbf{M}$ . In IGIs,  $\mathbf{M}$  can be used to update the position of a pre-procedure anatomical roadmap in near real-time (i.e. with the temporal resolution of the surrogate data and the registration time) to provide continuous and accurate guidance information.

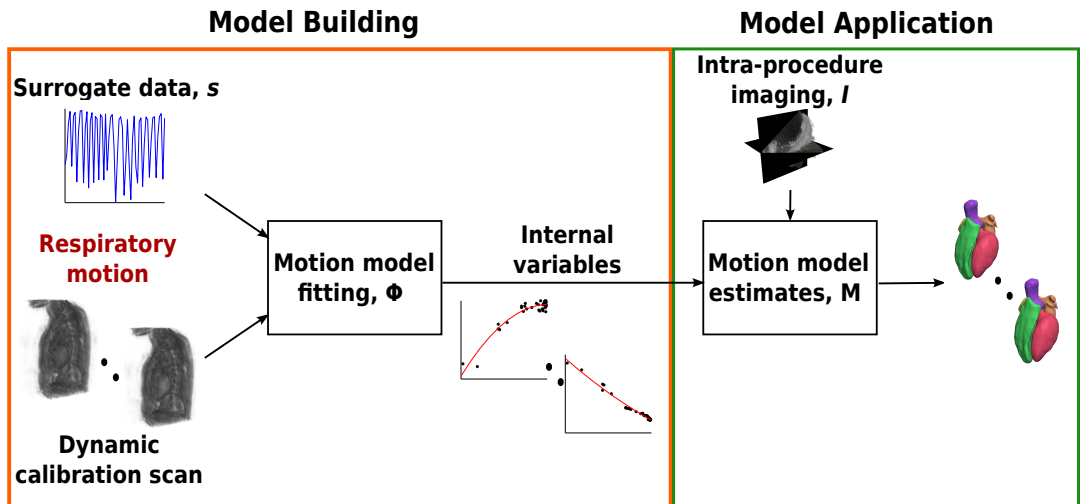


FIGURE 3.2: Example of indirect correspondence respiratory motion model.

Respiratory motion models can be *subject-specific* or *population-based*. When building subject-specific models, the respiratory motion is estimated from a dynamic calibration scan of the same subject that the model will be applied to, while in population-based models, the motion in the calibration phase is estimated from calibration scans acquired previously from a population sample of subjects, and the model is subsequently applied to a subject not belonging to the population sample. Details of these two types of motion models are outlined in Sections 3.2 and 3.3, respectively.

## 3.2 Subject-Specific Respiratory Motion Modelling

This Section reviews the state-of-the-art in subject-specific respiratory motion modelling. The ability of motion models proposed in the literature to deal with intra- and inter-cycle variability is discussed in Section 3.2.1, while echo-driven motion models are discussed in Section 3.2.2. Key papers are summarised in Table 3.1, detailing the number and nature of surrogate data, the imaging modality used to build the model and the type of model employed. The last column of Table 3.1 reports whether the correspondence model is direct,  $D$ , (i.e. the same or related surrogates are employed to build and apply the motion model) or indirect,  $I$ , (i.e. imaging data is used to apply the motion model).

In subject-specific motion models, the dynamic calibration scan is acquired from the same subject that the model is subsequently applied to. For this reason, subject-specific models are generally more accurate than population-based models. As can be noticed from Table 3.1, the dynamic calibration scan is typically acquired using 4D MRI or CT, meaning that dynamic 3D images over time are acquired ( $4D = 3D + t$ ). However, the dynamic calibration scan can cause significant interruptions to the clinical workflow, or often cannot be acquired at all, due to patient considerations, such as patients with MRI-incompatible implants or bariatric patients, or, as mentioned in Section 2.2.1, due to dose issues or high acquisition costs. Furthermore, in some cases, the quality of the dynamic calibration scan might not be sufficient for a reliable estimation of respiratory motion. These drawbacks of subject-specific models are further discussed in Section 3.4.

Paper	Intra-	Inter-	# Surr	Modality(ies)	Model(s)	Correspondence
Atkinson et al. (2001)	x	x	1	2D echo	SI translation	D
King et al. (2001)	x	x		MRI, 3D echo	Point Distribution Model	I
Manke et al. (2002a,b)	x	x	1	CMRA	SI, 3D translation, affine	D
Manke et al. (2003)	✓	✓	3	CMRA	Affine	D
Shechter et al. (2004, 2005)	✓	x	1	X-ray	Translational, rigid-body, affine	D
Ablitt et al. (2004) <sup>2</sup>	x	x	n	CMRA	PLSR	D
Low et al. (2005) <sup>3</sup>	✓	x	2	CT	Independent linear functions	D
McClelland et al. (2005, 2006)	✓	x	1	CT	Polynomial, B-spline, Fourier interp of FFD	D
Blackall et al. (2005)	x	x	1	MRI, 2D echo	Non-rigid, 3 <sup>rd</sup> order polynomial	I
Blackall et al. (2006)	x	x	1	MRI	Affine	D
Zhang et al. (2007) <sup>3</sup>	✓	x	2	CT	FFD and PCA	D
King et al. (2008, 2009a)	✓	x	1	MRI, X-ray	Affine	D
Yang et al. (2008) <sup>3</sup>	✓	x	2	CT	Linear forward and inverse	D
King et al. (2009c)	✓	✓	1	MRI, X-ray	Affine (3 models, exh. & inh.)	D
Klinder et al. (2010) <sup>3</sup>	✓	x	PCs	CT	Statistical inference	D
King et al. (2010a)	x	x	1	MRI, 3D echo	Affine and rigid-body	I
Schneider et al. (2010)	✓	✓	6	X-ray	Rigid-body PCA-based	I <sup>4</sup>

<sup>2</sup>Given the multiple navigators used, this model could, in principle, deal with intra- and inter-cycle variability. However, the model was built from data representing a single breathing cycle only, without differentiating between exhale and inhale.

<sup>3</sup>In principle, these motion models could estimate intra- and inter-cycle variability. However, 4D CT images retrospectively reconstructed from segments acquired during multiple breathing cycles were employed, thus representing a single respiratory cycle only.

<sup>4</sup>PCs were optimised to match the model estimate with the fluoroscopy images of guidewires.

Paper	Intra-	Inter-	# Surr	Modality(ies)	Model(s)	Correspondence
Savill et al. (2011)	✓	✓	1-2	MRI	Affine	D
McGlashan and King (2011)	✓	✓	1-2	MRI	Affine	D
McClelland et al. (2011) <sup>3</sup>	✓	x	1-3	CT	Cyclic B-spline for respiratory phase,	D
					3 <sup>rd</sup> order polynomial for surrogate value	
					2D linear function for value and its gradient	
King et al. (2012)	✓	✓	5	MRI, PET-MRI	PCA-based	I <sup>5</sup>

TABLE 3.1: Key papers on subject-specific respiratory motion modelling. For a thorough review see McClelland et al. (2013). A ✓ denotes the ability of the motion model to deal with the intra- or inter-cycle variability, whereas a x denotes the contrary. The fourth column shows the number of surrogates employed in building the motion model, while the fifth column describes the imaging modalities used to build and, if appropriate, apply the model. In the **Model(s)** column, a short description of the model type is provided. The last column reports the type of correspondence model, where *D* stands for direct and *I* stands for indirect.

<sup>5</sup>PCs were optimised to match the model estimate with a 2D MRI navigator image.

### 3.2.1 Modelling of Respiratory Motion Variability

The ability to model different types of respiratory motion variability is mainly determined by the dimensionality of the surrogate data/internal variables, the complexity of the motion model  $\Phi$  and the type of respiratory motion sampled by the dynamic calibration scan. For instance, using scalar surrogate data and a model that does not distinguish between exhalation and inhalation does not allow the modelling of either intra- or inter-cycle variability. Similarly, motion models built using dynamic images acquired during a single respiratory phase (e.g. exhalation or inhalation only), or representing a single respiratory cycle only (e.g. 4D helical or cine CT imaging) cannot capture intra- or inter-cycle variability, regardless of the complexity of the surrogates/variables or model  $\Phi$ . A brief description of the most relevant papers on modelling the different types of respiratory motion variability is given in the following Sections.

#### No Variability

Given the use of a scalar surrogate or dynamic images describing an average respiratory cycle, the following respiratory motion models could model an average respiratory cycle only, with no modelling of either intra- or inter-cycle variability.

As mentioned in Section 2.1.2, the earliest type of motion model was introduced by Wang et al. (1995), where a linear relationship between the SI translation of the heart and the SI displacement of the right hemi-diaphragm was reported.

In Atkinson et al. (2001), 2D echo images were retrospectively corrected for respiratory motion to reconstruct 3D images. The displacement of a passive marker at the subject's umbilicus was used as surrogate and a 1D translational motion description for cardiac respiratory motion was employed.

Manke et al. (2002a) assessed the ability of different motion models to describe the respiratory motion of the main coronary arteries using 3D Coronary Magnetic Resonance Angiography (CMRA). A MRI pencil-beam navigator echo acquiring the SI position of the right hemi-diaphragm was employed as a surrogate signal. The imaging was carried out during repeated breath-holds, therefore no intra-cycle variability was captured. The models compared were SI translation, 3D translation and a full affine model. Results showed the affine motion model to be the most accurate correction model. In Manke et al. (2002b), a subject-specific respiratory motion model

derived from a short free-breathing scan was subsequently used for prospective motion correction of a high resolution CMRA image.

In Blackall et al. (2006), fast MRI techniques to investigate the impact of intra- and inter-cycle reproducibility of respiratory motion in radiotherapy (RT) treatment for lung cancer were proposed. To investigate such variability, average motion models using images acquired during breath-holds and free-breathing sequences at exhalation, inhalation and during different respiratory cycles were built and compared. The surrogate was a MRI pencil-beam navigator echo placed on the right hemi-diaphragm.

A predictive respiratory motion model which used partial least squares regression (PLSR) to extract intrinsic relationships between cardiac respiratory motion and multiple scalar surrogate signals was proposed by Ablitt et al. (2004). To estimate cardiac respiratory motion, 3D ECG-gated MRI images were registered together using a FFD registration algorithm. PLSR was used to analyse the correlation between respiratory deformations and surrogates. Multiple 1D traces on the chest wall as depicted in the MRI images were used as input surrogates to the PLSR model. Given the multiple surrogate signals used, this model could, in principle, deal with intra- and inter-cycle variability. However, in the original paper, the model was built using respiratory gated images representing a single breathing cycle, without exhale and inhale differentiation.

### **Intra-cycle Variability**

The following motion models can model intra-cycle variability since the inhalation and exhalation phases were differentiated.

Shechter et al. (2004) investigated the respiratory motion of coronary arteries from free-breathing biplane X-ray angiography. Using a cardiac respiratory parametric model, the motion of the coronary arteries was separated into cardiac and respiratory components. The respiratory surrogate signal was obtained by tracking the displacement of the diaphragm, and three different respiratory motion models (3D translation, 3D rigid body, and 3D affine transformation) were investigated. The respiratory models covered a whole breathing cycle, and respiratory motion was parametrised as a function of the respiratory phase, where positive phase corresponded to exhalation, while negative phase indicated inhalation. In Shechter et al. (2005), the same cardiac respiratory parametric model was used to retrospectively and prospectively correct images acquired at arbitrary cardiac and respiratory phases.

A motion model for lung tumour localisation in RT planning was proposed in McClelland et al. (2005, 2006). Free-breathing 4D cine CT images were non-rigidly registered to a reference breath-hold volume. The AP displacement of the chest wall was used as respiratory surrogate. Three fitting functions (polynomial, spline and Fourier) were investigated, and the  $3^{rd}$  order spline was shown to be the most effective. By using the derivative of the surrogate signal, exhale and inhale phases were differentiated and modelled separately.

King et al. (2008) presented a respiratory motion model for X-ray guided cardiac EP procedures. An affine model was built based on a free-breathing pre-procedure ECG-gated 4D MRI scan. An affine registration was used to register the free-breathing volumes to an end-exhale reference volume. A MRI pencil-beam navigator placed on the diaphragm was used as respiratory surrogate. By comparing the navigator values with their predecessor/successor, exhalation and inhalation phases were determined and modelled separately.  $2^{nd}$  order polynomial functions were fitted to the affine motion parameters as a function of the surrogate. During the procedure, the motion of the diaphragm as tracked by fluoroscopy images was input to the motion model, providing respiratory motion correction of a roadmap used for guidance. Further validation of the motion model and an error simulation were presented in King et al. (2009a).

To estimate lung tumour respiratory motion for RT planning, Low et al. (2005) modelled respiratory motion as a function of the tidal volume and airflow, defined as the temporal derivative of the tidal volume. The model was tested on 4D cine CT images of the lungs, acquired simultaneously with the tidal volume as measured by a digital spirometer. Similarly, in Yang et al. (2008), a series of CT volumes were acquired in cine-mode and, by using an optical flow registration algorithm, they were registered to an end-exhale CT reference volume. Forward and inverse motion models were fitted to the estimated motion fields. Both models employed the tidal volume and airflow rate to parametrise the motion fields. Zhang et al. (2007) developed a respiratory motion model for the lungs for RT treatment. 3D CT images were acquired at ten positions of the respiratory cycle. A free-form deformation (FFD) registration algorithm was used to estimate the deformation field that mapped each 3D image to an end-exhale reference volume. The SI translation of the dome of the diaphragm and its temporal precursor were used as respiratory surrogate signals. Inhalation and exhalation phases

could therefore be differentiated. Principal Component Analysis (PCA) was performed to model the deformation field as a function of the surrogate data.

Inter-fraction variations in respiratory motion between the planning stage and successive RT fractions were assessed in McClelland et al. (2011). Lung respiratory motion was estimated from non-rigid registrations of 4D cine CT images. The respiratory surrogate signal was derived from the 3D skin surface displacement acquired by a stereo camera system. Three respiratory parameters were derived from the surrogate signal (amplitude, temporal gradient and respiratory phase) and used, in combination with the original surrogate, to build and compare three different motion models.

In Klinder et al. (2010), a direct correspondence PCA model was built to describe the subject-specific respiratory deformations of the lungs as estimated from 4D CT images. In the model application, a sub-set of deformations was supposed to be known and used to derive a model estimate.

The models proposed by Low et al. (2005), Zhang et al. (2007), Yang et al. (2008), McClelland et al. (2011) and Klinder et al. (2010) could, in principle, estimate intra- and inter-cycle variability. However, as mentioned earlier, since 4D CT images represent a single respiratory cycle, only the intra-cycle variability can be modelled.

### **Intra- and Inter-Cycle Variability**

In this section, respiratory motion models able to deal with intra- and inter-cycle variability are presented.

Similar to Manke et al. (2002a), Manke et al. (2003) proposed an affine motion model of the heart to correct for respiratory motion in CMRA. Three pencil-beam navigator echoes placed on the right hemi-diaphragm, on the chest wall, and on the right cardiac border were used as surrogate signals. These multiple navigators addressed non-linear properties and hysteresis effects in the motion, allowing modelling of intra- and inter-cycle variability. The optimal combination and weighting of the navigators was statistically determined after a short free-breathing calibration scan.

To capture inter-cycle variability, an adaptive and predictive motion model was proposed by King et al. (2009c). Three separate respiratory motion sub-models to describe normal, deep and fast breathing motion were built. Each sub-model represented the affine respiratory motion of the heart during a specific breathing pattern



as a function of the diaphragm displacement, as in King et al. (2008, 2009a). A recursive Bayesian estimation approach was adopted to predict the amplitude of the intra-procedure surrogate signal. The estimated amplitude was used to weight the interpolation between the motion estimates produced by each separate sub-model, thus adapting to the varying breathing patterns.

The effects of the nature and position of the surrogate signals on the estimation accuracy of cardiac respiratory motion models were investigated by Savill et al. (2011). Several post-processed MRI navigator echoes were simulated and, by using different combinations of these surrogate signals, affine motion models as in King et al. (2009a) were built and the estimation accuracy compared. The same procedure was used to investigate the impact of multiple navigators by McGlashan and King (2011).

Two relevant papers that employed a statistical technique similar to Klinder et al. (2010), but used an indirect correspondence model are described below.

A PCA-based respiratory motion model for motion compensation during cardiac IGIs was presented and validated in Schneider et al. (2010). 2D ECG-gated biplane cine angiograms were rigidly registered to a 3D pre-procedure segmentation of the coronary arteries, deriving a rigid transformation for each respiratory phase acquired. By assuming that such transformations lay on a linear sub-manifold in the six dimensional space of rigid 3D transformations, PCA was applied to find the associated basis vectors. The subject-specific model was used as a prior within the intra-procedure registration process to constrain the search space. In the intra-procedure registration, the coronary model was warped to match the projections of guidewires as imaged by the fluoroscopy images. In this case, the first six Principal Components (PCs) were the internal variables to be optimised in order to match the model estimation with the tracked guidewires.

Similar to Schneider et al. (2010), King et al. (2012) proposed a statistical subject-specific motion model formed from 4D MRI data and applied using an indirect correspondence model based on a 2D MRI image navigator. The technique was proposed for MRI-based motion correction of real-time Positron Emission Tomography (PET) data for simultaneous PET-MRI acquisition. A hierarchical FFD registration algorithm was employed to register the 4D MRI images of the lungs acquired during different breathing patterns. A PCA-based motion model was used to parametrise the non-rigid deformation fields. By using the first five PCs as internal variables, the model

was able to estimate both intra- and inter-cycle variability.

### 3.2.2 Echo Image-Driven Modelling

In this Section, an overview of indirect correspondence respiratory motion models that employ echo images as surrogates in the application phase is provided.

An early indirect correspondence model driven by freehand 3D echo images was proposed in King et al. (2001). In this paper, a statistical shape model and echo images were employed to register a pre-procedure segmentation of the liver to the intra-procedure physical space. This paper represents the first time that an indirect correspondence motion model was ever described.

Blackall et al. (2005) presented a technique to align a pre-procedure plan to intra-procedure echo images to aid needle placement for thermal ablation of liver metastases. A subject-specific motion model was built using 3D MRI images of the liver acquired during multiple breath-holds and the SI position of the diaphragm as the calibration surrogate. Non-rigid registration was used to compute the deformation fields of each breathing position with respect to an end-exhale reference volume. 3<sup>rd</sup> order polynomial functions were fitted to the 3D deformation field as a function of the SI position of the diaphragm. A single 2D echo image at an unknown respiratory position was acquired and used as the surrogate for model application. The pre-procedure plan was warped to match the corresponding anatomy. The warping was constrained by the respiratory motion model, meaning that the internal variable (i.e. the SI position of the diaphragm) was optimised so that the transformed pre-procedure plan matched the intra-procedure 2D echo image. A similar technique using 3D cardiac echo imaging was proposed in King et al. (2010a).

## 3.3 Population-Based Respiratory Motion Modelling

To overcome the need for a subject-specific calibration scan, population-based models have been proposed. There have been relatively few papers on this topic, and Table 3.2 reports the key contributions to date. As shown in Figure 3.3, the motion in the calibration phase is estimated from calibration scans previously acquired from a sample of a population of subjects, and the model is subsequently applied to an out-of-sample subject. In order to apply population-based motion models, the motion estimates

need to be transformed from the model space to the out-of-sample subject space, and this is usually achieved by registering a static template population image to a corresponding static image of the out-of-sample subject, and transforming the motion model accordingly.

Given the surrogate data and the dynamic calibration scan for each dataset in the population, an average respiratory motion model is typically built using all the subjects in the population, and is subsequently applied to any out-of-sample subject (Fayad et al., 2009, 2010; He et al., 2010; Ehrhardt et al., 2011; Klinder and Lorenz, 2012; Preiswerk et al., 2012). For direct correspondence models (Fayad et al., 2009, 2010; He et al., 2010; Klinder and Lorenz, 2012; Preiswerk et al., 2012), the respiratory motion estimates are obtained by simply inputting the surrogate data of the out-of-sample subject into the average population-based model. In Ehrhardt et al. (2011), the motion estimates of the mean motion model were scaled according to the depth of respiration of the out-of-sample subject. In Samei et al. (2012), a different model application technique was proposed for making more accurate population-based motion estimates. This approach was based on similarities of the surrogate to different members of the population, and was applied to estimate respiratory drift of the liver during RT treatment. No population-based indirect correspondence models have been proposed to date.

Since respiratory motion varies significantly between subjects (Keall et al., 2006), population-based models are generally less accurate than subject-specific models, as inter-subject respiratory motion variability is averaged out (McClelland et al., 2013).

### 3.4 Discussion

In this Chapter, an overview of subject-specific and population-based respiratory motion modelling has been presented.

Regarding subject-specific motion models, as can be noted from Table 3.1, some progress over time can be observed. Compared to initial motion models that were not able to model variability in motion, the necessity to improve respiratory motion estimation accuracy has led to the investigation and proposal of more sophisticated models that are able to describe both intra- and inter-cycle variability. Because direct correspondence models depend directly on the surrogate data, any inaccuracy

in its acquisition and application causes inaccuracies in the model estimates. Furthermore, most surrogate data used in direct correspondence models are relatively low-dimensional and so are limited in their ability to describe the complex variability in respiratory motion. To overcome these limitations, indirect correspondence motion models have been proposed that use high-dimensional imaging data as the surrogate. The use of imaging data to drive the model, instead of low-dimensional data, provides richer information about the motion of the tissue, allowing the model to potentially make more accurate estimates.

As shown in Table 3.2, population-based motion modelling is an emerging field, with only few works recently proposed. Despite the great advantage of not requiring the dynamic calibration scan, the poorer estimation accuracy compared to subject-specific motion models has so far limited their use to research purposes only.

As highlighted in McClelland et al. (2013), most of the motion model works proposed to date remain as research proposals. The only respiratory motion model currently in use in the clinic is embedded in the Cyberknife system for RT treatment (Schweikard et al., 2000). One reason for this lack of clinical translation lies in the lack of accuracy or robustness of many current techniques. Furthermore, the impact on the clinical workflow hampers the uptake of subject-specific motion models in clinically used systems.

The aim of this thesis is to improve clinical translation of respiratory motion models by proposing novel methods to address these limitations. To improve motion model estimation accuracy, a novel subject-specific respiratory motion model is presented in Chapter 4. This model uses both a scalar surrogate signal and dynamic 3D echo to drive a probabilistic motion model in a Bayesian framework. In Chapter 5, a proof of concept for the use of the Bayesian motion model to automatically guide the echo acquisition in cardiac IGIs is proposed. The automatic image acquisition further improves accuracy and robustness of the respiratory motion estimation. In Chapter 6, a novel personalisation technique for population-based respiratory motion models is presented. This personalisation allows more accurate motion estimation by exploiting inter-subject similarity in respiratory motion. In Chapter 7, these two novel techniques are combined to obtain a Bayesian respiratory motion model which does not require the acquisition of the subject-specific dynamic calibration scan.

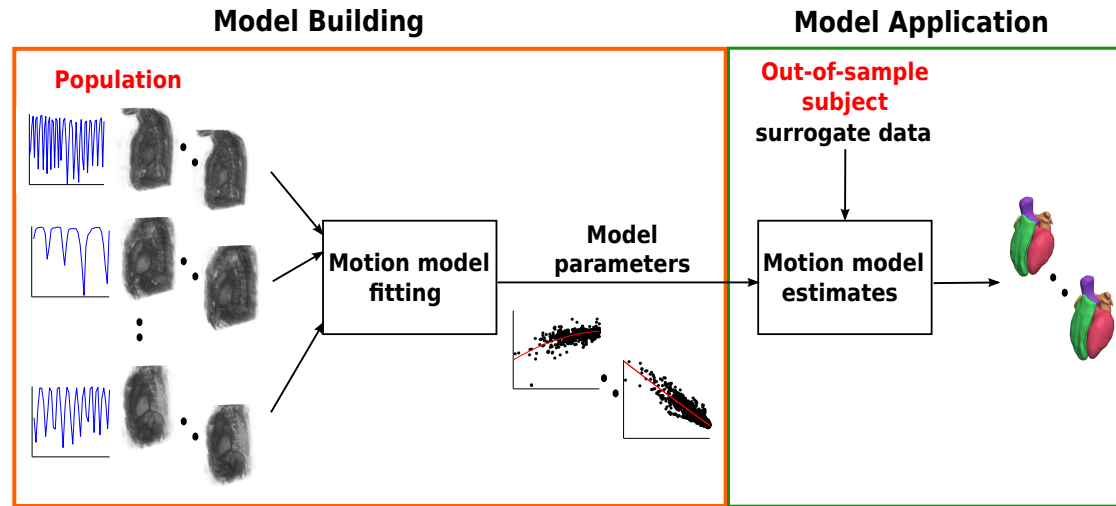


FIGURE 3.3: Example of population-based respiratory motion model framework.

Paper	# Subjects	Organ	Modality	Model(s)
Fayad et al. (2009, 2010)	3, 4	Lungs	4D CT	PCA
He et al. (2010)	30	Lungs	4D CT	Least-Squares Support Vector Machine
Ehrhardt et al. (2011)	17	Lungs	4D CT	Mean Motion Model
Klinder and Lorenz (2012)	31	Lungs	4D CT	PCA
Preiswerk et al. (2012)	20	Liver	4D MRI	PCA
Samei et al. (2012)	12	Liver	4D MRI	PCA

TABLE 3.2: Population-based respiratory motion models review. In this Table, the number of subjects in the population sample, the organ modelled, the modality used in the dynamic calibration scan and the technique employed to build the model are reported.

## Chapter 4

# Subject-Specific Bayesian Respiratory Motion Model

### Contents

---

<b>4.1</b>	<b>Introduction</b>	<b>49</b>
<b>4.2</b>	<b>Methods</b>	<b>50</b>
4.2.1	Overview	50
4.2.2	Bayesian Motion Estimation	51
4.2.3	Prior Probability	51
4.2.4	Likelihood	54
4.2.5	Optimisation of $\sigma_l^2$	55
<b>4.3</b>	<b>Experiments</b>	<b>56</b>
4.3.1	MRI Acquisition	56
4.3.2	Comparison of Estimation Techniques	57
4.3.3	Evaluation Using Real MRI, Simulated Echo Data	61
4.3.4	Evaluation Using Real MRI, Real Echo Data	63
4.3.5	Determination of the Optimal $\sigma_l^2$	65
<b>4.4</b>	<b>Results</b>	<b>67</b>
4.4.1	Simulated Echo Data	67
4.4.2	Real Echo Data	68
<b>4.5</b>	<b>Discussion</b>	<b>73</b>

---

## 4.1 Introduction

All motion models proposed to date have a significant limitation in that, for a given value of the surrogate data or internal variables, only a single predetermined motion estimate can be produced. In probabilistic terms, the model outputs the same motion estimate with a 100% confidence in estimation. In reality, the significant intra- and inter-cycle variability in respiratory motion means that such a restrictive model may introduce errors into the estimation process.

Over the last few years, the concept of uncertainty has been investigated and employed in several fields of medical image processing. For instance, confidence measures have played a significant role in optical flow measurements to identify unreliable flow vectors and recover corrupted optical flow regions (Kontermann et al., 2008). Taron et al. (2005) presented a method for obtaining an uncertainty measure from the registration process of different shapes. Similarly, Blanc et al. (2009) proposed a technique for estimating confidence regions around statistical shape models from partial observations. Recently, probabilistic frameworks to estimate spatial uncertainty in non-rigid registration have been proposed (Risholm et al., 2010b; Simpson et al., 2012; Risholm et al., 2013). These methods employed probabilistic methods to infer optimal regularisation parameters and derive a distribution of probable registrations. Furthermore, methods to visualise the uncertainty in non-rigid registration have been proposed (Risholm et al., 2010a; Hub et al., 2009).

In this Chapter, the concepts of direct and indirect correspondence motion models (see Section 3.1) are combined with the concept of uncertainty to overcome the limitations of previous motion models. The Chapter describes a novel technique to estimate cardiac respiratory motion based on a combination of a MRI-derived pre-procedure motion model and intra-procedure real-time echo images. The main novelty of the proposed approach lies in its probabilistic formulation, allowing motion estimates to be made with corresponding confidence measures. The MRI-derived model estimates the motion and its uncertainty which is then resolved using the echo imaging data. The use of a Bayesian approach allows the potentially conflicting information provided by the model and the echo data to be combined and resolved. This approach can be seen as a hybrid direct and indirect correspondence model since it employs a measurable

surrogate signal for the model formation but uses both the surrogate and imaging data to drive the model.

## 4.2 Methods

The work presented in this Chapter is described in Peressutti et al. (2013b), and extends the work presented in Peressutti et al. (2012). An overview of the proposed method for respiratory motion estimation is presented in the following Section.

### 4.2.1 Overview

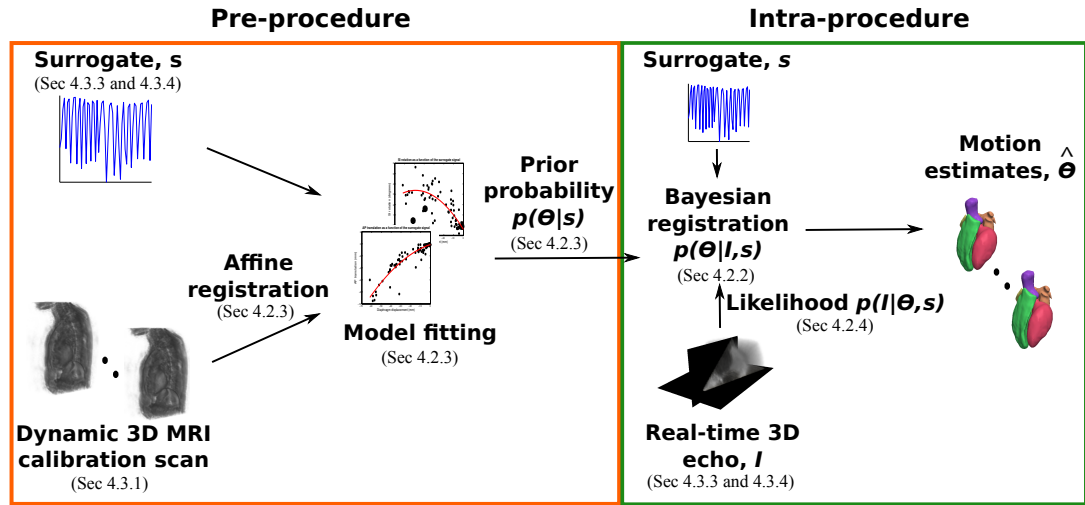


FIGURE 4.1: Schematic representation of the Bayesian motion estimation.

Figure 4.1 shows an overview of the proposed Bayesian motion estimation. Before the procedure, ECG-gated free-breathing dynamic 3D MRI images are acquired (see Section 4.3.1). A respiratory surrogate signal is acquired simultaneously with the dynamic calibration scan. Affine registration of the dynamic images is used to estimate the cardiac respiratory motion. Each of the affine parameters is modelled as a function of the surrogate signal and an associated uncertainty function is estimated. This serves as the prior probability function (see Section 4.2.3). During the procedure, the surrogate data together with live 3D echo imaging data are used to form the likelihood term (see Section 4.2.4). A measure of the echo image quality is used to determine the optimal combination of prior and likelihood (see Section 4.2.5). The final motion estimate is obtained in a *Maximum a Posteriori* (MAP) manner (see Section 4.2.2).



### 4.2.2 Bayesian Motion Estimation

The Bayesian framework combines prior knowledge of the subject-specific respiratory motion, in the form of a MRI-derived probabilistic motion model, with real-time echo images.

The posterior probability represents the state of certainty about a given phenomenon. The phenomenon here is the affine transformation  $\theta$  that describes the respiratory motion of the heart, where  $\theta$  is a vector of 12 affine motion parameters. Denoting by  $s$  the respiratory surrogate signal and by  $I$  the echo imaging data, Bayes' law states that the posterior probability function is proportional to the product of the likelihood and prior probability functions

$$p(\theta|I, s) = \frac{p(I|\theta, s) \cdot p(\theta|s)}{p(I|s)}. \quad (4.1)$$

The prior probability function  $p(\theta|s)$  represents the degree of certainty about the respiratory motion  $\theta$  given the surrogate  $s$ , before the echo images are considered. The prior is computed from the affine motion model as a function of the surrogate (see Section 4.2.3). The likelihood  $p(I|\theta, s)$  represents the probability of the echo image  $I$  given the affine transformation  $\theta$  and surrogate  $s$ . Thus, the likelihood represents the information carried by the new data, i.e. the real-time echo imaging data  $I$ . As is common in Bayesian image analysis (Geman and McClure, 1985; Hanson, 1993), the simplifying assumption that the normalising factor  $p(I|s)$  has a uniform distribution is adopted. The desired affine motion estimate  $\hat{\theta}$  is obtained in a MAP manner,

$$\hat{\theta} = \arg \max_{\theta, s} \{p(\theta|I, s)\}. \quad (4.2)$$

The parameters  $\theta$  and the surrogate  $s$  are optimised to maximise  $p(\theta|I, s)$  given the echo image  $I$ . The prior and the likelihood terms are now described in the following Sections.

### 4.2.3 Prior Probability

The prior probability is formed from the MRI-derived motion model. To build such a model, affine intensity-based registrations between a reference end-exhale dynamic 3D MRI image and the remaining dynamic 3D MRI images (see Section 4.3.1) are

performed. To constrain the registration to the heart only, a manually positioned ellipsoidal mask covering the four cardiac chambers was employed. This registration process results in 12 affine parameters for each dynamic image.  $2^{nd}$  order polynomial curves are fitted in a least-squares sense to each affine parameter as a function of the respiratory surrogate signal, as in King et al. (2009a). Given a value  $s$  of the surrogate acquired in the intra-procedure setting, the MRI-derived motion model outputs a 12 parameter affine transformation, denoted by  $\tilde{\boldsymbol{\theta}}(s)$ .

To incorporate a measure of uncertainty into the motion estimates made by the motion model, Gaussian distributions are fitted to the variations of each of the 12 affine parameters away from the model estimate  $\tilde{\boldsymbol{\theta}}(s)$ . An example of model fitting and a Gaussian function is shown in Figure 4.2 for the  $1^{st}$  affine parameter, i.e. AP translation. The peak of the Gaussian corresponds to the fitted value  $\tilde{\theta}_1(s)$  while the variance  $\sigma_{p_1}^2$  is a function of the residuals of the fitting method and the surrogate  $s$ .

As a simplifying assumption, the 12 affine parameters are considered to be statistically independent, so the prior probability is given by the product of the 12 Gaussian distributions,

$$p(\boldsymbol{\theta}|s) = \prod_i \frac{1}{\sqrt{2\pi\sigma_{p_i}^2(s)}} e^{-\frac{(\theta_i - \tilde{\theta}_i(s))^2}{2\sigma_{p_i}^2(s)}}, \quad i = 1, \dots, 12. \quad (4.3)$$

where  $\theta_i$  denotes the  $i^{th}$  affine parameter and  $\sigma_{p_i}^2(s)$  is the variance function for the  $i^{th}$  parameter. In the following,  $\mathbf{y}_i$  denotes the observations of the  $i^{th}$  parameter  $\theta_i$  (i.e. the motion estimates from the dynamic images). For instance, Figure 4.2(a) shows the observations of the first affine parameter  $\mathbf{y}_1$  as a function of the surrogate  $s$ , while Figure 4.2(d) shows the probability density function for  $\theta_1$ . Note that the variance  $\sigma_{p_i}^2$  varies as a function of the surrogate,  $s$ . This function is determined as follows.

The linear regression model solves

$$\mathbf{y}_i = \boldsymbol{\beta}_i X + \boldsymbol{\epsilon}_i, \quad i = 1, \dots, 12 \quad (4.4)$$

where  $X$  is the design matrix having  $[s^2 \ s \ 1]$  as column vectors and as many columns as the dynamic MRI images,  $\boldsymbol{\beta}_i$  are the regression coefficients of the polynomial function defining  $\tilde{\theta}_i(s)$  (see Figure 4.2(a)) and  $\boldsymbol{\epsilon}_i$  is the error term for the affine parameter  $i$  (Seber and Lee, 2003). A common assumption is that  $\boldsymbol{\epsilon}_i$  is normally distributed over the predictor variables (*homoscedasticity*). However, as can be seen in Figure 4.2(a)

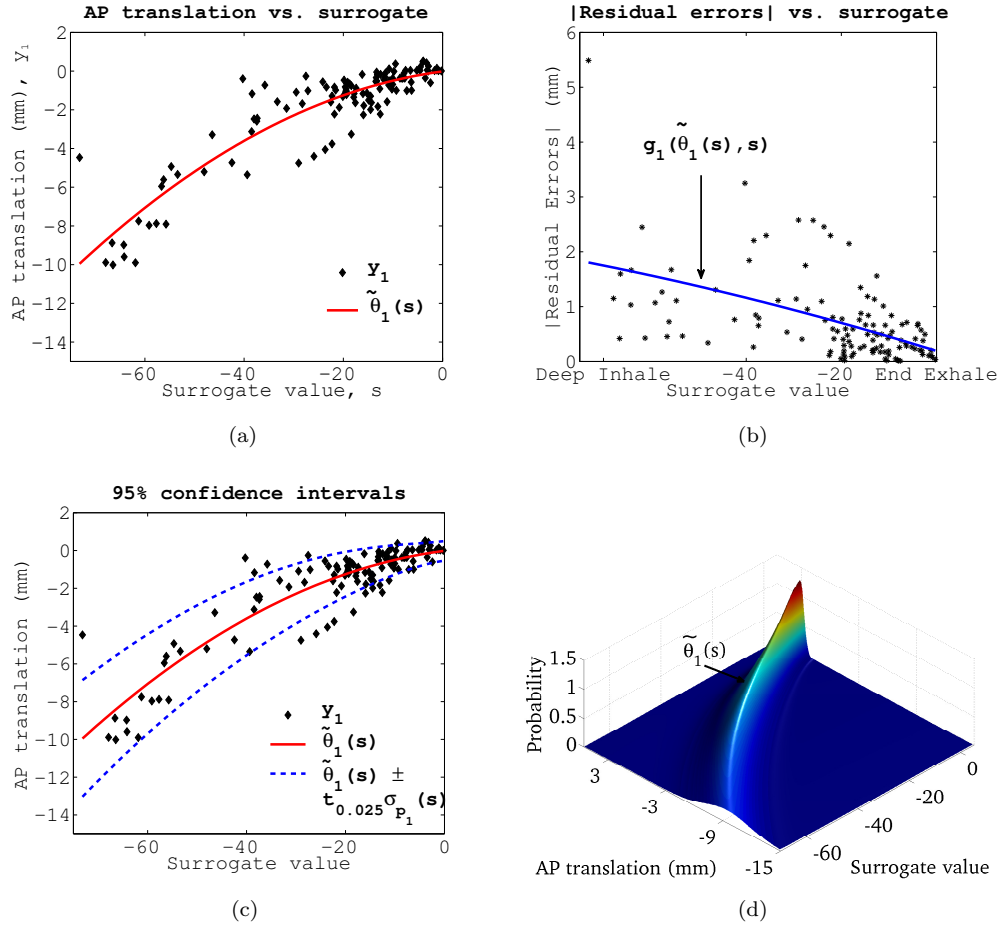


FIGURE 4.2: Example of Gaussian distribution function for a AP translation. (a) shows the 2<sup>nd</sup> order polynomial function  $\tilde{\theta}_1(s)$  that models the observations  $y_1$  as a function of the surrogate  $s$ . (b) shows the residual errors of  $\tilde{\theta}_1(s)$ , i.e.  $|y_1 - \tilde{\theta}_1(s)|$ . The curve  $g_1(\tilde{\theta}_1(s), s)$  is fitted to estimate how the standard deviation of the Gaussian distribution of the residual errors varies as a function of the surrogate  $s$ . 95% confidence intervals in prediction (dashed blue lines) (c) and the resulting probability distribution function for the AP translation (d) are shown.

and Figure 4.2(b), the residual distribution is not constant over the surrogate signal  $s$ , suggesting a correlation between the variance of the error  $\epsilon_i$  and the surrogate  $s$  (*heteroscedasticity*). The heteroscedastic behaviour of the affine parameters is due to respiratory motion variability, confirming that respiratory motion at inhale is less repeatable than at end-exhale (see Figure 4.2(b)). Therefore, a heteroscedastic variance function  $\sigma_{p_i}^2(s)$  is proposed

$$\sigma_{p_i}^2(s) = \mathbf{x}_0^T S_i \mathbf{x}_0 + g_i^2(\tilde{\theta}_i(s), s), \quad i = 1, \dots, 12. \quad (4.5)$$

$\sigma_{p_i}^2(s)$  is the variance of the error in prediction  $y_0 = \hat{\beta}_i \mathbf{x}_0$ , where the first term of

Equation (4.5) represents the error due to the data used to compute  $\hat{\beta}_i$  while the second term represents the variance of the error term  $\epsilon_i$ . For large sample sizes, the first term is negligible (Davidian and Carroll, 1987).  $S_i$  is the covariance matrix of the regression coefficients estimate  $\hat{\beta}_i$

$$S_i = \hat{\sigma}_i^2 (X^T X)^{-1}, \quad i = 1, \dots, 12 \quad (4.6)$$

where  $\hat{\sigma}_i^2$  is the mean squared error for the affine parameter  $i$ ,  $X$  is the design matrix,  $\mathbf{x}_0$  is the predictor vector for the new observation  $s_0$  ( $\mathbf{x}_0 = [s_0^2 \ s_0 \ 1]$ ) while  $g_i^2(\tilde{\theta}_i(s), s)$  describes the variance of the model error  $\epsilon_i$  as a function of  $s$ . As proposed by Davidian and Carroll (1987),  $g_i(\tilde{\theta}_i(s), s)$  is a function fitted to the absolute values of the residuals for the parameter  $i$  (see Figure 4.2(b)).  $2^{nd}$  order polynomial functions and least-squares fitting were again employed. This heteroscedastic model allows generation of a probability density function with a variance that depends on the surrogate value, as shown in Figure 4.2(d).

#### 4.2.4 Likelihood

The likelihood function  $p(I|\boldsymbol{\theta}, s)$  estimates the probability that the acquired image  $I$  would be generated by a given affine motion  $\boldsymbol{\theta}$ , which is related to  $s$ . To compute the likelihood, an end-exhale reference echo image  $I_{ref}$  was selected for each dataset (see Section 4.3). A Gaussian distribution based on the similarity measure between the new echo image  $I$  and the affine transformation of the reference echo image  $A(I_{ref}, \boldsymbol{\theta})$  was adopted,

$$p(I|\boldsymbol{\theta}, s) = \frac{1}{\sqrt{2\pi\sigma_l^2}} e^{-\frac{(NCC(A(I_{ref}, \boldsymbol{\theta}), I) - 1)^2}{2\sigma_l^2}} \quad (4.7)$$

where  $NCC(A(I_{ref}, \boldsymbol{\theta}), I)$  is the value of the normalised cross correlation similarity measure between the affine warping of the reference image  $A(I_{ref}, \boldsymbol{\theta})$  and the new echo image  $I$ , and  $\sigma_l^2$  is the likelihood variance. The more similar  $I$  and  $A(I_{ref}, \boldsymbol{\theta})$  are (i.e.  $NCC(A(I_{ref}, \boldsymbol{\theta}), I) \rightarrow 1$ ), the higher the value of the likelihood  $p(I|\boldsymbol{\theta}, s)$ . An automatic method for determining the optimal value of  $\sigma_l^2$  is now described.

#### 4.2.5 Optimisation of $\sigma_l^2$

The values of  $\sigma_l^2$  and  $\sigma_{p_i}^2$  affect the final motion estimate by changing the form, and therefore the peak, of the posterior probability function. For instance, using a non-informative prior, i.e. a uniform distribution function ( $\sigma_{p_i}^2 \rightarrow \infty$ ), would lead to a motion estimate completely driven by the likelihood function, whereas, on the other hand, greater values of  $\sigma_l^2$  would lead to a motion estimate tending to the model estimate  $\tilde{\theta}(s)$ .

As detailed in Section 4.2.3,  $\sigma_{p_i}^2$  is determined by the model data, i.e. the residuals of the modelling process. Therefore, the only free parameter that needs to be chosen is  $\sigma_l^2$ . A reasonable assumption is that the value of  $\sigma_l^2$  should reflect the quality of the acquired echo images,  $I$ . Ideally, if the echo imaging data were good enough to fully characterise the position of the heart, the prior knowledge from the model would not be necessary.

Quantification of image quality is a controversial and challenging topic, especially for echo imaging, due to its characteristic speckle pattern and many other artefacts such as shadowing, spatial distortion and multiple reflections. In this work, the relationship between  $\sigma_l^2$  and a differential signal-to-noise ratio (SNR) of the echo images is investigated, resulting in a simple empirical expression that can be used to determine the optimal value of  $\sigma_l^2$  before the Bayesian optimisation is performed.

Since the left ventricle (LV) was well imaged by both the dynamic MRI and echo images, the following differential SNR measure was utilised

$$SNR_d = \frac{\mu_{myo} - \mu_{blood}}{\sigma_{noise}}, \quad \sigma_{noise} = \frac{\sigma_{myo} + \sigma_{blood}}{2} \quad (4.8)$$

where  $\mu_{myo}$  and  $\sigma_{myo}$  are the mean and standard deviation of the LV myocardium voxel values while  $\mu_{blood}$  and  $\sigma_{blood}$  are the mean and standard deviation of the blood voxel values in the LV cavity. Higher values of  $SNR_d$  mean that LV myocardium voxels have more homogeneous values that differ markedly from voxels of the blood, therefore the echo image is highly informative. On the other hand, low values of  $SNR_d$  indicate poor contrast images with more heterogeneous values of the LV myocardium voxels.

For each echo image, the  $SNR_d$  is computed and the empirical model used to determine a value for  $\sigma_l^2$ . This value of  $\sigma_l^2$  is used in the optimisation of the posterior

probability. Section 4.3.5 provides further details on how the empirical model was used to determine  $\sigma_l^2$ .

### 4.3 Experiments

The proposed Bayesian technique was tested on simulated (see Section 4.3.3) and real echo imaging data (see Section 4.3.4). The use of simulated echo images, with realistic MRI-derived motion fields, enabled a thorough accuracy/robustness evaluation with known, gold-standard, motion fields. The use of real echo images enabled evaluation on data similar to those which would be acquired in a clinical environment, but without known, gold-standard, motion fields. In both cases, the prior probability term was formed from the MRI-derived affine motion model. In the following Section, MRI image acquisition is described. Echo image simulation/acquisition is described in Sections 4.3.3 and 4.3.4.

#### 4.3.1 MRI Acquisition

Details of the MRI sequences used to acquire the experimental data are provided in Appendix A. Each dataset consisted of a dynamic MRI scan to image the motion, as well as a high resolution static MRI scan (see below).

For this study, the subjects were asked to breathe in three different ways during the dynamic scan: normal, fast and deep breathing. This allowed respiratory variability to be captured and modelled. The overall acquisition of the dynamic MRI images lasted  $\sim 2 - 5$  minutes per volunteer. 13 volunteer datasets were processed: 9 datasets using simulated echo images (Vol. 1-9) and 4 datasets for real echo data (Vol. 13-16). See Appendix A for details of these datasets. For volunteers 1-4, the dynamic MRI sequence acquired 300 images (100 images for each different breathing pattern) while for the remaining volunteers Vol. 5-9 and Vol. 13-16, the dynamic sequence acquired 120 images (40 images for each breathing pattern) (see Table A.1). In the latter case, the number of images was sufficient to represent an adequate number of respiratory cycles (at least 4) for each breathing pattern.

In addition, for each dataset, a high resolution 3D image was acquired, which is a standard pre-procedure acquisition in many clinical protocols and provides high spatial resolution information about the anatomy and pathology of the heart. For the

simulated echo experiments, the high resolution MRI volume was segmented and used in the echo image simulation (see Section 4.3.3), while for the real echo experiments it was used for evaluation purposes (see Section 4.3.4). Also, the segmentation of the LV from the high resolution MRI image was employed for computing the  $\text{SNR}_d$  of the echo images (see Section 4.3.5).

### 4.3.2 Comparison of Estimation Techniques

To evaluate the performance of the proposed method, for both simulated and real echo experiments, the following motion estimation approaches were compared:

- (i) - *no estimate*: the reference end-exhale position is used as motion estimate for any inhale position;
- (ii) - *model-only*: a direct correspondence motion model estimate (King et al., 2009a). Given the surrogate value  $s$ , the motion estimate is  $\tilde{\theta}(s)$ . Details of which surrogate signals were used are provided in Sections 4.3.3 and 4.3.4;
- (iii) - *image-only*: as in King et al. (2010a), the estimate is given by the registration of the echo images only, without the constraints of a motion model. This approach corresponds to the Bayesian estimate using a non-informative prior. However, unlike a purely image-only registration,  $\tilde{\theta}(s)$  was provided as a starting estimate for the optimisation algorithm since the small FoV and the even smaller overlapping region of  $A(I_{ref}, \theta)$  and  $I$  made the optimisation unstable. A hill climbing optimisation algorithm was used;
- (iv) - *PCA-based model*: similar to Schneider et al. (2010) and King et al. (2012), the set of affine parameters  $\mathbf{y}_i$ ,  $i = 1, \dots, 12$  is assumed to lie on a linear sub-manifold having dimensionality  $f \leq F$ ,  $F = 12$ . Linear PCA is applied to find the first  $f$  eigenvalues  $\lambda_1 \geq \dots \geq \lambda_f$  and corresponding eigenvectors  $\mathbf{v}_1, \dots, \mathbf{v}_f$  that capture at least 95% of the overall variance  $\sum_{j=1}^F \lambda_j$ . Denoting by  $\mathcal{Y} = [\mathbf{y}_1; \dots; \mathbf{y}_F]$  the  $F \times P$  matrix where  $F = 12$  and  $P = 300 - 1$  for Vol. 1-4 and  $P = 120 - 1$  for Vol. 5-9, singular value decomposition (SVD) is applied to the covariance matrix  $\Sigma = \mathcal{Y}_c \mathcal{Y}_c^T$ , where  $\mathcal{Y}_c = \mathcal{Y} - \bar{\mathcal{Y}}$  is centred with respect to the F-component mean vector  $\bar{\mathcal{Y}} = \frac{1}{P} \sum_{h=1}^P \mathcal{Y}$ . Given the difference in units of the 12 affine parameters, the values of each affine parameter are normalised

with respect to their standard deviation before PCA is applied. The PCA-based model estimate  $\hat{\boldsymbol{\theta}}_{PCA}$  is obtained by optimising the f-component vector  $\boldsymbol{\gamma}$  of weights that maximises

$$\hat{\boldsymbol{\theta}}_{PCA}(\boldsymbol{\gamma}) = \arg \max_{\boldsymbol{\gamma}} \{NCC(A(I_{ref}, \boldsymbol{\theta}_{PCA}(\boldsymbol{\gamma})), I)\}, \quad (4.9)$$

where  $\boldsymbol{\theta}_{PCA}(\boldsymbol{\gamma}) = \bar{\boldsymbol{\mathcal{Y}}} + \sum_{j=1}^f \gamma_j \mathbf{v}_j$ . A hill climbing optimisation algorithm was used;

- (v) - *simple model and image*: using a method similar to that described in Blackall et al. (2005) and King et al. (2010a), the estimate is obtained by maximising  $NCC(A(I_{ref}, \boldsymbol{\theta}), I)$  but constraining  $\boldsymbol{\theta}$  to lie on the model, that is

$$\hat{\boldsymbol{\theta}} = \tilde{\boldsymbol{\theta}}(\hat{s}), \quad \hat{s} = \arg \max_s \{NCC(A(I_{ref}, \tilde{\boldsymbol{\theta}}(s)), I)\}. \quad (4.10)$$

This approach corresponds to an indirect correspondence model, without providing either a measure of uncertainty nor deviating from  $\tilde{\boldsymbol{\theta}}(s)$ . A hill climbing optimisation algorithm was used;

- (vi) - *Bayesian*: the proposed motion estimate (see Equation (4.2)). As described in Section 4.3.5, the optimal value of the likelihood variance was determined by means of Equation (4.12) for all simulated and real echo images. In the optimisation, the model-only estimate  $\tilde{\boldsymbol{\theta}}(s)$  was used as a starting estimate. A hill climbing algorithm was used to estimate  $\hat{\boldsymbol{\theta}}$ .



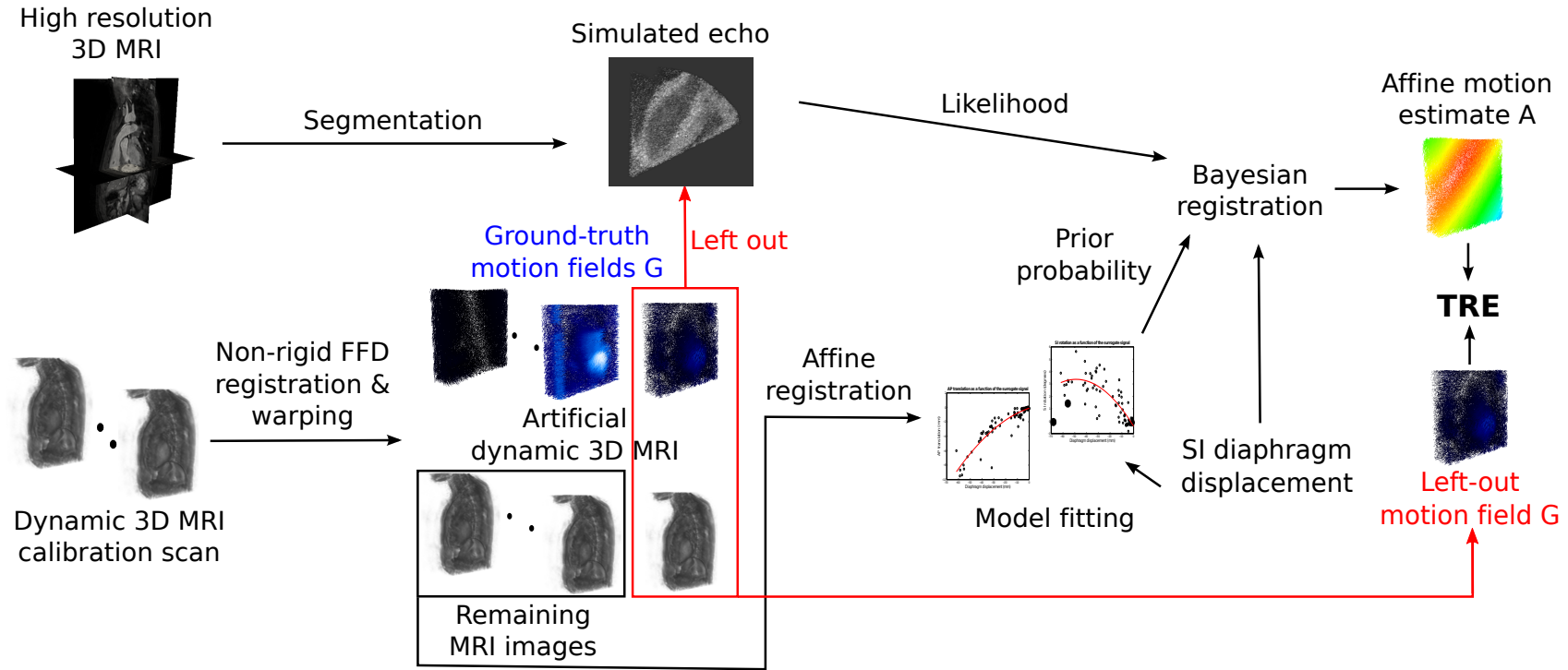


FIGURE 4.3: Overview of the echo simulation and leave-one-out validation framework. Real dynamic MRI images are non-rigidly registered to a dynamic end-exhale reference image, and warped using the resulting motion fields to create artificial, but realistic, dynamic MRI images with known gold standard motion fields. Each artificial MRI image is left out in turn. The non-rigid motion field of the left out dynamic is combined with a segmented high resolution MRI image to produce a simulated 3D echo image. By using an intensity-based affine registration algorithm, the remaining artificial MRI images are used to form the motion model. To assess the accuracy, the affine motion fields  $A$  are estimated by the model and compared to the left-out ground truth non-rigid motion fields  $G$  in order to compute TREs in estimation accuracy.

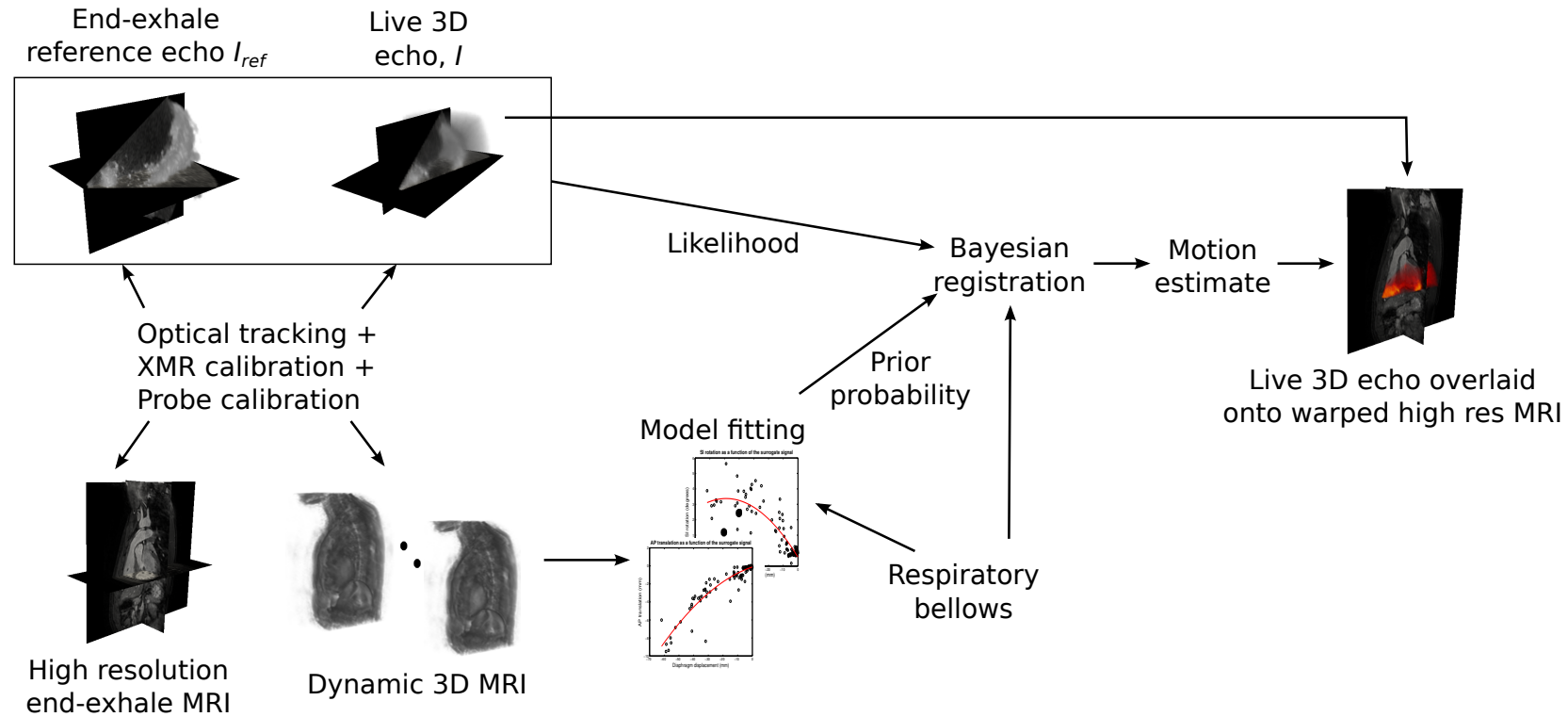


FIGURE 4.4: Workflow employed to evaluate the technique on real echo imaging data. The dynamic MRI images were used to build the affine motion model. A respiratory bellows was employed as surrogate signal. The MRI-derived affine motion model formed the prior probability, whereas the full-volume 3D reference and 3D live echo images formed the likelihood term. Optical tracking together with calibration of the XMR catheter laboratory and the echo probe provided the rigid transformation between the MRI and the echo imaging coordinate system. For evaluation purposes, the high resolution MRI image was transformed to the dynamic MRI coordinate system and then warped with the motion estimates produced by the different approaches compared (see Section 4.3.2). The corresponding live 3D echo was overlaid onto the warped MRI image and misalignment was visually assessed.

### 4.3.3 Evaluation Using Real MRI, Simulated Echo Data

The Bayesian motion model was evaluated on simulated echo images derived from the high resolution MRI image and the MRI dynamic calibration scan employed to build the model. A block diagram illustrating the evaluation using simulated echo imaging with realistic, gold-standard, motion fields is shown in Figure 4.3.

The SI displacement of the dome of the left hemi-diaphragm was chosen as the respiratory surrogate signal and automatically extracted from all dynamic MRI images, simulating an MRI navigator echo (Savill et al., 2011).

The dynamic MRI image having the highest SI displacement was selected as the end-exhale reference image for registration. To have a gold-standard set of deformation fields to simulate echo images and validate the motion model, a free-form deformation FFD registration algorithm (Buerger et al., 2011) was used to register each dynamic MRI image to the end-exhale reference image. The non-rigid registration resulted in a set of ground truth deformation fields  $G$  and the corresponding ‘artificial’ set of warped 3D MRI images was used to build the motion model and form the prior probability (see Section 4.2.3). Thus, in this evaluation, the intensity-based affine registration was applied to the ‘artificial’ set of warped 3D MRI images instead of the original dynamic sequence. This approach was employed to obtain a gold standard set of motion fields where all deformations were known and used for accuracy/robustness evaluation.

3D echo images were simulated using the US propagation model proposed in Rijkhorst et al. (2010). This method requires maps of the 3D acoustic impedance  $Z$  and absorption coefficients  $\alpha$  corresponding to different tissues. The high resolution 3D MRI image was manually segmented to differentiate blood pool, myocardium, liver and lungs. Due to poor contrast, it was not possible to segment the ribs out of the high resolution volume.

The values of the acoustic impedance and absorption coefficients were assigned according to Rijkhorst et al. (2010) and Baun (2010) and are reported in Table 4.1. The echo simulation method uses a Lambertian reflection model simulating reflection, absorption and transmission ratios along each ray direction. The effects of finite beam width in the elevational direction and of multiple active transducer elements are also simulated. To simulate realistic speckle noise, two different textures, one for the myocardium and one for the other tissues, were used. These textures were obtained using a texture quilting technique (Efros and Freeman, 2001) applied to real 3D echo patches

	blood	heart	muscle	lungs	liver
$Z$ ( $10^6 \text{ kg s}^{-1} \text{ m}^{-2}$ )	1.61	1.71	1.70	0.50	1.65
$\alpha$ ( $\text{dB cm}^{-1}$ )	0.18	1.10	1.00	12.00	0.94

TABLE 4.1: Values of the acoustic impedance  $Z$  and absorption coefficient  $\alpha$  used for simulating B-mode echo images.

of the myocardium and the blood pool, acquired from a volunteer. To obtain a  $\text{SNR}_d$  comparable to real echo images, Gaussian noise was added to the simulated echo images based on measurements of real echo images, as described in Section 4.3.5.

The high resolution MRI volume was rigidly transformed to the coordinate system of the dynamic reference MRI image and the segmentation was then warped to each dynamic inhale position using the FFD motion fields from the non-rigid registrations. The acoustic impedance and absorption maps were assigned to the warped segmentations and 3D echo images were simulated. A trans-apical acoustic window was adopted with a FoV that is typical of images acquired in real-time from a modern echo machine (see Section 4.3.4). The US simulation of the dynamic end-exhale reference MRI image was employed as the echo reference image  $I_{ref}$  in the computation of the likelihood term (see Section 4.2.4).

Nine volunteer datasets were processed. A leave-one-out framework was employed to evaluate the Bayesian approach using simulated echo images. This means that, for each simulated echo image, the corresponding non-rigid motion fields and ‘artificial’ MRI image were not utilised for building the motion model and forming the prior probability (see Section 4.2.3).

Given the availability of the ground truth non-rigid motion fields  $G$ , Target Registration Errors (TREs) were used to assess the accuracy of the Bayesian model and the other comparative approaches (see Section 4.3.2). A set of  $H$  landmarks ( $\approx 35,000$ ) was positioned on a regular Cartesian grid within a manually delimited elliptical mask covering the four chambers of the heart (see Section 4.2.3) in the end-exhale reference image,  $\vec{x}_h, 1 \leq h \leq H$ . Using the left-out ground-truth motion fields  $G$ , the set of landmarks was warped in turn to each of the  $P$  dynamic MRI inhale positions, with  $P$  being either  $P = 300 - 1$  or  $P = 120 - 1$  (see Section 4.3.1). Denoting by  $A$  the affine transformation estimated by each of the techniques compared, the error in estimation

was computed as

$$\|G_p(\vec{x}_h) - A_p(\vec{x}_h)\|, \quad 1 \leq h \leq H, \quad 1 \leq p \leq P. \quad (4.11)$$

Median and 95<sup>th</sup> quantiles were adopted as statistics because of the skewness of the error distributions. Results are reported in Section 4.4.1.

#### 4.3.4 Evaluation Using Real MRI, Real Echo Data

To evaluate the Bayesian motion model on real live echo images, experiments were carried out in an XMR catheterisation suite (Rhode et al., 2003, 2005). Please refer to Section A.2 for details of the echo acquisition setup and the acquired echo images.

While in the case of simulated echo images the SI displacement of the diaphragm was employed as a respiratory surrogate signal (see Section 4.3.3), for real echo images a respiratory bellows placed on the chest of the subjects was used to form the prior probability  $p(\theta|s)$  and to optimise the posterior probability  $p(\theta|I, s)$ . The respiratory bellows signal can be easily acquired during the procedure and used as the intra-procedure surrogate signal  $s$  (see Figure A.1).

Since tracking data, echo imaging data and respiratory bellows data were acquired on different machines, synchronisation of the machine clocks and time stamping of all data was performed to ensure temporal correspondence.

Four volunteer datasets were acquired. For each dataset, 4 standard 3D echo images were acquired during end-exhale breath-hold and 12 sequences of free-breathing live 3D echo images were acquired. Of the 12 free-breathing sequences, 6 sequences were acquired during normal breathing, 3 during fast breathing and 3 during deep breathing. Each sequence lasted approximately 4 seconds and live echo images were streamed at a rate of 14 images per second. However, since the MRI-derived motion model describes the heart's position at end-diastole, the echo images were manually retrospectively gated at end-diastole, resulting in 4 to 6 live echo images per sequence. Modified parasternal acoustic windows were used and the standard end-exhale echo image covering a similar FoV to the live images was employed as the reference image for the computation of the likelihood term (see Section 4.2.4).

By using the MRI to patient rigid transformation, the standard full-volume reference echo images and the live echo images were transformed to the coordinate system

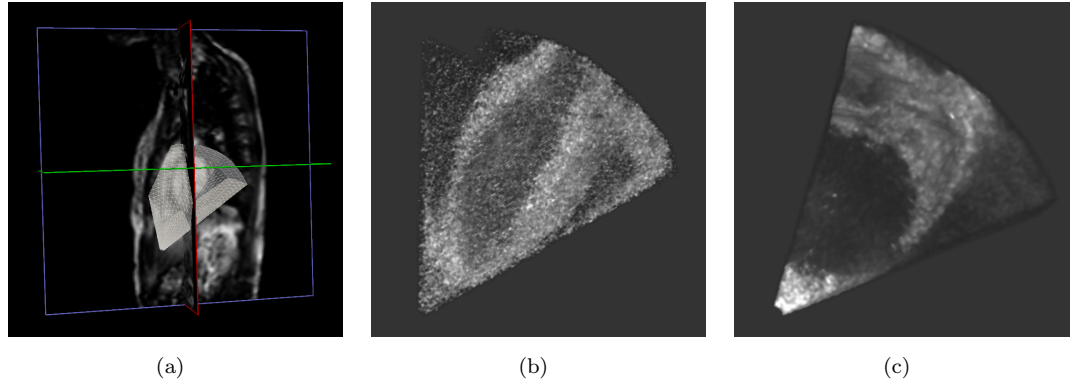


FIGURE 4.5: (a) Example of 3D live ultrasound beam overlaid onto a dynamic MRI image; volume rendering of a simulated (b) and live (c) 3D echo image.

of the dynamic MRI images, where the affine motion model was represented. Given the value of the respiratory bellows corresponding to each live echo image, the respiratory position was estimated by each of the different estimation methods (see Section 4.3.2).

To assess the accuracy of the motion estimates, the high resolution MRI image was first rigidly transformed to the dynamic MRI coordinate system and then warped to the affine inhale position estimated by each approach. The corresponding live echo image was overlaid onto the warped high resolution MRI image and the maximum misalignment error of corresponding anatomical landmarks (e.g. inter-ventricular septum, LV posterior wall) was visually assessed. As they had higher image contrast, anatomical landmarks on the lateral/posterior LV wall were mainly considered for error assessment, while the position of the septum was used to assess the overall realism of the motion estimate. The GIMIAS open-source visualisation software (Larrabide et al., 2009) was used to estimate the misalignment. Three independent observers were asked to assess 200 pairs of images (i.e. 50 pairs of images for each volunteer, 10 for each of the estimation techniques compared (see Section 4.3.2)) randomly selected and measure the maximum misalignment error. Observers were also asked to report any obviously unrealistic motion estimations. The evaluation assessment was blinded, that is the observers were presented with the image pairs without knowing which technique they were produced with. An example of misalignment assessment is shown in Figure 4.6. Results are reported in Section 4.4.

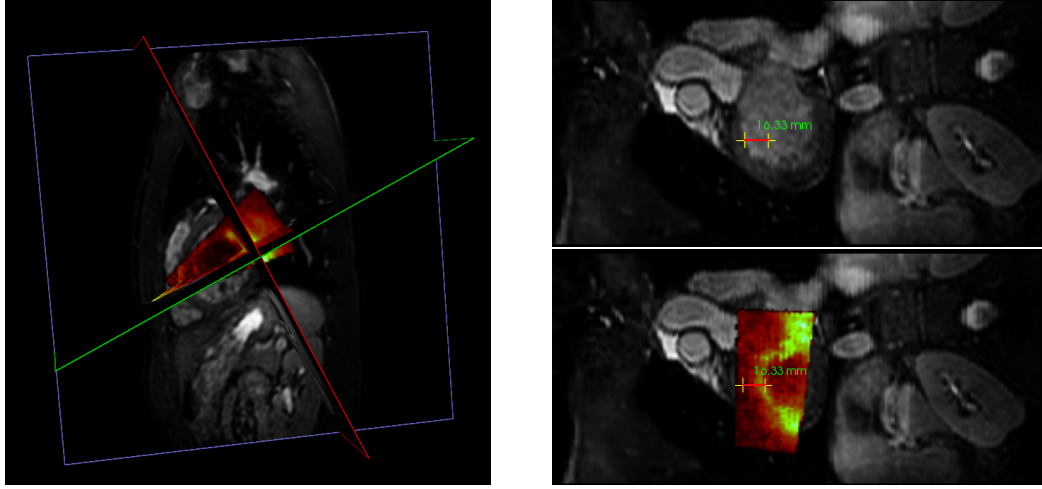


FIGURE 4.6: Example of evaluation assessment using GIMIAS. The 3D live echo image is overlaid onto the transformed high resolution MRI image and the maximum misalignment error (shown in green) is measured. 3D plane orientation is shown on the left. On the right, error assessment is shown on the transformed high resolution MRI image (top) and on the 3D live echo (bottom) shown in a modified coronal view.

#### 4.3.5 Determination of the Optimal $\sigma_l^2$

To automatically determine the optimal value of  $\sigma_l^2$ , a simple linear model based on the  $SNR_d$  of the echo images was employed. This means that each echo image will potentially have a different value of  $\sigma_l^2$  used in the optimisation, depending on the quality of the image. The formation of this simple model which is based on the simulated and real echo images is now described.

Firstly, the  $SNR_d$  for each echo image has to be computed. For simulated echo images (see Section 4.3.3), LV myocardium and blood were known from the segmentation of the high resolution MRI image used for echo simulation (see Section 4.3.3). For each dataset, two inhale echo images were selected and Gaussian noise having different values of variance was added in the simulation process to vary the  $SNR_d$  of the simulated images. Twelve evenly distributed values of  $\sigma_l^2$  were selected and the Bayesian estimation for each image and for each value of  $\sigma_l^2$  was computed. For each image, the value of  $\sigma_l^2$  producing the lowest TRE (see Section 4.3.3) was determined.

For real echo images (see Section 4.3.4), LV myocardium and blood were segmented from the high resolution MRI image and transformed to the dynamic MRI coordinate system. Given the availability of the image-only registration between the full-volume reference echo and the live echo images (see Section 4.3.2), the LV segmentation was warped to each live echo image using the image-only registration and the  $SNR_d$  was

computed for each live echo image. For each of the four volunteers, approximately 15 images were selected and, as for the simulated echo, 12 evenly distributed values of  $\sigma_l^2$  were selected and the Bayesian estimation computed. The value of  $\sigma_l^2$  generating the lowest misalignment error (see Section 4.3.4) was selected. Figure 4.7 shows the

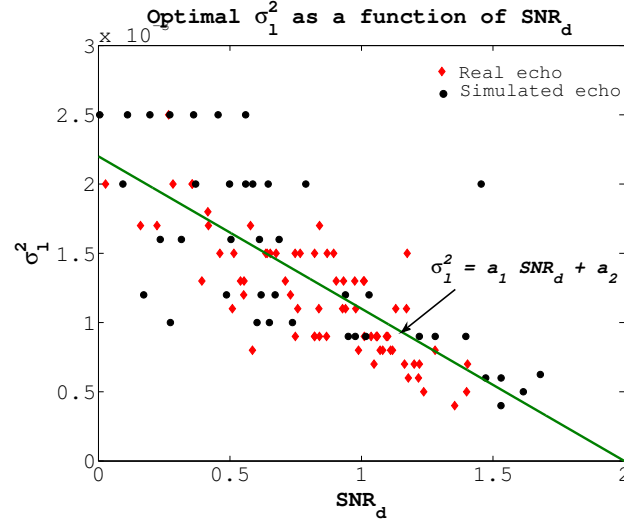


FIGURE 4.7: Distribution of the best values of  $\sigma_l^2$  as a function of  $SNR_d$ . Black circles refer to simulated echo images while red diamonds refer to real echo images.

distribution of  $\sigma_l^2$  producing the best results for simulated echo images and real echo images as a function of the  $SNR_d$ . As can be seen, the overlap of the two distributions is high, suggesting good similarity between the simulated and real echo images. A linear function was employed to describe the relationship between  $\sigma_l^2$  and  $SNR_d$

$$\sigma_l^2 = a_1 \cdot SNR_d + a_2. \quad (4.12)$$

A linear function represented the best trade-off between the quality of fit and the simplicity of representation. Furthermore, the possible range of  $SNR_d$  values for real echo images ( $0 < SNR_d < 1.5$ ) and simulated echo images ( $1 < SNR_d < 1.3$ ) ensured  $\sigma_l^2 > 0$ .

To separate data used for parameter estimation and data used for evaluation,  $a_1$  and  $a_2$  were computed using a leave-one-out test, which means that, for any given dataset, the corresponding  $a_1$  and  $a_2$  were fitted without considering the best  $\sigma_l^2$  derived from the same dataset. A least-squares fitting was used and typical values were  $a_1 = -1.1 \cdot 10^{-3}$  and  $a_2 = 2.2 \cdot 10^{-3}$ , with a correlation coefficient of 0.75 (see Figure 4.7).



## 4.4 Results

Results achieved for simulated and real echo images are presented in Section 4.4.1 and 4.4.2, respectively. The 50<sup>th</sup> and 95<sup>th</sup> quantile values rather than the mean and standard deviation values are employed as statistics since the error distributions were skewed and non-Gaussian.

### 4.4.1 Simulated Echo Data

The median and 95<sup>th</sup> quantile of the TREs for each of the estimation techniques compared are summarised in Figure 4.8 and reported in Table 4.2.

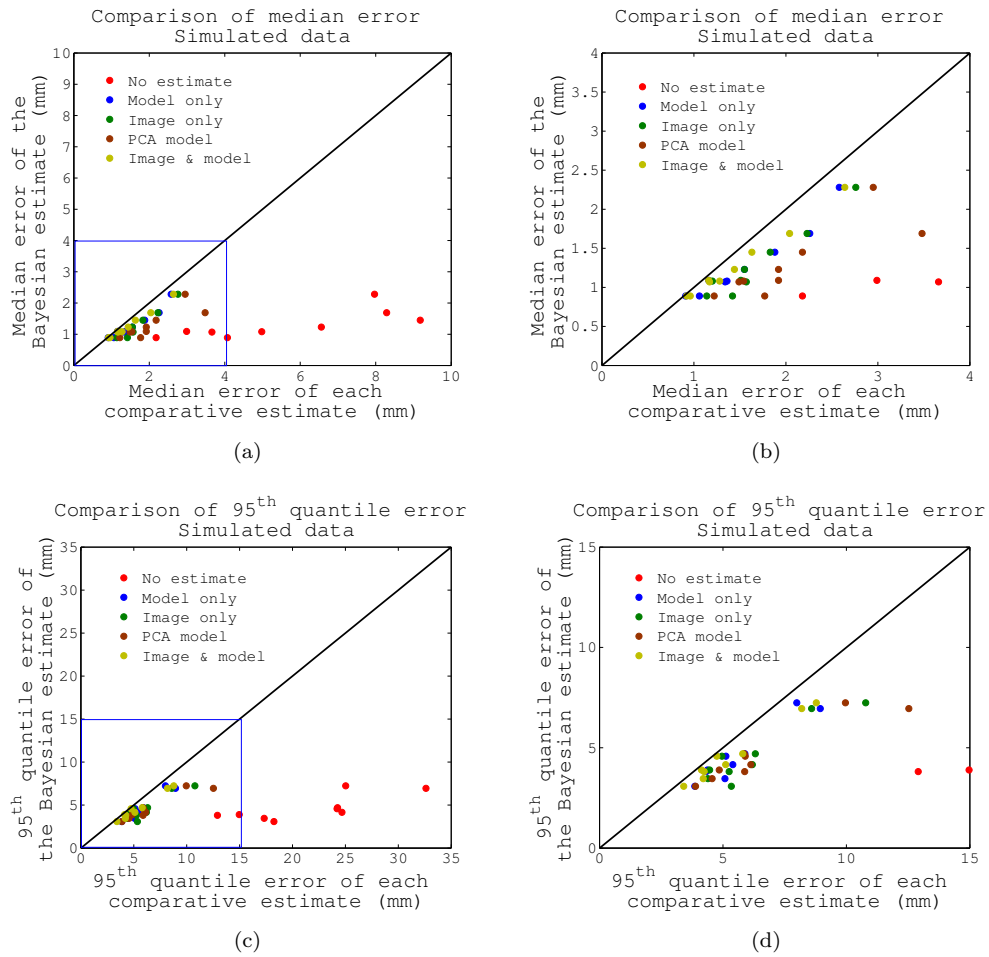


FIGURE 4.8: Accuracy error comparison between the Bayesian estimate ( $v_i$ ) (vertical axis) and each comparative estimate (horizontal axis) for simulated echo images. (a) Median error and (c) 95<sup>th</sup> quantile error. Since there are some very high errors with no motion estimation, (b) and (d) show the error distributions in the blue boxes of Figure (a) and (c), respectively. The estimation error of the Bayesian technique was lower than any other comparative estimation technique.

For each of the 9 datasets considered, the accuracy error achieved by the Bayesian method (*vi*) was lower than any other comparative approach. To summarise the performance of the Bayesian estimation, the mean/max improvements of median/95<sup>th</sup> quantile were computed. The mean is the average improvement of the median error over all 9 datasets. The mean/max improvements achieved were 10.6%/18.9% over the best comparative technique. The best comparative technique was defined to be the technique having the lowest 95<sup>th</sup> quantile, which was, for 8 volunteers out of 9, the combination of a simple model and image data (*v*). Mann-Whitney U-tests were performed between the Bayesian error distribution and the best comparative technique. For all volunteers, statistical significance was found with  $p < 0.05$ .

#### 4.4.2 Real Echo Data

Table 4.3 reports the median and 95<sup>th</sup> quantile of the maximum misalignment error measured by the three independent observers. Given the lower number of samples for real data compared to simulated data, rather than median/95<sup>th</sup> quantile, all misalignment errors for Vol. 13-16 are shown in Figure 4.9.

As for simulated echo images, the Bayesian method (*vi*) outperformed all the other estimation methods, with mean/max improvements in estimation accuracy of 20.8%/41.5% over the best comparative approach. The best comparative technique was again defined as the technique having the lowest 95<sup>th</sup> quantile. The mean value is the average improvement of the median error over the 4 datasets. Mann-Whitney U-tests between the Bayesian results and the best comparative results confirmed statistical significance with  $p < 0.05$  for Vol. 13 and Vol. 14. The highest XMR-based MRI-to-physical registration and echo probe calibration errors were found for Vol. 15, which might explain the poor performance of all motion estimation techniques for this subject.

Unrealistic motion estimates were reported for 26 out of 40 image-only (*iii*) estimates, while no unrealistic estimates were generated by the other estimation techniques. At least one unrealistic image-only motion estimate was reported for each dataset. An example of an unrealistic image-only estimate is shown in Figure 4.10. For Vol. 13, one image-only registration resulted in a completely wrong estimate, with misalignment errors up to 100mm.

Figure 4.11 shows the comparison of the different motion estimates for a live 3D echo image. The segmentation of the LV myocardium is transformed using the different

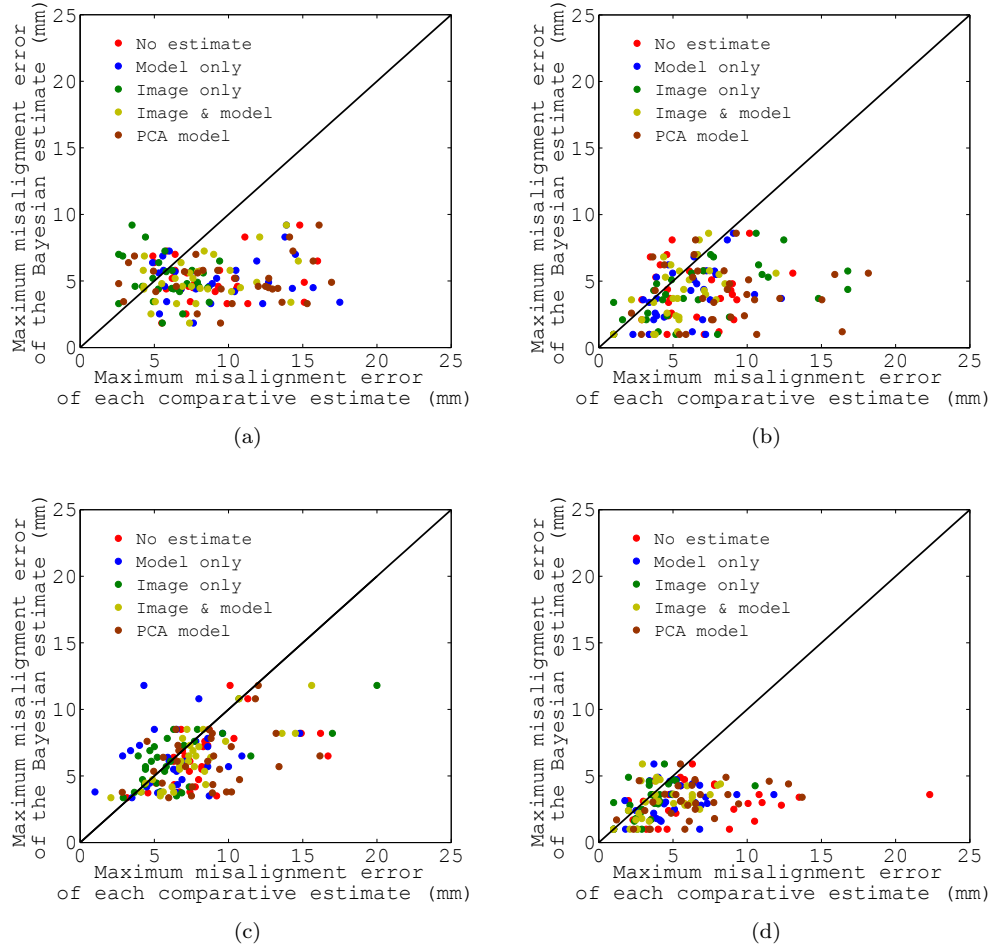


FIGURE 4.9: Maximum misalignment error comparison between the Bayesian estimate ( $vi$ ) (vertical axis) and each comparative estimate (horizontal axis). All misalignment errors are shown for (a) Vol. 13, (b) Vol. 14, (c) Vol. 15 and (d) Vol. 16. For clarity of visualisation, three misalignments errors of the image-only estimation (48.8mm, 64mm and 100mm) for Vol. 13 (a) are not reported.

respiratory motion estimates and overlaid onto the corresponding live 3D echo image. A cross-section is used to visualise the misalignment error. For no motion estimate ( $i$ ), model-only ( $ii$ ), PCA-based model ( $iv$ ) and simple model and image ( $v$ ) estimation techniques residual misalignment errors can be seen at the posterior LV wall (bottom arrow) and inter-ventricular septum (top arrow). In the LV wall, the brightest voxels in the echo image represent the boundary between the LV myocardium and the left lung, therefore the external surface of the LV myocardium should be aligned with the boundary reflection. The lower misalignment errors are shown by the image-only ( $iii$ ) 4.11(c) and Bayesian ( $vi$ ) 4.11(f) estimation techniques. Figure 4.10(a) shows the cardiac roadmap as segmented from the high resolution MRI, while Figure 4.10(b)

shows the cardiac surfaces as estimated by the image-only (*iii*) registration shown in Figure 4.11(c). The Bayesian motion estimation shows the best alignment while maintaining a realistic motion estimate (see Figures 4.10(c) and 4.11(f)).

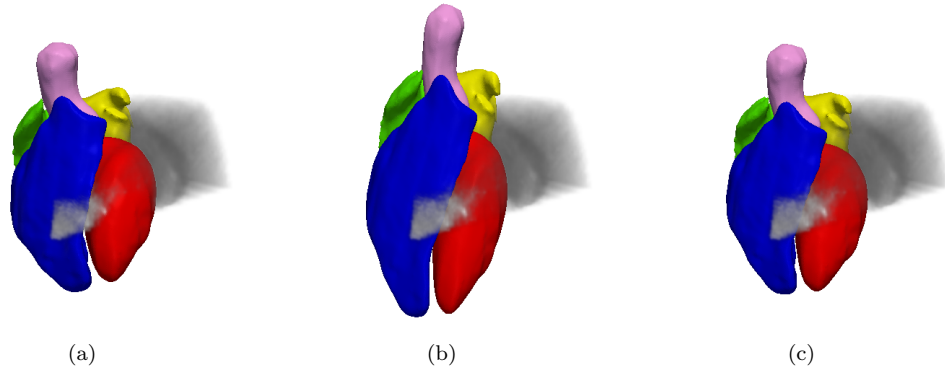


FIGURE 4.10: (a) Segmentation of the heart as derived from the high resolution MRI image (*i*); (b) unrealistic image-only motion estimate (*iii*) and (c) Bayesian motion estimate (*vi*) for the same live echo image.

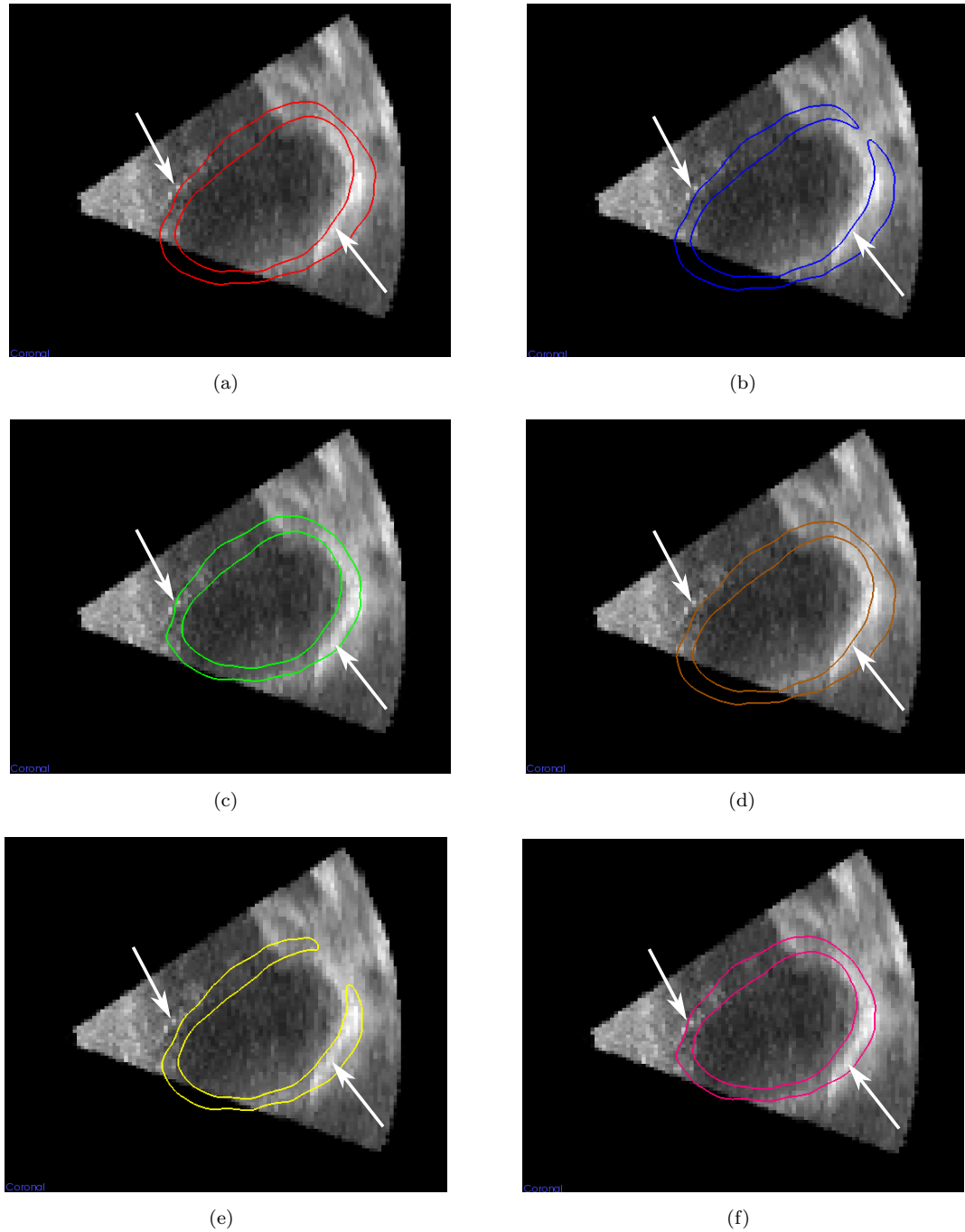


FIGURE 4.11: The motion estimates of the LV myocardium (coloured surfaces) are overlaid onto the corresponding live 3D echo image. Cross-sections are used to visualise the residual misalignment error. (a) No motion estimation (*i*), (b) model-only estimation (*ii*), (c) image-only estimation (*iii*), (d) PCA-based model (*iv*), (e) simple model and image estimation (*v*) and (f) Bayesian estimation (*vi*) are shown.

Subject	Median / 95 <sup>th</sup> quantile target error (mm)						Improv. (%)
	<i>No estimate</i> (i)	<i>Model only</i> (ii)	<i>Image only</i> (iii)	<i>PCA model</i> (iv)	<i>Image &amp; Model</i> (v)	<i>Bayesian</i> (vi)	
Vol. 1	2.99 / 24.26	1.16 / 5.89	1.51 / 6.31	1.92 / 5.86	1.16 / 5.80 †	1.09 / 4.70	6.0 / 18.9
Vol. 2	3.66 / 12.91	1.34 / 4.32	1.57 / 5.25	1.49 / 5.88	1.17 / 4.24 †	1.07 / 3.81	8.5 / 10.1
Vol. 3	4.07 / 18.25	1.06 / 3.86	1.14 / 5.34	1.22 / 3.89	0.96 / 3.41 †	0.89 / 3.08	7.3 / 9.7
Vol. 4	4.98 / 14.97	1.36 / 4.37	1.20 / 4.46	1.54 / 4.85	1.28 / 4.13 †	1.08 / 3.89	15.6 / 5.8
Vol. 5	7.97 / 25.03	2.58 / 7.99 †	2.76 / 10.78	2.95 / 9.96	2.64 / 8.78	2.28 / 7.24	11.6 / 9.4
Vol. 6	8.29 / 32.62	2.26 / 8.94	2.23 / 8.59	3.48 / 12.53	2.04 / 8.19 †	1.69 / 6.95	17.2 / 15.1
Vol. 7	9.18 / 24.68	1.88 / 5.40	1.83 / 6.19	2.18 / 6.13	1.63 / 5.11 †	1.45 / 4.16	11.0 / 18.6
Vol. 8	6.56 / 24.21	1.55 / 5.12	1.55 / 4.96	1.92 / 5.90	1.44 / 4.75 †	1.23 / 4.58	14.6 / 3.6
Vol. 9	2.18 / 17.33	0.91 / 5.08	1.42 / 4.39	1.77 / 4.56	0.92 / 4.20 †	0.89 / 3.46	3.4 / 17.6

TABLE 4.2: Evaluation results of Bayesian estimation using simulated echo images. Median and 95<sup>th</sup> quantile values of TRE are reported. The last column shows the percentage improvement in median and 95<sup>th</sup> quantile target error of the Bayesian technique over the best comparative estimate, denoted by a †.

Subject	Median / 95 <sup>th</sup> quantile maximum error in misalignment (mm)						Improv. (%)
	<i>No estimate</i> (i)	<i>Model-only</i> (ii)	<i>Image-only</i> (iii)	<i>PCA model</i> (iv)	<i>Image &amp; Model</i> (v)	<i>Bayesian</i> (vi)	
Vol. 13	7.65 / 15.10	8.75 / 15.70	6.19 / 64.00	9.87 / 15.92	7.70 / 14.20 †	4.85 / 8.30	37.0 / 41.5
Vol. 14	5.52 / 10.16	6.35 / 10.50	5.98 / 16.78	8.09 / 16.17	5.35 / 8.50 †	3.85 / 8.10	28.0 / 4.7
Vol. 15	7.87 / 16.20	6.48 / 10.90 †	5.74 / 17.00	8.75 / 13.31	7.31 / 14.50	6.10 / 10.80	5.9 / 0.9
Vol. 16	5.66 / 13.5	4.65 / 9.30	3.51 / 5.19 †	5.90 / 12.19	3.87 / 8.00	3.07 / 4.90	12.5 / 5.6

TABLE 4.3: Evaluation results of Bayesian estimation using real echo images. Median and 95<sup>th</sup> quantile values of the maximum misalignment error are reported. The last column shows the percentage improvement in median and 95<sup>th</sup> quantile target error of the Bayesian technique over the best comparative estimate, denoted by a †.

## 4.5 Discussion

In this Chapter, a novel Bayesian model for respiratory motion estimation and compensation in cardiac IGIs was presented. The method combines a MRI-derived affine motion model of the heart with intra-procedure live 3D echo in a Bayesian approach. The novelties of the proposed method lie in its probabilistic formulation, which embeds a measure of confidence in its estimates and resolves the uncertainty related to the variability of respiratory motion and the potentially conflicting information carried by the model and the imaging data. Moreover, the use of probability density functions overcomes the limitations of motion models proposed so far, allowing the Bayesian motion estimate to deviate from the predetermined direct correspondence model estimate. By determining the optimal value of the only free parameter  $\sigma_l^2$ , the Bayesian technique adapts automatically to the quality of the echo images.

Simulated echo images with realistic MRI-derived motion fields were employed to perform a thorough accuracy/robustness evaluation with known, gold-standard, motion fields. Results showed mean/max accuracy improvements in motion estimation of 10.6%/18.9% over the best comparative estimation technique. Although echo image artefacts such as spatial distortion and incidence angle were not included in the simulation process, the realism of the simulated echo images was improved by including real speckle textures and Gaussian noise. Even though  $\text{SNR}_d$  is a simple measure of echo image quality, the comparable  $\text{SNR}_d$  values achieved for simulated and real echo images suggest that similar image quality was achieved. The lack of the rib cage simulation was compensated by the selection of an echo beam positioning that resembled realistic acoustic windows.

Real echo imaging data enabled evaluation on data similar to those which would be acquired in a clinical environment. For the 4 volunteer datasets considered, results showed the Bayesian method to outperform all comparative approaches, producing the lowest misalignment errors with mean/max improvements in estimation accuracy of 20.8%/41.5%. Due to more sources of inaccuracy, such as errors in the probe and XMR suite calibration (Rhode et al., 2003, 2005; Ma et al., 2009), synchronisation, evaluation assessment and errors due to echo image artefacts not included in the simulation, errors were higher for real echo images compared to simulated echo. In addition, the respiratory bellows signal was subject to amplitude drifts, which directly affect direct

correspondence model estimates. Spirometry has also been proposed in the literature as a surrogate signal but is impractical to use in most cardiac interventions, causing high discomfort to the patient. Echo images employed in this study were acquired in a supine position, where the position of the heart is not ideal to be imaged. Better quality echo images could further improve the Bayesian motion estimates.

This work has also provided a comparative study on motion estimation techniques available in the literature and reviewed in Section 3.2. Results from both simulated and real echo images have confirmed the findings presented in King et al. (2010a), showing the combination of a motion model and echo data ( $v$ ) (i.e. using an indirect correspondence model) to be more robust than the echo image-only estimation ( $iii$ ), which, despite being accurate in the area of coverage of the echo images, is not reliable for a whole heart motion estimation. Furthermore, echo image-only registration was unstable if a suitably close starting estimate was not provided. The improvement gained by the Bayesian method over the indirect correspondence model approach ( $v$ ) (see Section 4.3.2) represents the amount of respiratory variability that the Bayesian estimates are able to capture. Since this variability is highly subject dependent (Keall et al., 2006), so is the level of improvement. Therefore, results were particularly improved for individuals where respiratory motion altered significantly. This adaptability to changes in respiratory motion means that the proposed method has the potential to widen the patient population who could benefit from image guidance. Concerning direct correspondence model estimates,  $\tilde{\theta}(s)$ , inaccuracies affecting the respiratory surrogate measurement in building and applying the model directly affected the estimation accuracy, resulting in higher errors, particularly for the real echo experiments. The performance of the PCA-based motion model was comparable to the image-only estimation, even though no initial estimate was provided to the PCA-based model. The lack of the surrogate information along with artefacts and a low quality of the echo images may be the cause of the poor performance of the PCA-based motion model. Accuracy errors for no motion estimation highlight the need for motion compensation techniques to fulfil clinical requirements (Linte et al., 2010, 2012).

A simple but effective formulation for the automatic determination of the optimal weighting of the likelihood and prior terms was also proposed. The linear relationship between  $\sigma_l^2$  and  $\text{SNR}_d$  simplifies the application of the Bayesian model, which only requires the knowledge of the  $\text{SNR}_d$  of the echo image acquired. The formulation for



the optimal  $\sigma_l^2$  should be valid for any new patient dataset and for this reason a leave-one-out technique to derive the coefficients  $a_1$  and  $a_2$  was employed. However, the typical values of  $a_1$  and  $a_2$  need to be evaluated on a larger set of volunteers/patients to account for variations affecting the echo imaging acquisition. In this study, the  $\text{SNR}_d$  was derived from the echo-only image registration and, given the increasing availability of 3D live-stream echo images and parallelisation algorithms, the  $\text{SNR}_d$  could be rapidly computed and made available for the Bayesian estimation. The proposed method for determining the optimal value of  $\sigma_l^2$  used a segmentation of the LV cavity and myocardium derived from the high resolution MRI image, which were then warped to each live echo image using the MRI to patient rigid registration and the affine echo-only registration. The MRI to patient rigid registration is available from the XMR suite and the associated rigid registration errors are estimated to be approximately 2 mm (Rhode et al., 2005). The affine echo-only image registration was used to warp the LV segmentations to the respiratory position of each live 3D echo image since, as previously shown by King et al. (2010a) and as confirmed by our results, echo-only registrations produce reasonably accurate estimations within the echo FoV (although much less so outside the FoV). For these reasons, the proposed approach has proved to be accurate enough to make an approximate estimate of  $\text{SNR}_d$ . However, alternative methods that rely on echo images only could be employed instead (Noble and Boukerroui, 2006; Pavani et al., 2012).

As already mentioned in Section 4.2.3, the assumption of statistical independence of the affine parameters is a simplification and may not be strictly valid. However, accounting for the unknown dependencies between parameters would require a large amount of data, increasing the complexity of the clinical acquisition protocol and the Bayesian estimation. Therefore, the proposed formulation represents a simplified but effective description of the prior information about subject-specific respiratory motion. The time required to build the prior probability term depends on the affine registration algorithm used. Typically, from the acquisition of the dynamic MRI images, the prior probability term was built in less than 20 minutes. This time lag is shorter than the time required to move the patient from the MRI scanner to the operative X-ray table and to prepare them for the intervention. The Bayesian method was implemented in C++ with an average CPU execution time of 120 seconds on an 8-core i7-2600 processor per echo image. Therefore the technique is not currently real-time. However,

code optimisation was not the focus of this work and would need to be considered for real-time application.

As mentioned in Section 3.4, the lack of accuracy/robustness of state-of-the-art respiratory motion models and the need for a subject-specific dynamic scan hamper the uptake of respiratory motion models into clinical routine. The Bayesian motion estimation proposed in this Chapter addresses the first limitation of current motion models, providing more accurate respiratory motion estimates compared to state-of-the-art techniques (see Section 4.4). Therefore, in terms of clinical applications, the Bayesian model has the potential to improve guidance in many cardiac interventions, such as catheterisation procedures for EP studies, valve implantation, or cardiac stem cell implantation, where the accuracy requirement is very high. Further, the Bayesian motion model could be used to improve the accuracy of IGIs applied to any other organ affected by respiratory motion.

As mentioned in Section 2.2.2, echo imaging is not currently routinely used in cardiac IGIs, but there is an increasing trend toward incorporating echo information in the procedural workflow (Linte et al., 2008; Wein et al., 2009; Parthasarathy et al., 2011; Gao et al., 2012). The proposed method provides a framework for using echo data to estimate respiratory motion, which could be used in combination with a robotic arm (Ma et al., 2010) for automatic acquisition of the live echo images during the procedure. A proof of concept for this framework is presented in the next Chapter, where the accuracy and robustness of the Bayesian estimation is evaluated using 2D echo images, the acquisition of which is guided by the motion model itself.

## Chapter 5

# Motion Model Guidance of Echo Imaging Acquisition

### Contents

---

<b>5.1</b>	<b>Introduction</b>	<b>77</b>
<b>5.2</b>	<b>Method</b>	<b>78</b>
5.2.1	Respiratory Motion Model	79
5.2.2	Model-Driven Image Acquisition	79
5.2.3	Bayesian Motion Estimation	80
<b>5.3</b>	<b>Evaluation</b>	<b>81</b>
5.3.1	Materials	81
5.3.2	Evaluation Approach	83
<b>5.4</b>	<b>Results</b>	<b>85</b>
<b>5.5</b>	<b>Discussion</b>	<b>87</b>

---

### 5.1 Introduction

In Chapter 4, a respiratory motion estimation technique for cardiac IGIs based on a combination of a motion model and 3D echo imaging was presented. The technique uses a Bayesian approach to resolve the uncertainty in the motion estimates made by the motion model using real-time 3D echo imaging.

The main advantage of 3D over 2D echo is the ability to image cardiac volumes and maintain the moving targeted structure(s) in the field of view (FoV). However, 2D

echo is clinically more available, and has better image quality and higher frame rate compared to 3D echo. Therefore, an attractive approach is to use 2D echo imaging but to maintain the visibility of target structures by automatically controlling the echo acquisition. In the Bayesian motion estimation technique presented in Chapter 4, the direct correspondence motion model used as the prior probability offers a possible means of providing motion information for such an approach. This is the focus of this Chapter, which presents a proof of concept of integrating model-driven 2D echo acquisition into cardiac IGIs. This approach has the advantage of providing high-quality consistent images of the targeted cardiac structures which can then also be used for potentially more accurate and robust respiratory motion estimates. The model-driven echo acquisition could be effectively coupled with robotics, given the increasing availability of algorithms to control robotic arms or robotic instruments (Moorthy et al., 2004; Figl et al., 2008; Yuen et al., 2009). For example, a framework to remotely acquire echo images using a robotic arm has recently been proposed in Ma et al. (2010). Similarly, the model-driven acquisition framework could be used to steer the 2D echo beam using a matrix phased array probe.

The method is highly novel, with very little prior related work. As pointed out in Chapter 3, motion models in IGIs have been used for motion correction of guidance information or intra-procedure imaging, but have not previously been proposed for guiding the image acquisition process itself. This method is based on work presented in Peressutti et al. (2013a). Details on the parts of the proposed framework, as well as on the materials used to validate it are provided in the following Sections.

## 5.2 Method

An overview of the proposed workflow is shown in Figure 5.1. Before the procedure, a subject-specific affine motion model is built using dynamic MRI images and a respiratory surrogate signal (see Section 4.2.3). Probability density functions are derived for each affine parameter to model the respiratory motion and its variability. These are used to form the prior probability term for the Bayesian model (see Section 4.2.3). During the procedure, the target structures of the heart which are to be constantly imaged are manually identified once. The surrogate signal is acquired and a motion

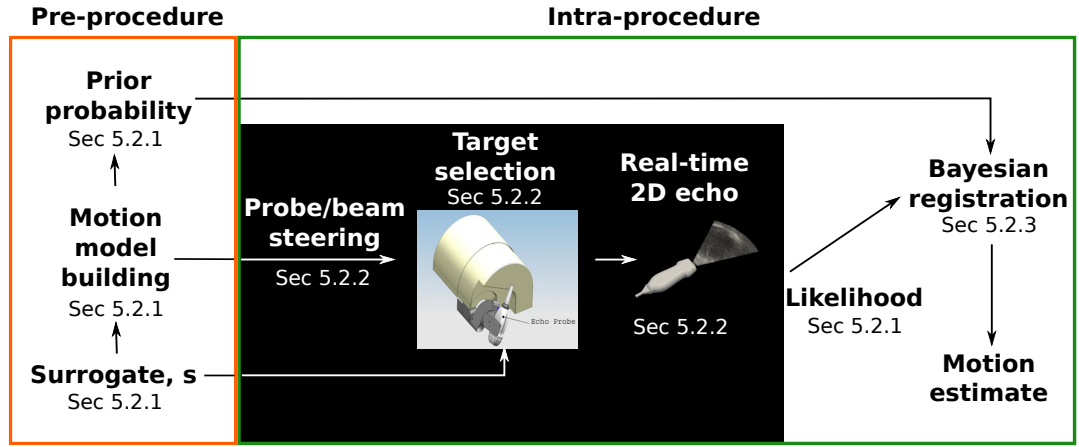


FIGURE 5.1: Schematic overview of the proposed workflow. The black box highlights the novel automatic model-driven 2D echo acquisition proposed in this work.

estimate made using the prior probability term of the motion model only (i.e. without considering the echo imaging). This motion estimate is used to steer the echo probe/beam, providing a 2D imaging plane close to the targeted features. As well as being useful for guidance, the echo images acquired in this way are also potentially more useful for estimating motion using the Bayesian model for updating a cardiac roadmap.

### 5.2.1 Respiratory Motion Model

The respiratory motion model is formed as previously described in Section 4.2.3. A respiratory bellows placed on the volunteer’s chest was employed as the surrogate signal. Note that in this framework the model is used in two different ways. The prior probability function only (i.e. direct correspondence model) is used to derive the respiratory motion estimate which is used to steer the echo probe/beam. The full Bayesian estimation (i.e. incorporating the uncertainty in motion estimation and the 2D echo imaging) is used to compute the final respiratory motion estimate used to update the cardiac roadmap for guidance purposes.

### 5.2.2 Model-Driven Image Acquisition

The main novelty of this work is the automatic model-driven echo image acquisition. The final concept will be to automate the echo acquisition to compensate for respiratory motion. The automatic echo acquisition could be implemented using a robotic arm or by steering the 2D echo beam using a matrix phased array probe.

In Ma et al. (2010), a self-tracked, remotely operated robotic arm with haptic feedback was used to manipulate a 3D trans-thoracic echo (TTE) probe during simultaneous X-ray fluoroscopy and echo acquisitions. The robotic arm was integrated into a X-ray/MRI (XMR) catheterisation suite (Rhode et al., 2005). The XMR suite allows rigid registration of the coordinate systems of the MRI images, the fluoroscopy X-ray images, the robotic arm and the echo images by means of calibration and optical tracking of the patient bed and robotic arm (Rhode et al., 2005; Ma et al., 2010). As a proof of concept, in this Chapter an automatic 2D echo acquisition using the workflow employed in Ma et al. (2010) is simulated. The haptic feedback of the robotic arm ensures that the tip of the probe remains constantly positioned on the chest of the subject and translates only due to the rib cage movement. Consequently, the degrees of freedom of the robotic arm to be controlled by the motion model would be the three rotations only.

The proposed method requires the sonographer to select at least two points  $\mathbf{P}_I = \begin{bmatrix} x_1 & \dots & x_i \\ y_1 & \dots & y_i \\ z_1 & \dots & z_i \end{bmatrix}$ ,  $i \geq 2$  on the desired imaging plane at the reference end-exhale state. Denoting by  $\mathbf{P}_t = \begin{bmatrix} x_t \\ y_t \\ z_t \end{bmatrix}$  the position of the probe tip at end-exhale, the set of points  $\mathbf{P} = [\mathbf{P}_t \ \mathbf{P}_I]$  is used to compute the rotation of the robotic arm to its initial position. Given the intra-procedural value of the surrogate  $s$ , the corresponding points  $\mathbf{Q}_I$  produced by the direct correspondence model estimate are computed as  $\mathbf{Q}_I = \Theta \mathbf{P}_I$ , where  $\mathbf{Q}_I$  and  $\mathbf{P}_I$  are in homogeneous coordinates and  $\Theta$  is the 4x4 affine matrix derived from the direct model estimate  $\tilde{\theta}(s)$ . Denoting by  $\mathbf{Q}_t$  the dynamic position of the probe tip as recorded by the robotic arm, the rotations  $\mathbf{R} = (R_x, R_y, R_z)$  to be input to the controller of the robotic arm are found by minimising the distance between the set of points  $\Psi = \mathbf{P} - \mathbf{P}_t$  and  $\Omega = \mathbf{Q} - \mathbf{Q}_t = [\mathbf{Q}_t \ \mathbf{Q}_I] - \mathbf{Q}_t$ , where  $\Psi$  and  $\Omega$  are centred with respect to  $\mathbf{P}_t$  and  $\mathbf{Q}_t$ , respectively. This ensures that the tip of the probe always lies on the imaging plane. A singular value decomposition (SVD) is used to find the analytical solution to the minimisation problem. The same formulation could be used to steer a 2D echo beam with a matrix phased array probe.

### 5.2.3 Bayesian Motion Estimation

Once the model-driven 2D echo images have been acquired, the full Bayesian technique presented in Chapter 4 is applied during the procedure using the acquired 2D echo images. The echo images are used to compute the likelihood density function, which

resolves the uncertainty expressed in the prior model. As presented in Chapter 4,  $\sigma_l^2$  is derived from the echo images using Equation (4.12) and the Normalised Cross-Correlation similarity measure is employed in the computation of the likelihood. The output of the Bayesian registration is the motion estimate  $\hat{\theta}$  used to update the cardiac roadmap.

### 5.3 Evaluation

The proposed framework is intended to allow automatic guidance of 2D echo image acquisition. In this work, the framework was evaluated using 2D echo images extracted from manually acquired 3D echo images. The use of 3D, rather than 2D echo, enabled the extraction of different imaging planes from the 3D volumes to test different acquisition protocols.

Three related hypotheses were investigated. The first hypothesis was that the Bayesian estimation technique (Peressutti et al., 2013b) is accurate and robust when using 2D echo images rather than 3D. The second hypothesis was that Bayesian estimates using model-driven 2D echo images are more accurate than Bayesian estimates obtained with fixed 2D echo images. The third hypothesis was that the performance of the Bayesian estimation technique would vary depending on the echo imaging plane used (e.g. sagittal or axial).

#### 5.3.1 Materials

##### MRI Acquisition

To investigate these hypotheses, the four volunteer datasets Vol. 13-16 were considered (see Table A.1). For each dataset, a sequence of 3D dynamic MRI images and a 3D high resolution anatomical image were acquired. See Section A.1 for details of the MRI sequences. For each dataset, the dynamic sequence consisted of  $P = 120$  3D images: 40 acquired during normal breathing, 40 during fast breathing and 40 during deep breathing. The dynamic sequence is cardiac gated, and therefore captures cardiac respiratory motion only. The three different breathing patterns were acquired to capture the respiratory motion variability. The next Section describes how the echo images were obtained.

### Echo Images

To evaluate the proposed framework, 3D echo images were manually acquired using an optically tracked probe, as described in Section A.2. Each echo dataset consisted of 2 standard 3D echo images acquired during an end-exhale breath hold over 4 cardiac cycles. An intensity-based rigid registration using a NCC similarity measure was performed to refine the alignment between the 2 standard 3D echo images acquired at end-exhale. The 3D echo images were acquired from a modified parasternal acoustic window, representing a clinically realistic scenario of a robotic arm application (see Figure A.1). The 3D echo images were resampled to a  $2mm$  isotropic voxel size. An example of 3D echo images is shown in Figure 5.2. Inhale 3D echo images were artificially produced from the exhale images and known, gold-standard, MRI-derived motion fields, as detailed in the following Section.

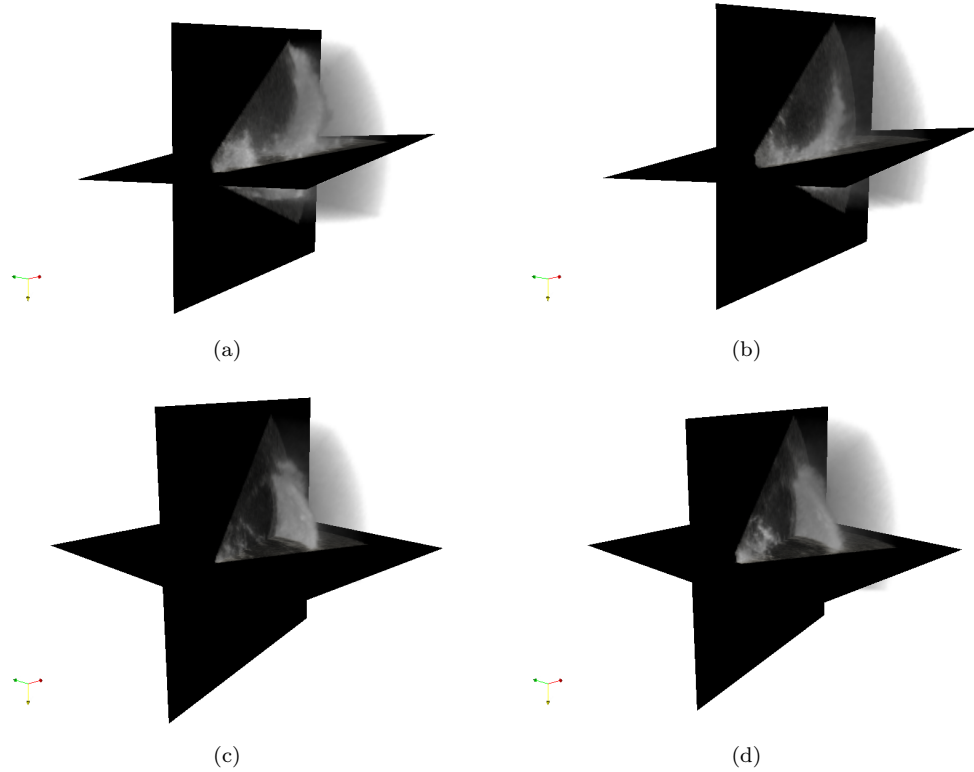


FIGURE 5.2: Example of standard 3D echo images for two datasets. The images are acquired from a modified parasternal acoustic window during two different breath-holds at end-exhale. To ensure spatial alignment of the two echo images, the rigid registration provided by the XMR suite is refined using an intensity-based rigid registration. Echo images for Vol. 13 are shown in Figures (a)-(b), while Figures (c)-(d) show echo images for Vol. 15.



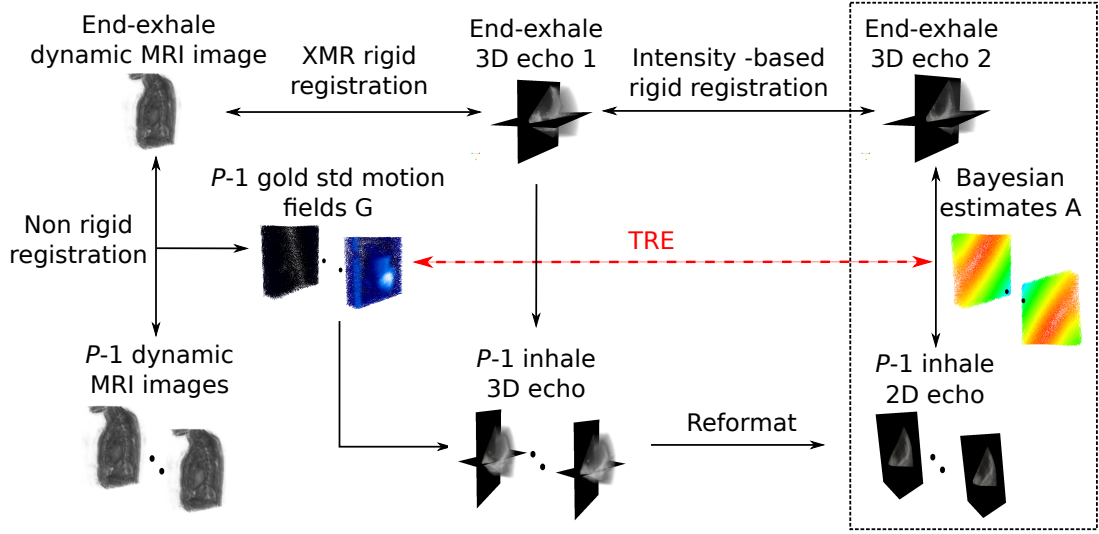


FIGURE 5.3: Block diagram of the evaluation approach employed.

### 5.3.2 Evaluation Approach

As shown in Figure 5.3, to perform a thorough evaluation of the proposed framework, a gold-standard set of motion fields was created. Using a hierarchical non-rigid registration algorithm (Buerger et al., 2011), the  $P - 1$  dynamic MRI images were registered to the dynamic end-exhale reference MRI image, obtaining a set of  $P - 1$  non-rigid gold standard motion fields  $G_p$  and corresponding warped dynamic MRI images. These warped images instead of the original ones were used to build the motion model (see Section 5.2.1). One of the standard 3D echo images (see Figure 5.2(a)) was warped with the non-rigid motion fields  $G_p$ , resulting in a set of  $P - 1$  3D echo images with known, gold standard motion fields. The other standard 3D echo image (see Figure 5.2(b)) was used as reference image for the computation of the likelihood term. The 2D echo images used to test the proposed framework were extracted from the set of  $P - 1$  warped 3D echo images. A leave-one-out cross-validation was used, which means that the motion model employed to estimate  $\tilde{\theta}$  for the  $p$ -th dynamic 2D echo image was built by leaving out the  $p$ -th warped dynamic MRI image. Denoting by  $A_p$  the affine motion fields estimated by the Bayesian registration for the  $p$ -th dynamic 2D echo image, the Target Registration Error (TRE) is the H-component vector with elements

$$TRE_p = \|G_p(\vec{x}_h) - A_p(\vec{x}_h)\|, \quad (5.1)$$

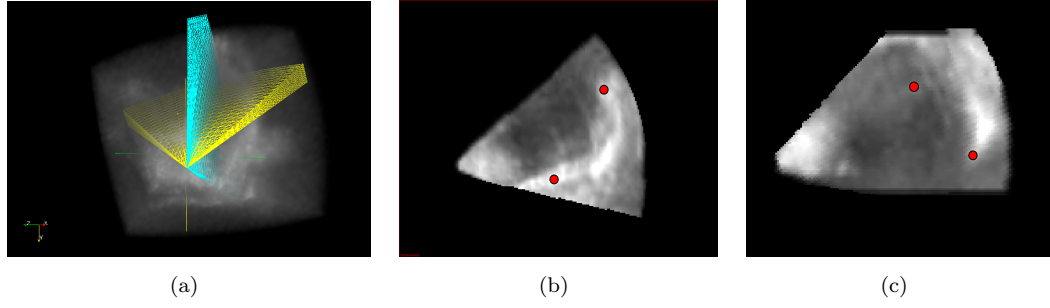


FIGURE 5.4: (a) Rendering of a standard 3D echo image and *sagittal* (cyan) and *axial* (yellow) imaging planes; (b) and (c) example of extracted *sagittal* and *axial* 2D echo image and respective selected points  $P_I$  (red dots).

where  $\vec{x}_h, 1 \leq h \leq H$  are a set of  $H$  landmarks ( $\approx 35,000$ ) of an elliptical mask covering the four chambers of the heart. Median and 95<sup>th</sup> quantile of the sample comprising the  $P - 1$  H-component vectors  $TRE_p$  are reported. To test the first hypothesis, the Bayesian estimation was compared to no motion estimation, direct correspondence model estimation  $\tilde{\theta}$  and image-only estimation (i.e. the likelihood only was maximised).

For all 4 datasets, the same imaging planes were extracted from the  $P - 1$  warped 3D echo images. Since the major components of cardiac respiratory motion approximately lie within the sagittal plane, imaging planes approximately parallel to (*sagittal*) and orthogonal to (*axial*) the sagittal plane were used (see Figure 5.4). Both views were selected in the proximity of the mitral valve on the standard end-exhale 3D echo image. As shown in Figure 5.4(b) and Figure 5.4(c), the points  $P_I$  selected to compute  $R$  were picked on the inter-ventricular septum and the lateral wall of the left ventricle (LV) for the *axial* view and on the inferior and posterior LV wall for the *sagittal* view. These features might be relevant to track in EP studies or valve replacement procedures. For each dataset, the sets of  $P - 1$  2D echo images extracted at the same end-exhale *sagittal* and *axial* views simulated an echo acquisition where the rotation of the probe is fixed, while the sets of  $P - 1$  2D echo images extracted at the model-driven echo probe position (see Section 5.2.2) simulated the proposed framework. Comparison of the accuracy results for fixed and rotating probes allowed the testing of the second hypothesis. Comparing the results for the *sagittal* and *axial* views allowed the testing of the third hypothesis.

## 5.4 Results

Table 5.1 reports median/95<sup>th</sup> quantile of TRE for the techniques compared. The first row of each dataset refers to all  $P - 1$  breathing states while the second row considers the deep breathing states only. Deep breathing results are reported separately since they are likely to contain a large amount of *intra-* and *inter-cycle* variability. TRE of image-only estimation using the fixed 2D echo images is reported only, since similar values were achieved for model-driven echo acquisition. The last two columns report the accuracy improvement achieved by using model-driven against fixed echo acquisition.

Concerning the first hypothesis, by comparing the accuracy results of the Bayesian estimation to the comparative methods it can be noted that Bayesian estimates are the most accurate. The shaded cells in Table 5.1 highlight the estimates having the lowest 95<sup>th</sup> quantile. For each dataset the lowest 95<sup>th</sup> quantile values belong to Bayesian estimates, with improvements in the 95<sup>th</sup> quantile of 50.3%, 56.4%, 56.6% and 29.4% (Vol. 13-16 respectively, all  $P - 1$  states) over the best comparative method, which was the direct correspondence model. These percentages were computed by comparing the best Bayesian estimation result with the best non-Bayesian result, e.g. for Vol. 13 the improvement was  $\frac{15.9-7.9}{15.9}\% = 50.3\%$ . Results of image-only estimation show that 2D to 3D echo registration on its own has very poor robustness.

Concerning the second and third hypotheses, a statistically significant difference (Mann-Whitney U-test,  $p < 0.05$ ) was achieved by rotating the probe. The highest improvements were achieved for the *axial* view, with accuracy improvements of up to 25% for deep breathing. The lower improvement achieved for the *axial* views for Vol. 15 and Vol. 16 might be due to a lower quality of the standard 3D echo images employed, as shown in Figures 5.2(c)-5.2(d). Overall, compared to the *axial* view results, a smaller or no accuracy improvement was achieved by rotating the imaging plane for the *sagittal* view. This is to be expected considering that the selected features in the fixed *sagittal* view were imaged anyway most of the time, requiring minor or no movement of the probe to keep them in the FoV. However, due to the position of the probe tip with respect to the ribs, *sagittal* views are more impractical to acquire compared to *axial* views and more dependent on the subject's anatomy. The accuracy achieved with model-driven *axial* views was comparable to, if not better than, *sagittal* views.

	<i>No estimate</i>	<i>Model only</i>	<i>Image only</i>		<i>Bayesian estimation</i>				<i>Improvement</i>	
			<i>sagittal</i>	<i>axial</i>	<i>sagittal</i>		<i>axial</i>		<i>sagittal</i>	<i>axial</i>
	(mm)	(mm)	<i>fixed</i> (mm)	<i>fixed</i> (mm)	<i>fixed</i> (mm)	<i>rotating</i> (mm)	<i>fixed</i> (mm)	<i>rotating</i> (mm)	(%)	(%)
Vol. 13	2.4/16.1	4.0/15.9	28.9/59.4	8.6/46.1	2.5/8.6	2.2/7.9	2.3/8.6	2.1/8.1	12.0/8.1	8.7/5.8
	8.0/19.2	9.7/18.3	28.8/60.5	16.6/70.0	3.5/11.8	3.0/11.2	3.2/12.9	3.1/12.7	14.3/5.0	3.2/1.6
Vol. 14	5.0/12.4	3.7/10.1	5.8/16.0	12.1/49.7	1.9/4.6	1.9/4.4	2.2/6.9	1.9/5.4	0.0/4.3	13.6/21.7
	7.3/13.0	5.6/10.3	8.0/16.8	15.9/60.8	2.2/5.1	2.1/5.0	3.1/8.0	2.3/6.0	4.5/2.0	25.8/25.0
Vol. 15	5.7/16.4	3.3/11.3	8.1/25.0	9.4/40.0	3.3/6.5	3.3/6.7	1.9/5.4	1.8/4.9	0.0/-3.0	5.3/9.3
	8.4/19.6	4.8/14.1	10.1/32.5	14.9/48.4	3.5/8.0	3.5/8.2	2.3/6.8	2.2/5.9	0.0/-2.5	4.4/13.2
Vol. 16	4.8/15.6	3.8/9.5	6.2/20.8	6.2/19.0	2.3/6.9	2.2/7.2	2.8/7.2	2.5/6.7	4.3/-4.3	10.7/6.9
	6.6/17.4	4.0/10.8	6.3/24.1	7.1/21.4	2.9/7.8	2.9/8.2	3.3/7.8	2.8/7.3	0.0/-5.1	15.2/6.4

TABLE 5.1: Median/95<sup>th</sup> quantile of TRE. The first row of each dataset considers all  $P - 1$  states, while the second row considers the deep breathing states only. For each row, the shaded cells highlight the estimates having lowest 95<sup>th</sup> quantile. The last two columns report the accuracy improvement achieved by using model-driven against fixed echo acquisition. Improvements of median/95<sup>th</sup> quantile are reported.

## 5.5 Discussion

In this Chapter, a novel model-driven 2D echo acquisition framework for robust respiratory motion estimation in cardiac IGIs was proposed. Results showed accuracy improvements of 50.3%, 56.4%, 56.6% and 29.4% over the best comparative estimation technique. The improvements achieved by the model-driven 2D echo acquisition were subject-dependent, but generally higher improvements were achieved for the *axial* views, with improvements up to 25%.

The demonstration of the Bayesian technique presented in Chapter 4 using low-cost standard 2D echo images makes its clinical application more feasible. The technique still requires a reference 3D echo image to compute the likelihood. However, this reference image could be obtained by compounding free-hand 2D echo images or potentially by using the high resolution MRI image as reference image instead.

As previously discussed, direct correspondence model estimates are directly affected by errors in the surrogate acquisition. Consequently, these errors also affect the acquisition of the 2D echo images. However, results show that the use of a model-driven echo acquisition provides an initial respiratory motion compensation that leads to more robust motion estimates. Automatic robotic systems need to be very accurate, robust and have negligible time lag (Yuen et al., 2009) to provide real time adaptation to respiratory motion. The use of a motion model to control the robotic arm will minimise the overall time lag to the time required by the mechanical parts to move. The high acquisition rate of the surrogate  $s$  and the low computational complexity of producing motion model estimates make the model-based image acquisition near real-time. The same conclusions can be drawn for the steering of the 2D echo beam using a matrix phased array probe.

Possible applications of the proposed framework are respiratory motion updating of the cardiac roadmaps used for guidance, or echo image stabilisation, where features of interest are automatically and constantly imaged. A clinical example is stabilisation of the aortic and mitral valve planes in valve replacement interventions.

In the current and previous Chapters, the Bayesian motion model was evaluated using 3D and 2D echo images for respiratory motion estimation in cardiac IGIs. Estimation accuracy results showed the Bayesian model to be more robust and accurate than state-of-the-art motion estimation techniques, thus moving towards the accuracy

requirements needed to translate respiratory motion models into routine clinical practice. However, as with any subject-specific motion model, the Bayesian motion model requires the subject-specific dynamic calibration scan to build the prior probability function. As pointed out in Chapter 3, the dynamic calibration scan often complicates and interrupts the clinical workflow, and in many cases cannot be acquired at all. In the next Chapter, a novel personalisation method for population-based respiratory motion model is proposed. This proposed method provides more accurate respiratory motion estimates without the need for a dynamic calibration scan. The method proposed in Chapter 6 and the Bayesian motion estimation are then combined in Chapter 7 to obtain a personalised Bayesian motion model able to provide accurate and robust respiratory motion estimates without the need for a dynamic calibration scan.

## Chapter 6

# Personalising Population-Based Respiratory Motion Models using Learnt Anatomical Features

### Contents

---

<b>6.1</b>	<b>Introduction</b>	<b>90</b>
<b>6.2</b>	<b>Overview</b>	<b>91</b>
<b>6.3</b>	<b>Materials</b>	<b>92</b>
<b>6.4</b>	<b>Methods</b>	<b>93</b>
6.4.1	Average Shape Atlas	93
6.4.2	Motion Estimates in Atlas Space	94
6.4.3	Quantifying Motion Similarity	95
6.4.4	Neighbourhood Approximation	97
6.4.5	Personalisation	99
<b>6.5</b>	<b>Experiments</b>	<b>100</b>
6.5.1	Evaluation of Estimation Accuracy	101
6.5.2	Evaluation of Correlation Hypothesis	102
<b>6.6</b>	<b>Results</b>	<b>103</b>
6.6.1	Estimation accuracy	103
6.6.2	Correlation hypothesis	104
<b>6.7</b>	<b>Discussion</b>	<b>105</b>

---

## 6.1 Introduction

As already mentioned in Chapter 3, to overcome the need for a subject-specific calibration scan, population-based models have been proposed (Fayad et al., 2010; He et al., 2010; Ehrhardt et al., 2011; Klinder and Lorenz, 2012; Preiswerk et al., 2012; Samei et al., 2012). For such models, the motion in the calibration phase is estimated from calibration scans acquired previously from a sample of the population of subjects, and the model is subsequently applied to a subject not belonging to the sample. Respiratory motion can vary significantly between subjects (Keall et al., 2006), so population-based models are generally less accurate than subject-specific models, as they average out inter-subject variations in motion (McClelland et al., 2013).

Typically, population-based models are personalised to individuals by registering a template image representing the average anatomy of the population sample to a corresponding image of the new subject, and transforming the average motion model from the population coordinate system to that of the new subject. Most population-based models proposed to date use all subjects in the population sample to build the average motion model which is then applied to any out-of-sample subject. In this Chapter, a novel personalisation framework for more accurate population-based respiratory motion model estimates is proposed. A related work was presented in Samei et al. (2012). The authors proposed a technique for making more accurate population-based motion estimates by weighting the contributions of the subjects in the population sample according to similarities of the surrogate. The technique was devised to estimate the respiratory motion and drift of the liver during radiotherapy treatment, but proved effective to estimate the respiratory drift only. As opposed to the personalisation proposed by Samei et al. (2012), the method proposed in this Chapter is applied in the model formation phase instead of the model application phase, and considers static anatomical features only for the personalisation of the motion model, without any information on the respiratory motion or respiratory surrogates of the out-of-sample subject. Hence, to date no work has investigated the use of anatomical features learnt from static images to personalise population-based models in order to achieve more accurate motion estimates.

In our framework, a subset of the population sample that is more likely to represent the respiratory motion of the out-of-sample subject is selected to personalise



the model. The selection is based on anatomical features of the organ derived from a static image which are learnt using a neighbourhood approximation technique. The underlying hypothesis is that the respiratory motion of the organ and its morphology and position are in some way correlated. To the author’s knowledge, this is the first work investigating such a hypothesis. Work has been performed to investigate such a correlation for cardiac cycle motion (Metz et al., 2012), but not, so far, for respiratory motion.

Results on the respiratory motion of the heart are presented. Preliminary work was presented in Peressutti et al. (2013c). This work has been extended and submitted as a journal paper, which forms the basis of this Chapter. While in this Chapter the framework is evaluated using direct correspondence motion models, in the next Chapter the framework is used to derive the prior probability function of the Bayesian motion model presented in Chapter 4.

## 6.2 Overview

An overview of the proposed framework is shown in Figure 6.1. The relationship between the respiratory motion of the heart and its anatomical features is learnt in a prior population model calibration phase. Provided with a static high resolution image of an out-of-sample subject as input, the respiratory motion model is personalised based on its anatomical features.

Each of the  $N$  datasets in the population sample consists of a high resolution image of the heart, a dynamic free-breathing calibration scan capturing the cardiac respiratory motion and some surrogate data (see Section 6.3). Similar to Ehrhardt et al. (2011) and Klinder and Lorenz (2012), an average shape atlas of the anatomy is built using the  $N$  high resolution images (Section 6.3). Respiratory motion estimates are derived from the  $N$  dynamic calibration scans and transformed to the atlas coordinate system to produce a motion atlas (Section 6.4.2). Unlike the population-based models proposed thus far (McClelland et al., 2013; Ehrhardt et al., 2011; Klinder and Lorenz, 2012; Preiswerk et al., 2012) in which an average motion model of the  $N$  datasets is used for any out-of-sample subject, the proposed personalisation selects only  $K \ll N$  subjects from the population sample which are more likely to represent the respiratory motion of the out-of-sample subject. These are selected using a neighbourhood

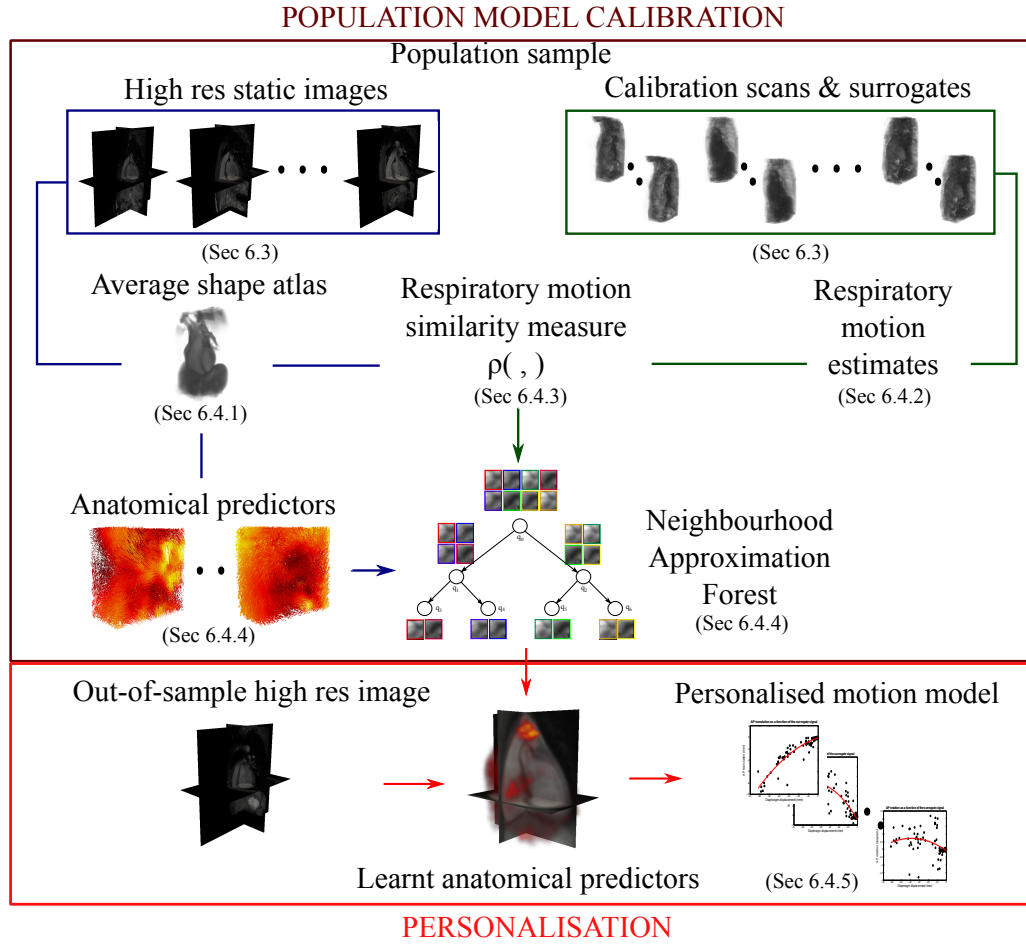


FIGURE 6.1: Overview of the proposed framework for formation of the population-based model and personalisation to out-of-sample subjects.

approximation technique described in Section 6.4.4. The inter-subject variability in motion is therefore exploited to obtain motion estimates that are more accurate than standard population-based model estimates. In the following, each of these stages is described in more detail.

### 6.3 Materials

In this work, 28 healthy adult volunteers were imaged (i.e. all subjects in Table A.1). Each dataset consisted of a static high resolution 3D MRI volume and a free-breathing dynamic 3D MRI calibration scan (see Appendix A for the MRI sequence details).

The high resolution 3D image is part of many routine clinical protocols and provides high spatial resolution information about the anatomy and pathology of the heart. The dynamic calibration scan was ECG-triggered, therefore the images represented the

motion of the heart due to respiration only. The scan acquired  $P = 40$  3D images while the volunteer was breathing normally. Given the short acquisition time of this scan, the FoV of the dynamic images was limited, covering most, but not all, of the four cardiac chambers. The superior-inferior (SI) displacement of the left hemi-diaphragm was measured in each image and this was used as the respiratory surrogate for model formation.

## 6.4 Methods

The constituent parts of the proposed framework can be summarised as:

1. building of an average shape atlas in its natural coordinate system;
2. transformation of respiratory motion estimates from each subject to the atlas coordinate system;
3. analysis of respiratory motion similarities between subjects in the population sample;
4. neighbourhood approximation using respiratory motion similarity as distance metric and anatomical features as predictors;
5. personalisation to out-of-sample subject based on a static image.

The following Sections describe each part in detail.

### 6.4.1 Average Shape Atlas

A typical initial step in the formation of any population-based motion model is the creation of an average shape atlas of the organ investigated, providing a common coordinate system in which the motions of the different subjects can be represented. An average shape atlas of the heart in its *natural coordinate system* (Frangi et al., 2002) was built by iteratively registering and averaging together the high resolution 3D images, as described below.

To remove positional differences from the subsequent non-rigid registrations, the high resolution images were firstly aligned according to the centre of mass of the heart. The centres of mass were computed over a manually positioned binary mask covering the main cardiac chambers and vessels. The same masks were later used for motion estimation and evaluation purposes.

Denoting by  $I_n, n = 1, \dots, N$  the aligned high resolution images, one image was randomly selected as a reference  $I_{ref}$  and the remaining images were registered to it using a hierarchical non-rigid registration algorithm (Buerger et al., 2011). The  $N - 1$  images (i.e. all apart from  $I_{ref}$ ) were warped using the registration results. The intensities of the warped images and  $I_{ref}$  were averaged to obtain an average intensity image  $I_{avg_0}$  which was used as reference  $I_{ref}$  in the next iteration. All  $I_n$  were registered and warped to the new reference  $I_{ref}$  and the intensities of the warped images averaged together to obtain  $I_{avg_1}$ . This non-rigid registration and averaging process was repeated until the Normalised Cross Correlation (NCC) similarity measure between  $I_{avg_t}$  and  $I_{avg_{t-1}}$  was higher than a predefined threshold of 0.99.

Since the pose and size of  $I_{avg_t}$  was still biased towards the initial choice of  $I_{ref}$ , the method proposed in Frangi et al. (2002) and Rueckert et al. (2003) was employed to remove any remaining bias, as follows. The final average image  $I_{avg_t}$  was non-rigidly registered to each  $I_n, n = 1, \dots, N$  and the resulting  $N$  deformation fields were averaged together and used to warp  $I_{avg_t}$ . The result of this warping is the final atlas image  $I_{atlas}$  in its *natural coordinate system*, which requires the least residual deformation to explain the anatomical variability across all individuals. An example of  $I_{atlas}$  formed from the 28 volunteers is shown in Figure 6.2, overlaid with the binary mask used for registration.

### 6.4.2 Motion Estimates in Atlas Space

To compare the respiratory motion of the different subjects in the population sample, the motion was first estimated from each of the dynamic calibration scans. These motion estimates were transformed to the atlas natural coordinate system, where they could be directly compared. This process is described below.

In the following,  $D_{n_p}$  denotes the dynamic calibration image  $p$  of subject  $n$ ,  $p = 1, \dots, P$ ,  $n = 1, \dots, N$ . To estimate the respiratory motion of the heart, the dynamic image with the highest corresponding value of the surrogate was selected as the reference end-exhale image  $D_{n_{ref}}$  and all remaining images were registered to it. As reported in the literature (Shechter et al., 2004; King et al., 2009a), cardiac respiratory motion can be well described by affine deformations, therefore a 12 parameter affine registration algorithm to align  $D_{n_{ref}}$  to all other  $D_{n_p}$  was employed. This resulted in a set of  $P$  affine transformations  $R_{n_p}$  that map  $D_{n_{ref}}$  to  $D_{n_p}$  for each subject  $n$ . To localise the

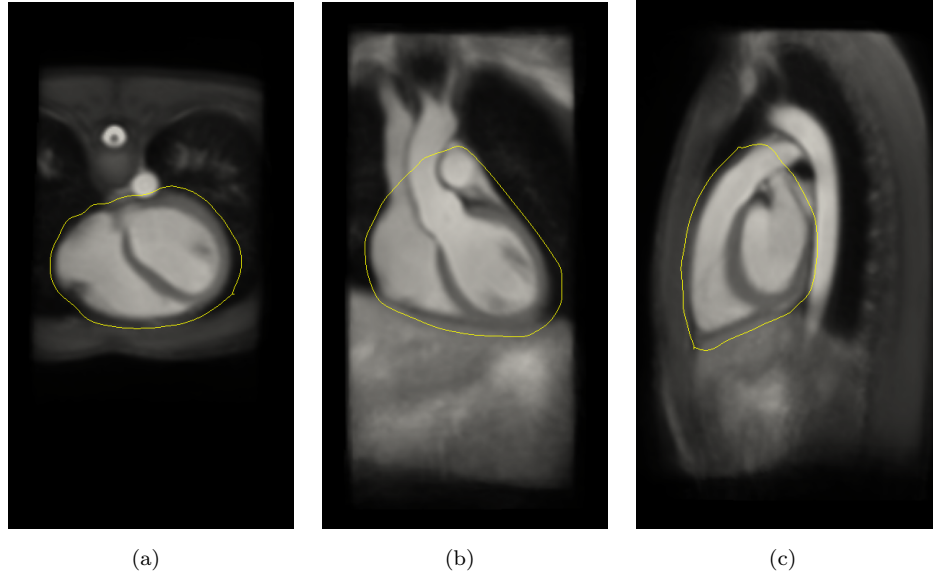


FIGURE 6.2: Axial (a), coronal (b) and sagittal (c) views of the average shape atlas of the heart in its natural coordinate system. Despite the blurring effect of the averaging process, all major cardiac features are well represented and discernible. The outline of the binary mask used to derive the anatomical features (see Section 6.4.4) is overlaid in yellow.

registration to the heart only, the dynamic images were masked using the same binary masks employed to build the atlas.

The transformations<sup>6</sup>  $R_{n_p}$  were transformed to the atlas coordinate system using the method proposed in Rao et al. (2002, 2004). Denoting by  $T_n$  the diffeomorphic non-rigid transformation that maps each high resolution image  $I_n$  to  $I_{atlas}$  and by  $\mathbf{r}_{n_p}$  the respiratory deformation field corresponding to  $R_{n_p}$ , the transformation was computed as follows

$$\mathbf{r}_{n_p}^{atlas} = J_n^{-1} \mathbf{r}_{n_p}, \quad (6.1)$$

where  $J_n^{-1}$  is the inverse of the Jacobian matrix of  $T_n$  and  $\mathbf{r}_{n_p}^{atlas}$  the deformation field transformed to the atlas coordinate system. The Jacobian matrix can be determined analytically and does not require the computation of the inverse transformation  $T_n^{-1}$ .

### 6.4.3 Quantifying Motion Similarity

The previous two steps are typical of many population-based motion models and allow the creation of a common coordinate system where the subject-specific respiratory

<sup>6</sup>For clarity's sake, in the following, a capital letter denotes the transformation mapping one image to another, while a small bold letter denotes the deformation field corresponding to the transformation.

motion estimates can be represented. The end result is a set of  $N \times P$  respiratory deformation fields  $\mathbf{r}_{n_p}^{atlas}$  in the atlas natural coordinate system.

The aim of the next step was to quantify the similarities between the respiratory motions of the different subjects. The motivation for this was to learn the relationship between the anatomical features and respiratory motion. Quantifying motion similarities is a non-trivial task due to the lack of sampling correspondence between subjects, i.e. the surrogate values at which motions are estimated are different.

To overcome the lack of sampling correspondence between subjects, a similarity measure from the pairwise comparison of subject-specific respiratory motion models was derived.  $r_{n_{px}}^{atlas}$ ,  $r_{n_{py}}^{atlas}$  and  $r_{n_{pz}}^{atlas}$  denote the  $x$ ,  $y$  and  $z$  components of the respiratory deformation field  $\mathbf{r}_{n_p}^{atlas}$  corresponding to the respiratory state  $p$  of subject  $n$ . In order to compare the respiratory positions of the different subjects, the respiratory surrogate  $s$  of each subject was normalised so that the minimum and maximum values were  $[-1, 0]$ . The subjects were given no particular breathing instructions during the dynamic scan acquisition, so it is assumed that the acquired sequence is an unbiased sample of their normal breathing pattern. Similar to King et al. (2011), a subject-specific polynomial motion model  $\Phi_n(s)$  was formed for each subject  $n$  by fitting a polynomial function to the  $P$  values of  $r_{n_{px}}^{atlas}$ ,  $r_{n_{py}}^{atlas}$  and  $r_{n_{pz}}^{atlas}$  as a function of the surrogate  $s$  for every control point of a grid covering the whole imaging volume. For details of the order of the polynomial function and the spacing of the grid see Section 6.5. Provided with a value of the surrogate  $s$ , the model produces an estimate of the respiratory deformation field  $\mathbf{r}_{n,s}^{atlas}$ . Although the original motion estimates were affine, due to numerical approximations and registration inaccuracies, the deformation fields  $\mathbf{r}_{n_p}^{atlas}$  are not strictly affine after transforming them using Equation (6.1).

To quantify motion similarities across subjects, the difference in respiratory deformation estimation between each pair of subject-specific motion models was computed as a motion similarity metric. Given 40 values of the surrogate  $s$  linearly distributed in  $[-1, 0]$ , Target Registration Errors (TREs) between each pair of 40 motion model estimates were computed using all  $H \approx 30,000$  voxels in the binary mask covering the heart of the atlas as target points. For any given pair of subjects,  $i$  and  $j$ , the TRE was a vector of length  $40 \times H$ , with the element for voxel  $h$  and surrogate  $s$  defined as

$$TRE_{i,j,s,h} = \|\Phi_i(s)_h - \Phi_j(s)_h\|_2 = \|\mathbf{r}_{i,s,h}^{atlas} - \mathbf{r}_{j,s,h}^{atlas}\|_2, \quad (6.2)$$

where  $\Phi_i(s)_h$  and  $\mathbf{r}_{i,s,h}^{atlas}$  denote the model deformation estimation for subject  $i$  for the given surrogate values  $s$  at the  $h$ -th voxel location. The 95<sup>th</sup> quantiles of these pairwise TREs computed over the 40 values of  $s$  and all voxels  $h = 1, \dots, H$  were employed as the motion similarity metric,  $\rho(i, j) = 95^{th} \text{quantile}\{TRE_{i,j,s,h}\}$ ,  $\forall h, s, i, j = 1, \dots, N$  and a  $N \times N$  distance matrix  $\mathbb{P} = \{\rho(i, j)\}$  was built. The statistical distribution of TREs was highly asymmetric and non-Gaussian, thus quantiles represented a robust statistic of the distribution.

#### 6.4.4 Neighbourhood Approximation

The main novelty of this work is the investigation of the hypothesis that the respiratory motion of the heart is in some way correlated with the cardiac morphology and position. Considering the mechanics of respiration, the contraction/relaxation of the diaphragm and the movement of the rib cage are the driving forces of motion (Sharp et al., 1975). Therefore, it is reasonable to hypothesise that the morphology of the heart and its pose with respect to the rib cage and diaphragm will affect its respiratory motion.

In this work, the Neighbourhood Approximation Forests (NAF) technique recently proposed by Konukoglu et al. (2013) is utilised. The aim of the application of this technique is to determine the neighbourhood of an out-of-sample subject by learning the underlying manifold implied by the respiratory motion similarities.

The training database for this learning phase consisted of the anatomical deformation fields  $\mathbf{t}_{atlas \rightarrow n}$ , corresponding to  $T_n^{-1}$ , that map the atlas  $I_{atlas}$  in its natural coordinate system to each subject  $I_n$ , and the pairwise distance matrix  $\mathbb{P}$ . An example of  $\mathbf{t}_{atlas \rightarrow n}$  is shown in Figure 6.3. In the learning phase, NAF learns the subset of anatomical deformations that are most strongly correlated with the neighbourhood structure implied by the respiratory motion similarities  $\mathbb{P}$ .

An overview of the training phase of the NAF is shown in Figure 6.4. Since the interest is on the morphology of the heart only, the subset of  $H$  anatomical deformations  $\mathbf{t}_{atlas \rightarrow n}^H$  defined over the binary mask covering the heart and major vessels of the atlas were considered as features, instead of the deformations  $\mathbf{t}_{atlas \rightarrow n}$  defined over the entire imaging volume. An outline of the binary mask is shown in Figure 6.2. In order to remove translational offsets from the feature analysis, the mean value of the deformation vectors  $\mathbf{t}_{atlas \rightarrow n}^H$  was subtracted. Since our predictors are 3D vectors, the original NAF technique (Konukoglu et al., 2013) was extended to deal with vector

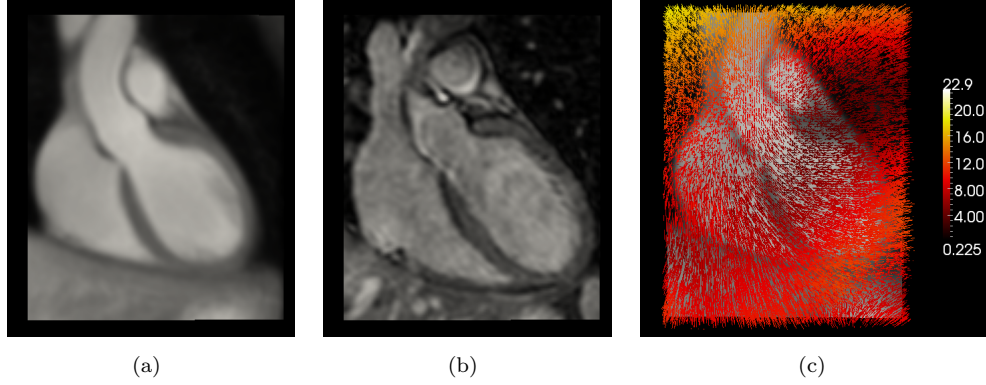


FIGURE 6.3: Coronal views of (a) the atlas  $I_{atlas}$  in its natural coordinate system and (b) one subject  $I_n$  of the population. The deformation field  $\mathbf{t}_{atlas \rightarrow n}$  mapping the anatomical transformation  $T_n^{-1}$  is overlaid onto the atlas and shown in (c). The scale of the colormap is  $mm$ .

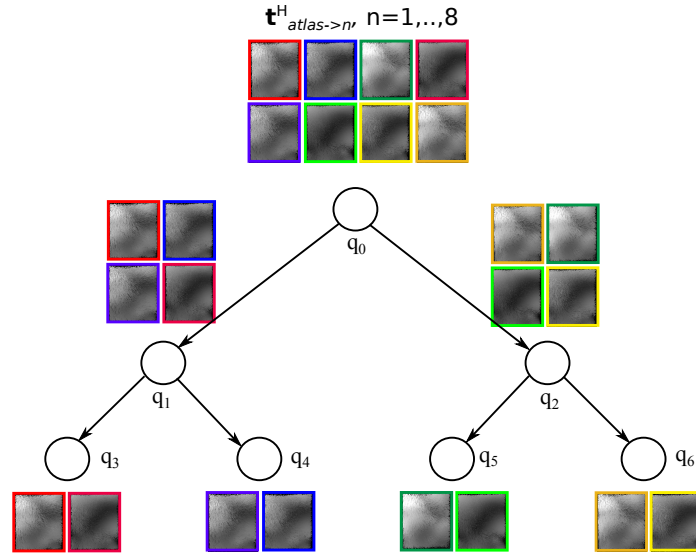


FIGURE 6.4: Toy example of binary tree training of the NAF. The  $N = 8$  anatomical deformation fields  $\mathbf{t}_{atlas \rightarrow n}^H$  are the input vector features. At each node, the training dataset is partitioned into smaller balanced sets. The partitioning optimises over the anatomical vector features able to describe the neighbourhood structure implied by the respiratory motion similarity distances  $\rho(i, j)$ , here represented as similarities in colour of the frame.



predictors rather than scalars. A brief description of the NAF algorithm and the proposed extension to it are provided in Appendix B. The parameters to be optimised were the number of trees in the forest, the minimum number of samples per node and the number of random features selected at each node. These parameters were determined by means of cross-validation and the values are reported in Section 6.5.

#### 6.4.5 Personalisation

The personalisation of the proposed population-based model is carried out before model application. The input is a static high resolution image  $I_{oos}$  of the heart for an out-of-sample subject, while the output is a respiratory motion model personalised for the out-of-sample subject.

The anatomical deformation field  $\mathbf{t}_{atlas \rightarrow oos}$  was determined by registering  $I_{atlas}$  to  $I_{oos}$ . After the subtraction of the mean value, the anatomical deformations  $\mathbf{t}_{atlas \rightarrow oos}^H$  over the binary mask were given as input to the trained NAF. The out-of-sample anatomical deformations were propagated through each node in every tree in the forest by testing the features learnt in the previous step (see Section 6.4.4). The individual tree predictions were combined by computing an affinity measure  $A(I_{oos}, I_n) = \sum \mathbf{1}(I_n), \forall I_n$  for every tree in the forest, where  $\mathbf{1}(\cdot)$  is the indicator function, i.e. it is 1 if  $I_n$  is in the same terminal node as  $I_{oos}$ , and 0 if not. The affinity measure therefore counted the occurrences of  $I_n$  in the same terminal node as  $I_{oos}$  for all trees in the forest. The  $K$  subjects used to build the motion model for the out-of-sample subject were the  $K$  subjects with the highest affinity measure, representing the  $K$  closest neighbours on the manifold implied by the respiratory motion distances  $\rho(\cdot, \cdot)$ .

The respiratory motion estimates of the  $K$  neighbours were transformed to the coordinate system of the out-of-sample subject using Equation (6.1), but employing the forward Jacobian matrix instead of its inverse. A direct correspondence polynomial motion model, similar to those used to determine respiratory motion similarities (see Section 6.4.3), was then built using the transformed respiratory deformations. Given the respiratory surrogate values for the out-of-sample subject, respiratory motion model estimates were produced.

## 6.5 Experiments

The aims of the evaluation were two-fold.

First, the estimation accuracy of the proposed personalised model was investigated by comparing it to other estimation techniques, namely no respiratory motion estimation, a standard average population-based motion model (Fayad et al., 2010; He et al., 2010; Ehrhardt et al., 2011; Klinder and Lorenz, 2012; Preiswerk et al., 2012), and a subject-specific motion model (King et al., 2011). The subject-specific motion model accuracy represented the best target accuracy achievable. Details of this experiment are presented in Section 6.5.1.

Secondly, the relationship between the anatomical features and the respiratory motion of the heart was analysed in the set of experiments detailed in Section 6.5.2.

For all experiments, a leave-one-out cross-validation was employed. Each of the 28 volunteer datasets was left out in turn and the remaining 27 datasets were used as the population sample (i.e.  $N = 27$ ). The left-out dataset was used as the out-of-sample subject  $I_{oos}$ . Similar to the evaluation approach used in Chapter 5, for a thorough accuracy evaluation, the dynamic images  $D_{n_p}$  of each dataset  $n$  were non-rigidly registered (Buerger et al., 2011) to the dynamic end-exhale reference image  $D_{n_{ref}}$ . This process resulted in  $P - 1$  gold-standard non-rigid motion fields which were employed to evaluate the accuracy of all techniques compared in each experiment. By warping  $D_{n_{ref}}$  using the gold-standard non-rigid motion fields, a set of artificial images with known, realistic motion fields was obtained and employed instead of the original images  $D_{n_p}$  to estimate and compare the respiratory motion of the different subjects (see Sections 6.4.2 and 6.4.3).

Target Registration Errors between the non-rigid gold-standard deformations and the respiratory deformations estimated by the compared techniques were computed over the  $H$  voxels in the binary mask covering the major chambers and vessels of the heart for all respiratory positions  $p = 1, \dots, P - 1$ . Median and 95<sup>th</sup> quantile of the  $H \times (P - 1)$  values of the TREs are the statistics considered as accuracy measures. Results for each experiment are reported in Section 6.6. Mean and standard deviation of the  $N$  values for the median and 95<sup>th</sup> quantile are reported for compactness of representation.

### 6.5.1 Evaluation of Estimation Accuracy

The aim of this experiment was to evaluate the estimation accuracy of the proposed personalisation framework compared to state-of-the-art techniques. To this end, the following methods were compared:

- (I) no respiratory motion estimation;
- (II) standard population-based motion model (Fayad et al., 2010; He et al., 2010; Ehrhardt et al., 2011; Klinder and Lorenz, 2012; Preiswerk et al., 2012). All  $N$  subjects were used to build an average motion model which was applied to the out-of-sample subject  $I_{oos}$ . To build such an average population-based model, all respiratory motion deformations  $\mathbf{r}_{n_p}^{atlas}$ ,  $\forall n, \forall p$  were transformed to the coordinate system of  $I_{oos}$  using Equation (6.1). Given the normalised ranges  $[-1, 0]$  of the surrogate values, an average motion model of the  $N \times P$  respiratory deformations at all control points of a grid covering the heart of  $I_{oos}$  was formed as a function of the normalised surrogates;
- (III) the proposed personalised motion model. As in (II), but only the  $K$  closest neighbours as predicted by the NAF were used to form the model for the out-of-sample subject  $I_{oos}$ ;
- (IV) subject-specific motion model (King et al., 2011). The respiratory motion model was formed using the respiratory deformations derived directly from the dynamic calibration scan of the out-of-sample subject. A leave-one-out validation was used to form the subject-specific motion model, meaning that, to estimate the respiratory position  $p$ , the corresponding respiratory deformations were not included in the model formation. The accuracy of the subject-specific model estimates represent a limit to the accuracy achievable by population-based motion models.

For all motion models compared (II, III, IV), a grid spacing of  $5mm$  was employed and a  $2^{nd}$  order polynomial function was fitted to the  $x, y, z$  components of the respiratory deformation fields at all control points of the grid (King et al., 2011). For method (III), the parameters were optimised using a subsample of 15 subjects from the population sample. The optimal NAF parameters for the proposed technique (III) were 500 trees, minimum number of samples  $\Delta = 3$  and  $h = \sqrt{H}$  random features (see Appendix B).

### 6.5.2 Evaluation of Correlation Hypothesis

The aim of this experiment was to provide more insights into the relationship between the anatomical features of the heart and its respiratory motion in healthy adult volunteers. Given the hypothesis that some cardiac anatomical features can be used to predict similarities in respiratory motion of the heart, the proposed personalised model was compared to two different techniques that employed the anatomical similarities only, i.e. without knowledge of respiratory motion similarities, to select the  $K$  subjects used to personalise the respiratory motion model.

The techniques compared were:

- (i) exhaustive search based only on anatomical similarity. Given the anatomical features  $\mathbf{t}_{atlas \rightarrow oos}^H$  of the out-of-sample subject  $I_{oos}$ , the  $K$  subjects of the population sample with the most similar features were used to personalise the respiratory motion model. No training was required for this experiment. The similarity of the features was quantified by computing the mean anatomical deformation difference

$$\rho_{anat}(oos, n) = \frac{1}{H} \sum_{w=1}^H \|\mathbf{t}_{atlas \rightarrow oos}^{H_w} - \mathbf{t}_{atlas \rightarrow n}^{H_w}\|_2, \quad (6.3)$$

where  $H_w$  denotes the  $w$ -th voxel of the  $H$  voxels in the binary mask. The more similar the anatomies of  $I_{oos}$  and  $I_n$  were, the lower the value of  $\rho_{anat}(oos, n)$ ;

- (ii) NAF using anatomical similarity. The proposed framework (III) was used, but rather than using the respiratory motion distance  $\rho(\cdot, \cdot)$  defined in Section 6.4.3, the mean anatomical deformation difference  $\rho_{anat}(\cdot, \cdot)$  defined in Equation (6.3) was used instead. This technique corresponds to unsupervised clustering with respect to the entire set of anatomical features. The best anatomical features selected by the NAF would therefore correlate with the neighbourhood structure implied by the anatomical similarities rather than the respiratory motion similarities;

- (iii) the proposed model.

Both techniques (i) and (ii) considered anatomical similarities only. In particular, technique (i) used all features for the selection of the  $K$  closest neighbours, while in technique (ii) the subset of features that maximised the anatomical similarity between

the selected  $K$  neighbours was selected. By comparing techniques (i) and (iii) the investigation focused on whether or not the similarity of the whole anatomy would be a good predictor of the respiratory motion, while by comparing techniques (ii) and (iii) the difference between the subset of features most strongly correlated with the anatomical similarity and those most strongly correlated with the similarity in respiratory motion was investigated. The same optimal NAF parameters used in the experiments detailed in Section 6.5.1 were used for techniques (ii) and (iii).

## 6.6 Results

Results of the experiments on the accuracy are reported in Section 6.6.1, while Section 6.6.2 presents results for the experiments on the correlation hypothesis.

### 6.6.1 Estimation accuracy

Results of the leave-one-out cross-validation for the estimation accuracy experiments are reported in Table 6.1. Mean and standard deviation of the  $N$  values for the median and 95<sup>th</sup> quantile of the TREs corresponding to the estimation accuracy experiments are shown. 95<sup>th</sup> quantiles of the TREs for each subject  $n$  are shown in Figure 6.5. Results for no motion estimation ( $I$ ) are not reported in Figure 6.5 for clarity of representation.

Different values for the number of neighbours  $K$  (i.e.  $K = 3, 5, 7$ ) used for the personalisation of the proposed model ( $III$ ) were considered, with no significant statistical difference between the accuracy results over all subjects. However, the value of  $K$  did affect the individual estimation accuracies. For instance, a small  $K$  generated more accurate motion estimations for the subjects showing respiratory motion significantly different from the average motion of the population sample, while poorer accuracy was achieved for subjects with an average respiratory motion. On the other hand,  $K \rightarrow N$  generated better estimation accuracies for subjects showing an average respiratory motion, but poorer accuracy for the other subjects. Therefore, to better highlight the performance of our method, hereafter the results using the closest  $K = 3$  neighbours are reported. The proposed personalised model estimates ( $III$ ) achieved an average improvement in estimation accuracy of 20% for both median and 95<sup>th</sup> quantile compared to an average population-based motion model ( $II$ ). A paired t-test showed a

statistically significant difference with  $p < 0.01$ . The highest improvements of the 95<sup>th</sup> quantile were achieved for subjects 27 (59.2%), 18 (52.8%) and 9 (48.8%). The accuracy improvement was higher for subjects with a respiratory motion differing significantly from the average motion of the population sample. The poor accuracy results achieved for subjects 28 (-40.8%), 15 (-21.0%) and 22 (-11.7%) might be due to sub-optimal parameters of the NAF and the number of neighbours  $K$ . In fact, these subjects show an average respiratory motion and accuracy results can be improved by increasing  $K$ . Furthermore, increasing the number of subjects in the population sample would likely lead to more robust performance improvements.

	Mean/standard deviation (mm)				Impr. in mean (%) wrt (II)
	(I)	(II)	(III)	(IV)	
Median	3.5/2.0	2.0/1.1	1.6/0.6	0.9/0.3	20.0
95 <sup>th</sup> quantile	11.3/4.4	5.9/2.4	4.7/1.5	2.5/0.8	20.3

TABLE 6.1: Leave-one-out estimation accuracy results. Mean and standard deviation of the median and 95<sup>th</sup> quantile of TREs over the  $N$  subjects are reported. The last column shows the accuracy improvement in the mean value achieved by the proposed technique (III) against the average population-based model (II).

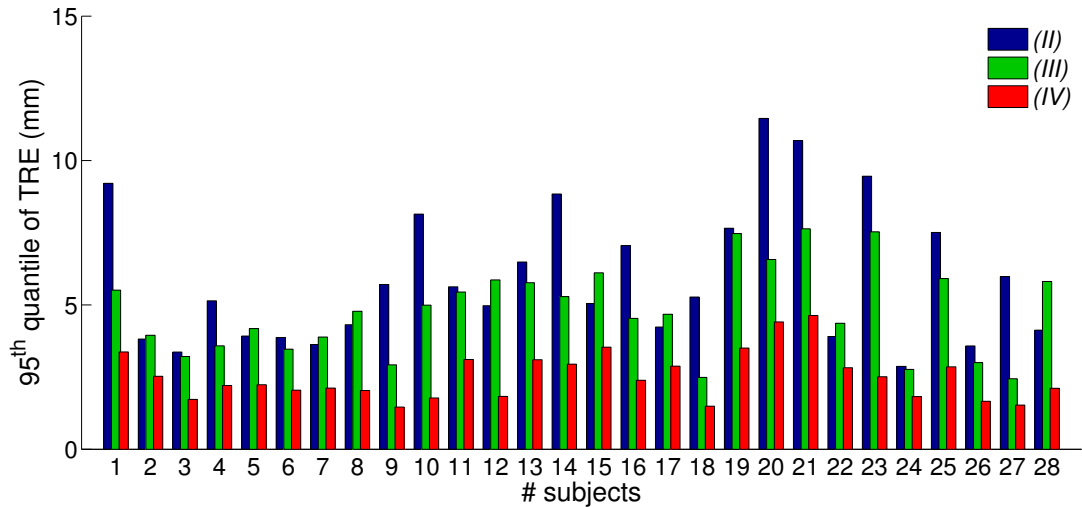


FIGURE 6.5: 95<sup>th</sup> quantiles of the TREs for each left-out subject for the estimation accuracy experiment. Results for the average population-based motion model (II), our proposed personalised motion model (III) and subject-specific motion model (IV) are shown.

### 6.6.2 Correlation hypothesis

Results of the leave-one-out cross-validation for the experiment on the correlation hypothesis are reported in Table 6.2 and Figure 6.6.

The closest  $K = 3$  neighbours were considered for the personalisation of the motion models for all techniques (i), (ii) and (iii). Accuracy results in respiratory motion estimation achieved by techniques (i) and (ii) highlight the fact that the similarity in the anatomy of the heart as a whole is not a good predictor of respiratory motion. In fact, estimation accuracy for both techniques (i) and (ii) was slightly worse than an average population-based model (II).

Figure 6.7 shows the frequency maps of the anatomical features that were selected as best features by the NAF for methods (ii) and (iii). For clarity of representation, the frequency maps shown are scaled to the maximum value, which was different for method (ii) and (iii) (see colourmap ranges). It can clearly be seen that the most relevant features implied by the anatomical similarities are different from those implied by the similarity in respiratory motion. In particular, referring to Figure 6.7(b), anatomical features most strongly correlated to respiratory motion are found on the apex of the heart in proximity to the diaphragm and the rib cage, on the left ventricle and interventricular septum. This seems plausible, considering that the main drivers of respiratory motion are the diaphragm and the rib cage movement. On the contrary, the set of features most strongly correlated to anatomical similarity only (Figure 6.7(a)) are less localised, especially in the inner regions of the heart. This experiment emphasises the importance of the respiratory motion manifold in constraining the selection of the anatomical features relevant for respiratory motion estimation.

	Mean/standard deviation (mm)			Impr. in mean (%)
	(i)	(ii)	(iii)	
Median	2.1/1.1	2.1/1.0	1.6/0.6	23.8
95 <sup>th</sup> quantile	6.6/2.8	6.4/2.6	4.7/1.5	26.6

TABLE 6.2: Leave-one-out results for the correlation hypothesis experiment. Mean and standard deviation of the median and 95<sup>th</sup> quantile of TREs over the  $N$  subjects are reported. The last column shows the accuracy improvement in the mean value achieved by technique (iii) with respect to (ii).

## 6.7 Discussion

In this Chapter, a novel framework for the personalisation of population-based respiratory motion models was proposed. The proposed method selects a subset of the population sample which is more likely to represent the respiratory motion of an out-of-sample subject based on learnt anatomical features only. These learnt anatomical

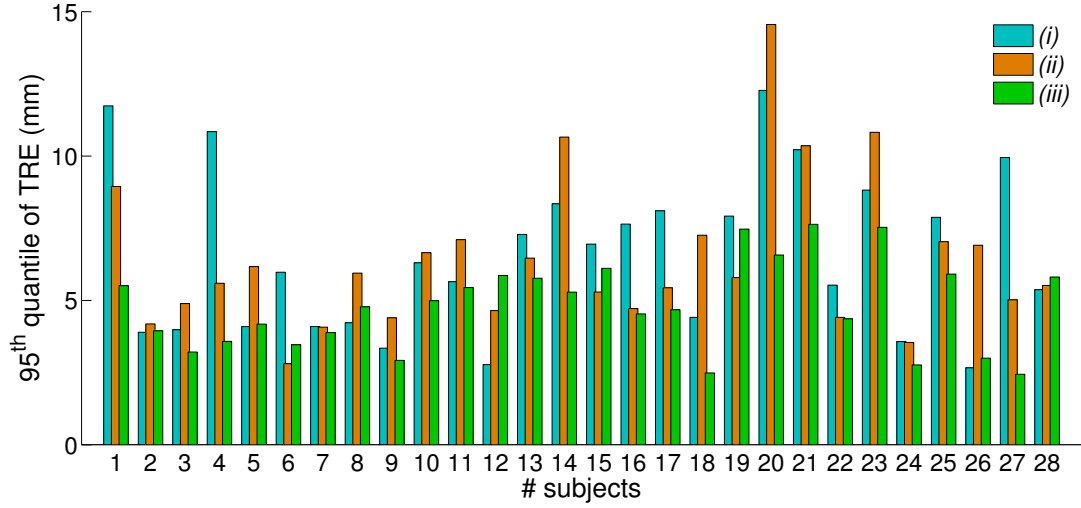


FIGURE 6.6: 95<sup>th</sup> quantiles of the TREs for each left-out subject for the correlation hypothesis experiment. Results for the exhaustive search based on anatomical similarities (i), NAF on anatomical similarities (ii) and the proposed model (iii) are shown.

features are able to predict the neighbourhood structure implied by the similarity in respiratory motion.

Results on the cardiac respiratory motion of adult healthy volunteers derived from MRI images were reported. The proposed framework showed average improvements in respiratory motion estimation accuracy of 20% compared to state-of-the-art population-based motion models. Results reported in this paper support the hypothesis of correlation between the anatomical appearance of the heart and its motion due to respiration. To the author’s knowledge, this is the first work investigating such a hypothesis. In particular, features of the heart on the apex in proximity to the diaphragm and rib cage, on the left ventricle and on the interventricular septum were found to be good predictors of the similarity in respiratory motion of the heart. The anatomical features selected by the NAF could be used to derive local high-order descriptors of the cardiac shape which might be meaningful from a clinical perspective. For instance, in future work, the average shape of the apex for the different subsets in the population sample could be extracted and used as a clinical parameter for motion classification.

There is a conceptual link between the framework described here and prior work on multi-atlases. For example, in Aljabar et al. (2009) and Wolz et al. (2010) more accurate atlas-based segmentations were achieved by exploiting similarities between



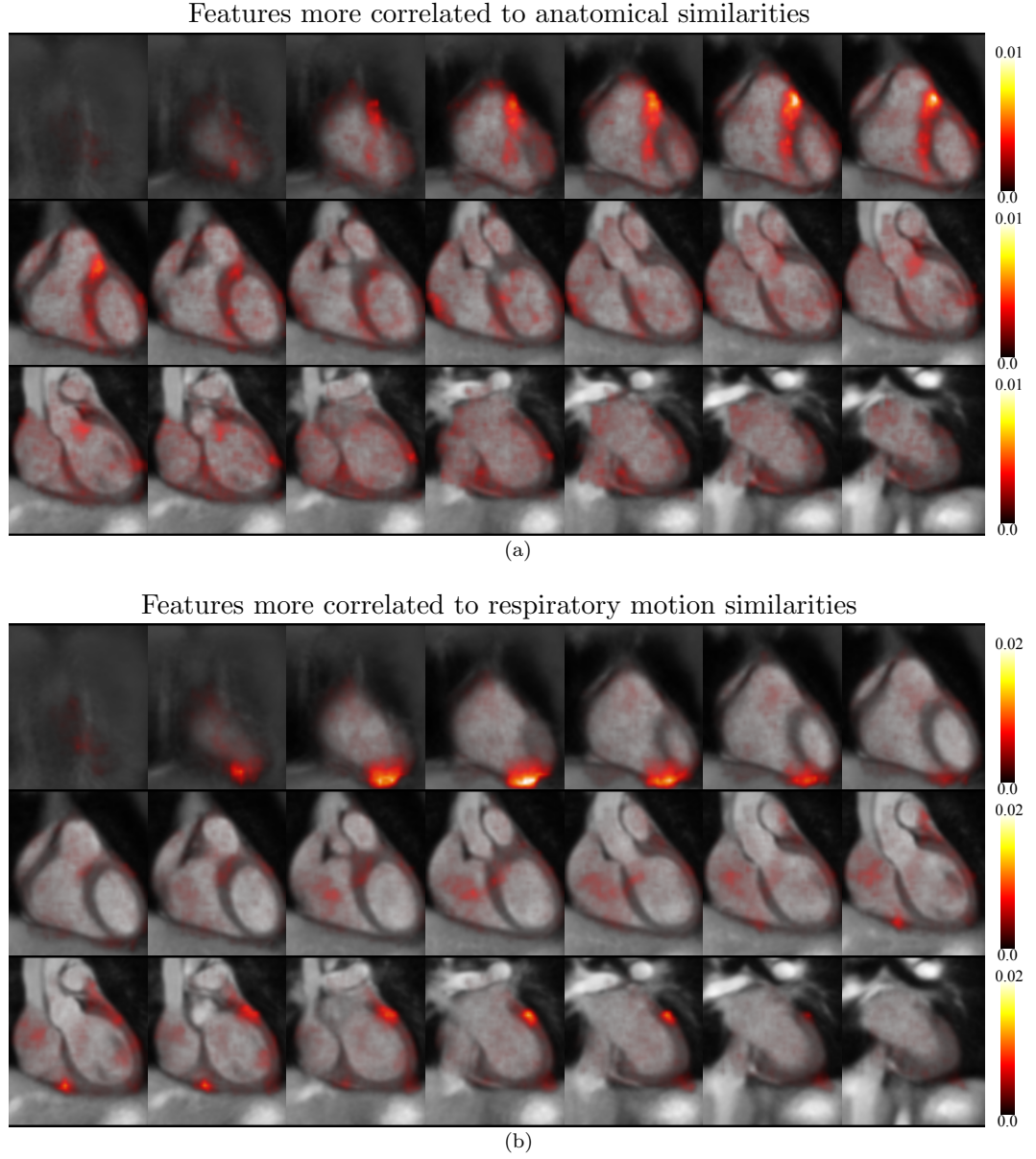


FIGURE 6.7: Frequency maps. The frequency of the best features  $m_q$  selected during the training of the trees in the forest normalised by the overall number of nodes is overlaid onto the atlas. Coronal views in the antero-posterior direction show (a) features more correlated to similarities in anatomy (method (ii)), and (b) features more correlated to similarities in respiratory motion (method (iii)). Note the scaling difference of the two colour maps.

an out-of-sample subject and a subset of a database of atlas images. This type of approach can be viewed as defining a manifold of atlas images and then determining the neighbours of a new image in this manifold. Atlas segmentations were then propagated from the neighbours. In the proposed framework, an implicit manifold of motion is defined and NAF is used to find the neighbours of an out-of-sample subject in the manifold. Motion models are then formed from the motion estimates of the neighbours.

To quantify the respiratory motion similarities, the range of the respiratory surrogate was normalised and a motion model was built subsequently for each subject. Therefore, to apply the personalised motion model, the respiratory surrogate signal of the out-of-sample subject needs to be normalised as well. This might require a preparatory phase where the surrogate is acquired to establish minimum and maximum values, so that the surrogate can be normalised in real time. More sophisticated techniques for the quantification of motion similarities might be the focus of future work, as well as the extension to other respiratory patterns, such as shallow or deep breathing.

Further work is also required to investigate the optimal settings for the NAF parameters and the number of neighbours on a larger sample of subjects. It is possible that the relatively poor performance of the proposed method for some subjects is due to non-optimal NAF parameters. A neighbourhood approximation technique was employed in this work, but other methods could be used to provide an explicit formulation of the manifold implied by the respiratory motion. Moreover, further investigations are required to analyse the effect of pathologies and abnormalities of the heart on the cardiac respiratory motion. More robust techniques to derive the anatomical features or the use of non image-based descriptors might be required in these cases.

The application of the proposed framework to other organs affected by respiratory motion, such as the lungs or the liver, could lead to a personalisation framework for the respiratory motion of the whole thorax, provided with the subject-specific anatomy only. Furthermore, previous studies have shown differences in respiratory motion of the lungs due to lung diseases and tumours (Ehrhardt et al., 2009). It is therefore possible that an explicit formulation of the manifold implied by respiratory motion could be used as a diagnostic tool for disease detection or staging. Such an approach could have application in treatment/detection of lung cancer or diseases such as chronic obstructive pulmonary disease.

As pointed out in Chapter 3, the need for a subject-specific calibration scan and the relatively poor estimation accuracy of state-of-the-art population-based motion models represent significant impediments to the clinical translation of respiratory motion models. The proposed framework addresses these limitations, providing more accurate motion estimation without the need for a subject-specific calibration scan, thus opening up new possibilities for the use of respiratory motion models in routine clinical protocols. As discussed in Section 2.2, for some cardiac image-guided interventions, such as ablation procedures or coronary artery bypass grafting, an accuracy of  $\sim 5mm$  represents a clinically adequate goal (Linte et al., 2010), which is on average achieved by the proposed framework. Other procedures, such as the mapping of ablated points or stem cell implantation therapy in the heart (Cleary and Peters, 2010), have higher accuracy requirements, which, currently, no state-of-the-art population-based motion model could achieve. The proposed framework showed results closer to subject-specific models for some subjects, making it a promising solution for such procedures. A static high resolution image of the organ is often already available in the patient’s record so, ideally, the personalisation framework can be applied without the need for any extra imaging, reducing scanning time and cost, and patient discomfort.

In the next Chapter, the personalisation framework presented in this Chapter is used to build the prior probability function of the Bayesian motion model presented in Chapter 4 for an out-of-sample subject. Given the intra-procedure echo images and surrogate values, the population-based Bayesian model estimate is obtained. This way, the accuracy and robustness of the Bayesian motion model is combined with the advantages of the proposed personalisation method to derive accurate and robust respiratory motion estimates with no need for a subject-specific dynamic calibration scan.

## Chapter 7

# Personalised Bayesian Respiratory Motion Model

### Contents

---

<b>7.1</b>	<b>Introduction</b>	<b>110</b>
<b>7.2</b>	<b>Method</b>	<b>111</b>
7.2.1	Personalisation	112
7.2.2	Bayesian Motion Estimation	113
<b>7.3</b>	<b>Evaluation</b>	<b>114</b>
7.3.1	Materials	114
7.3.2	Experiments	115
<b>7.4</b>	<b>Results</b>	<b>117</b>
<b>7.5</b>	<b>Discussion</b>	<b>119</b>

---

### 7.1 Introduction

As mentioned in the previous Chapters, the clinical translation of respiratory motion modelling techniques is currently hindered by their lack of accuracy/robustness, and by the need for a subject-specific calibration scan that complicates the clinical workflow.

The Bayesian motion estimation technique presented in Chapters 4 and 5 addresses the lack of accuracy/robustness by combining the robustness of a respiratory motion model with the real-time information provided by 2D/3D echo images. Results showed the Bayesian estimation to be more accurate and robust than state-of-the-art

motion estimation techniques. Furthermore, the personalisation framework presented in Chapter 6 allows exploitation of inter-subject variability in respiratory motion, enabling accurate motion estimates without the need for a subject-specific calibration scan.

This Chapter presents a proof of principle of the combination of the Bayesian motion estimation approach and the personalisation framework, resulting in a personalised Bayesian respiratory motion model. Specifically, the personalisation framework presented in Chapter 6 is used to build the prior probability function, whilst live 3D echo images are subsequently used to form the likelihood and obtain the final Bayesian respiratory motion estimate. Therefore, the advantages of the two techniques are combined and exploited to overcome the limitations of current respiratory motion modelling techniques. The resulting technique is highly novel, being the first population-based indirect correspondence model ever proposed (see Section 3.3). Furthermore, the technique is able to model both intra- and inter-cycle variability in respiratory motion. This should enable accurate and robust respiratory motion estimates that do not interrupt or further complicate the clinical workflow. The method and the evaluation approach are detailed in Section 7.2 and 7.3, respectively, while results are presented in Section 7.4. A discussion on the technique and the findings is provided in Section 7.5.

## 7.2 Method

An overview of the proposed personalised Bayesian motion estimation approach is shown in Figure 7.1.

The input of the proposed method is a high resolution 3D MRI image of the heart (see Appendix A) of the subject. This image is a standard acquisition in many clinical protocols, providing detailed information about the anatomy and pathology of the heart. Given this 3D image as input, the personalisation framework presented in Chapter 6 selects a subset of  $K$  datasets from the population sample that approximate the neighbourhood implied by the similarity in cardiac respiratory motion. The respiratory motion estimates derived from the previously acquired dynamic calibration scans of the  $K$  datasets are used to build the prior probability function  $p(\theta|s)$  of the Bayesian motion estimation (see Section 4.2.3). Provided with the intra-procedure value of the surrogate  $s$  and the live 3D echo images  $I$ , the likelihood probability function  $p(I|\theta, s)$

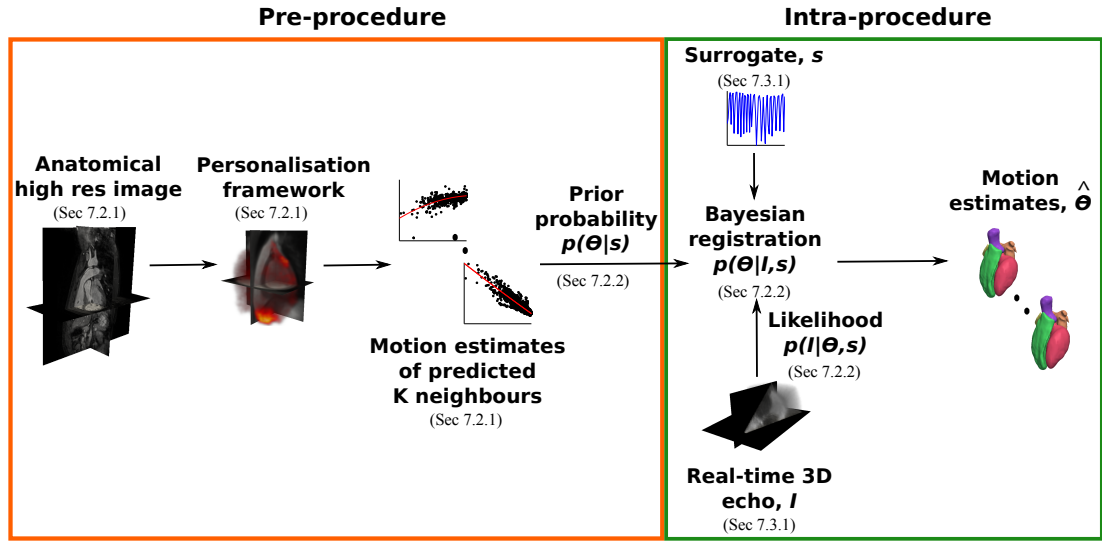


FIGURE 7.1: Overview of the personalised Bayesian respiratory motion model.

is computed and the Bayesian motion estimates  $\hat{\theta}$  are obtained by maximising the posterior probability function  $p(\theta|I, s)$  (see Section 4.2.2). The following Sections describe in more detail how the methods proposed in Chapters 4 and 6 are combined to derive the proposed personalised Bayesian motion model.

### 7.2.1 Personalisation

As detailed in Section 6.4.5, the high resolution 3D MRI image of the out-of-sample subject is non-rigidly registered to the anatomical atlas of the heart in its natural coordinate system. The anatomical non-rigid deformation of the heart resulting from the registration is provided as input to the trained Neighbourhood Approximation Forest (NAF). An affinity measure that approximates the neighbourhood structure implied by the respiratory motion is derived from the predictions of each tree in the NAF. The motion estimates of the  $K$  datasets of the population sample having the highest affinity measure are subsequently used to build the prior probability function  $p(\theta|s)$ , as described below.

In order to apply the personalised motion model in an intervention, it is necessary to transform the model from the atlas coordinate system to the physical space of the catheter laboratory. Normally, the rigid transformation that maps the high resolution MRI image to the intra-procedure physical space is provided by the XMR suite (see Section 2.2.2). Alternatively, the image-to-physical transformation can be derived from the registration of the MRI image and the intra-procedure echo imaging data (King

et al., 2010b; Housden et al., 2013). Once the image-to-physical transformation is determined, the  $P$  motion estimates of each of the  $K$  chosen datasets are warped (Equation (6.1)) to the intra-procedure physical coordinate system, where the echo images are acquired.

Since the Bayesian motion estimation models affine deformations, Singular Value Decomposition (SVD) is employed to linearise the non-rigid motion estimates warped to the intra-procedure physical space. This linearisation process is carried out considering the locations of the  $H$  voxels of an elliptical binary mask covering the main chambers and vessels of the heart. The same mask and voxel locations are used for evaluation purposes (see Section 7.3). The end result of the warping and linearisation processes is a set of  $P \times K$  affine respiratory motion estimates in the intra-procedure coordinate system of the out-of-sample subject (where  $P$  is the number of dynamic calibration images per subject and  $K$  is the number of chosen subjects).

### 7.2.2 Bayesian Motion Estimation

The Supero-Inferior (SI) displacement of the left hemi-diaphragm is employed as the surrogate signal because the same surrogate was used for the quantification of respiratory motion similarity in the personalisation framework. As described in Section 6.4.3, to allow comparison between different subjects, the surrogate range of each subject in the population sample was normalised with respect to its minimum and maximum values. Therefore, the same surrogate should be acquired and normalised intra-operatively for the out-of-sample subject and used to compute the Bayesian motion estimate. There are several ways in which this could be done. For instance, the SI displacement of the left hemi-diaphragm could be acquired intra-operatively using fluoroscopy images (King et al., 2009a) and the range could be normalised with respect to the minimum and maximum values determined during a preparatory phase. Furthermore, as pointed out in Section 4.2.2, the Bayesian motion estimate could in principle be obtained without providing any surrogate value, since this is also optimised during the maximisation of the posterior probability. However, as described in the following Section, in the proof of principle presented in this Chapter the normalised surrogate is derived from the available dynamic calibration scan of the out-of-sample subject and provided as input to the Bayesian motion estimation.

Given the  $P \times K$  linearised affine motion estimates in the intra-procedure coordinate system and the corresponding  $P \times K$  normalised surrogate values, the prior probability function is built as described in Section 4.2.3. During the procedure, provided with the normalised surrogate value  $s$ , a standard 3D echo image  $I_{ref}$  and live 3D echo images  $I$ , the likelihood and posterior probability function are computed (see Section 4.2.4). The optimal value of the variance of the likelihood  $\sigma_l^2$  is derived from the live 3D echo images (see Section 4.2.5). Using the same optimisation algorithm described in Section 4.2.2, the final affine motion estimate  $\hat{\theta}$  is derived by maximising the posterior probability function. In the following Section 7.3, the evaluation approach employed is described.

### 7.3 Evaluation

For a thorough evaluation of estimation accuracy, a similar approach to those employed in Chapters 5 and 6 was used. Given the availability of real 3D echo, the four datasets Vol. 13-16 were considered (see Appendix A). As in Chapter 6, in order to personalise the prior probability density functions, a leave-one-out cross-validation was used to build the personalisation framework. Similar to the evaluation approach used in Chapter 5, for each dataset Vol. 13-16, the dynamic calibration scan was used to derive a set of non-rigid gold-standard motion fields  $G$  which was employed to generate the live 3D echo images  $I$ . The gold-standard motion fields  $G$  were also used to evaluate the accuracy of the Bayesian motion estimates. The materials are reported in Section 7.3.1, while the evaluation approach is described in Section 7.3.2.

#### 7.3.1 Materials

The proof of principle presented in this Chapter combines the personalisation framework presented in Chapter 6 with the Bayesian motion estimation proposed in Chapter 4. Therefore, the same materials employed to evaluate each method separately were employed to evaluate the method here presented. In particular, the 28 healthy volunteer MRI datasets composed of the high resolution images and the dynamic calibration scans were used to build the personalisation framework using a leave-one-out cross-validation. For details of the MRI sequences, please refer to Section A.1. As in



Chapter 6, only the  $P = 40$  dynamic images acquired during normal breathing were considered.

Each echo dataset consisted of 2 standard 3D echo images acquired from a modified parasternal acoustic window during an end-exhale breath hold over 4 beating cycles (see Section A.2 for more details). An intensity-based rigid registration using a NCC similarity measure was performed to refine the alignment between the 2 standard 3D echo images acquired at end-exhale. The 3D echo images were resampled to a  $2mm$  isotropic voxel size. The next Section describes the evaluation approach used to obtain the live 3D echo images and to compute the Target Registration Error (TRE) estimation accuracy.

### 7.3.2 Experiments

As previously mentioned, a leave-one-out cross-validation was used. This means that the personalisation framework utilised to form the prior probability density function for Vol. 13-16 was built by leaving out the dataset being evaluated. The left-out high resolution MRI image was used to derive the closest  $K$  neighbours and subsequently form the prior probability function. As in Chapter 6, the three closest neighbours  $K = 3$  were considered. The same NAF parameters employed in Section 6.5.1 were utilised here.

As shown in Figure 7.2, the left-out MRI dynamic calibration scan was used to generate a set of gold-standard motion fields  $G$ . Following the same approach used in Section 5.3.2, the set of gold-standard motion fields was used to create the set of live 3D echo images and compute TREs. While in Chapter 5 2D echo images were extracted from the set of warped 3D echo images, in this Chapter a FoV similar to that acquired by the iE33 3D real-time echo system was employed to generate the live 3D echo images  $I$  (see Section 4.3.4 for details of the echo beam geometry).

Three different Bayesian motion estimation techniques were compared. The difference between them lies in the formation of the prior probability density function, as follows:

- (A) - *Population-based prior*: the prior probability density function was formed using the respiratory motion estimates of the population sample ( $N = 27$ ) warped to the intra-procedure coordinate system.

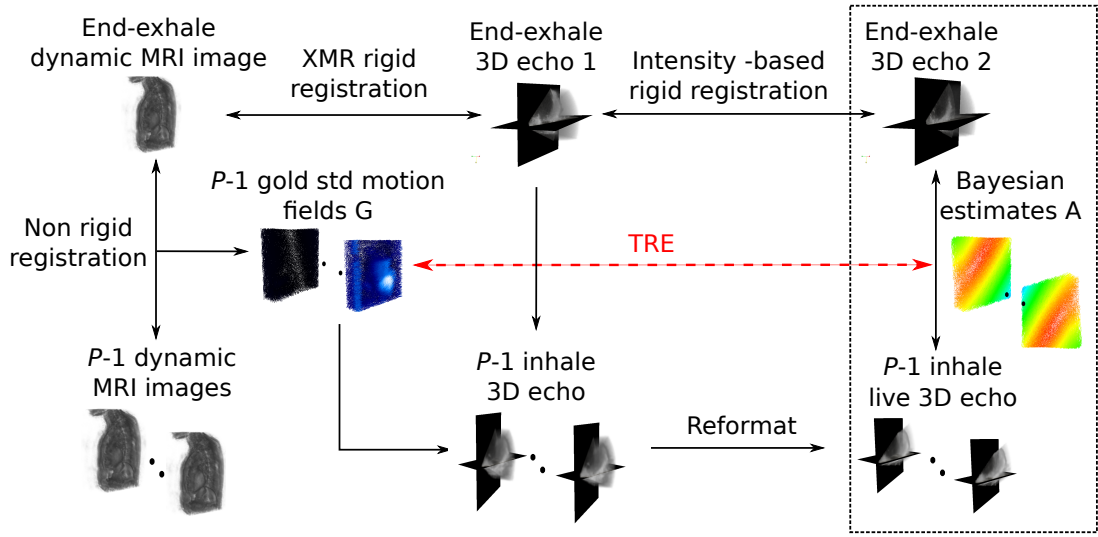


FIGURE 7.2: Overview of the evaluation approach. The dynamic calibration scan of the left-out subject is used to generate a set of non-rigid gold-standard motion fields  $G$ . This set of gold-standard motion fields is used to create the synthetic live 3D echo images and to compute Target Registration Errors (TREs) in estimation accuracy.

- (B) - *Personalised prior*: the proposed method. The prior probability density function was formed using only the respiratory motion estimates of the  $K$  datasets predicted by the personalisation framework.
- (C) - *Subject-specific prior*: as in Chapter 4, the prior probability density function was formed using the  $P = 40$  motion estimates derived from the subject-specific dynamic calibration scan. The estimation accuracy of this subject-specific Bayesian technique represents the best possible estimation accuracy achievable by techniques (A) and (B). For this experiment, a leave-one-out cross-validation was used to form the prior probability function, meaning that the prior for the  $p$ -th dynamic position was formed by leaving out the corresponding affine motion estimate.

An example of different probability density functions for the first affine parameter (AP translation) is shown in Figure 7.3. Note that the overall prior probability function is given by the product of the 12 probability density functions, one for each affine parameter. As can be noted in Figure 7.3, the probability function distributions of the affine parameters are affected by the number of estimates employed for the formation. Since the population-based probability density functions use  $P \times N$  motion estimates, the variance of the corresponding Gaussian function is high, resulting in wide probability density functions (see first column of Figure 7.3). On the other hand, the personalised

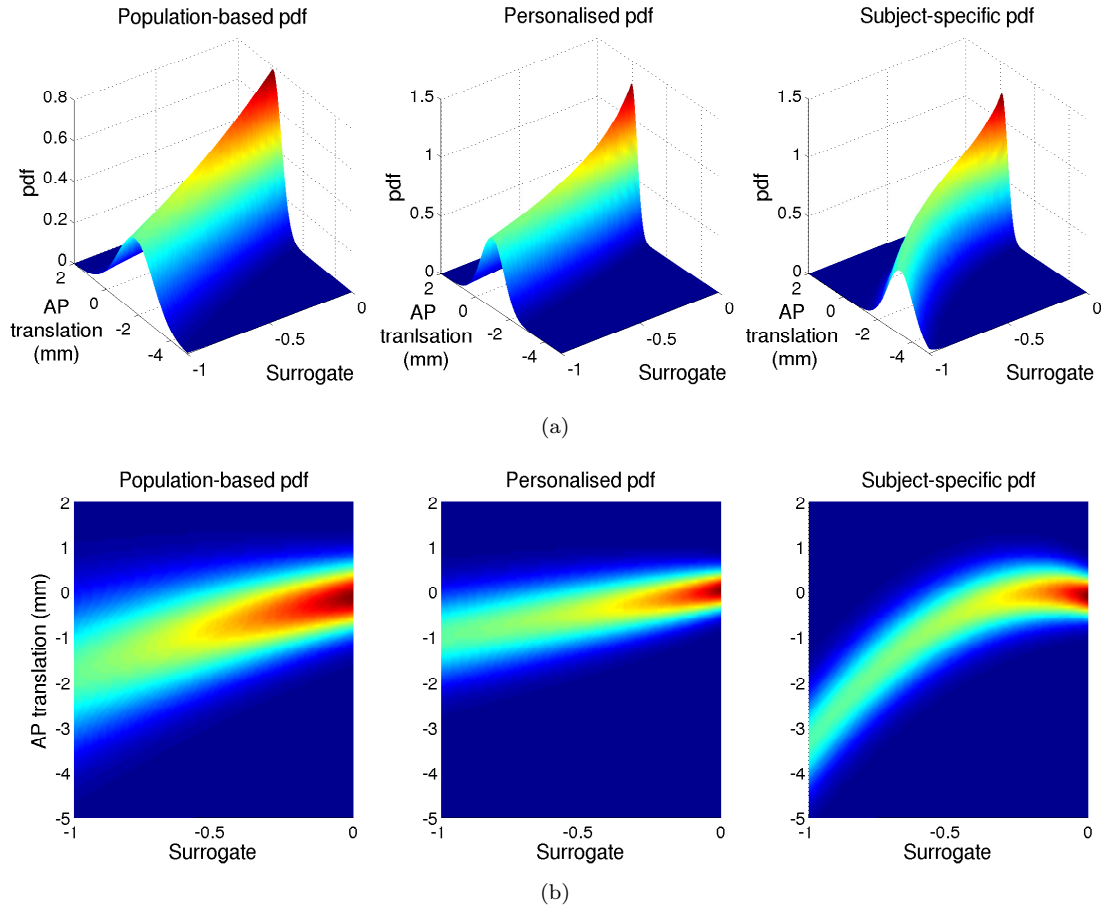


FIGURE 7.3: Example of probability distribution functions of the AP translation for Vol. 13. The first column of Figures (a)-(b) shows the probability density function using the  $N \times P$  estimates derived from the population sample  $N$ , while in the second column only the  $K \times P$  estimates corresponding to the  $K$  datasets chosen by the NAF are used to form the probability function. The last column shows the subject-specific probability function formed using the subject-specific  $P$  estimates of AP translation.

probability density functions are formed using  $P \times K$  motion estimates. As a result, the variance of the Gaussian functions is lower compared to the population-based functions (see second column of Figure 7.3). Subject-specific probability density functions (see third column of Figure 7.3) are formed using the  $P$  subject-specific motion estimates, resulting in narrow Gaussian functions.

Results on estimation accuracy are reported in the following Section 7.4.

## 7.4 Results

Median and 95<sup>th</sup> quantile of the TREs in estimation accuracy for Vol. 13-16 are reported in Table 7.1. Compared to the population-based Bayesian motion estimation

	Median/95 <sup>th</sup> quantile of TRE (mm)			Impr. (%)
	<i>Pop-based prior</i> (A)	<i>Personalised prior</i> (B)	<i>Sub-spec prior</i> (C)	
Vol. 13	1.0/4.9	1.0/4.6	0.9/3.3	0.0/6.1
Vol. 14	1.4/3.4	1.4/3.0	1.1/2.5	0.0/11.8
Vol. 15	1.3/4.3	1.4/4.8	1.1/3.6	-7.6/-11.6
Vol. 16	1.2/4.6	1.2/4.4	0.9/3.4	0.0/4.4

TABLE 7.1: Results of the evaluation of estimation accuracy for the three Bayesian estimation techniques compared. Median and 95<sup>th</sup> quantile of the TREs are reported in *mm*. The last column shows the improvement in median/95<sup>th</sup> quantile achieved by the personalised Bayesian technique (B) against the population-based Bayesian technique (A).

(A), the proposed personalised Bayesian estimation (B) produced improvements in the 95<sup>th</sup> quantile of TRE for Vol. 13, 14 and 16 of approximately 6%, 12% and 4%, respectively. For Vol. 15, worse motion estimates were produced by the proposed technique (B) compared to technique (A). A statistically significant difference was found for each dataset and for each technique compared (Mann Whitney U-test,  $p < 0.01$ ).

By comparing these results with the improvements in accuracy achieved in Chapter 6 by the personalised motion model against the population-based motion model (i.e. 11% for Vol. 13, 40% for Vol. 14, -21% for Vol. 15 and 35% for Vol. 16 for the 95<sup>th</sup> quantile of TRE), a similar pattern can be observed. In particular, it can be noted that improvements were achieved for the subjects where the personalisation framework was more effective (i.e. Vol. 13, 14 and 16), providing a prior probability function more similar to the subject-specific prior. However, the amount of improvement achieved in this experiment is significantly less than the improvements achieved in the previous Chapter. This is probably due to the Bayesian formulation which allows the likelihood term (i.e. the echo images) to affect the final motion estimation. Furthermore, as shown in the first column of Figure 7.3, the population-based probability density functions have a higher variance compared to the personalised probability functions due to the higher number of motion estimates used. This higher variance effectively makes the prior weaker, allowing the likelihood term to have more weight. As a consequence, the difference in motion estimation found in Chapter 6 is reduced and closer estimation accuracies are achieved for techniques (A) and (B). It can also be noted that for Vol. 15, as mentioned in Chapter 5, the quality of the echo images was poor, meaning that the prior probability function influenced the final motion estimate more than the

likelihood, thus maintaining the lower estimation accuracy of the personalised model compared to the population-based model.

For this experiment, the closest  $K = 3$  neighbours were used for the prior formation. It is possible that the estimation accuracy could benefit from a higher number of  $K$ , since probability density functions for the affine parameters with higher variance but still close to the subject-specific density functions would be generated.

## 7.5 Discussion

In this Chapter, as a proof of concept, the novel techniques previously presented in Chapter 4 and Chapter 6 were combined to derive a Bayesian respiratory motion model that does not require a dynamic calibration scan of the subject under investigation. In particular, the personalisation framework based on anatomical features only (see Chapter 6) was employed to select a subset from the population sample more likely to represent the respiratory motion of the out-of-sample subject. The respiratory motion estimates derived from the dynamic calibration scans of the  $K$  selected datasets were employed to build the prior probability density function. In the proposed workflow, during the procedure, the live 3D echo images and the surrogate would be acquired and used to derive the Bayesian respiratory motion estimates. This method represents one simple way of combining the personalisation framework and the Bayesian motion estimation, although other approaches could be employed.

Compared to a population-based Bayesian technique, improvements in estimation accuracy were achieved for three datasets out of four. The amount of improvement achieved followed the improvements achieved by the personalisation framework alone, highlighting the importance of the prior information in the Bayesian motion estimation. As a general observation, it can be noted from the results that both Bayesian techniques (A) and (B) provided an accuracy in motion estimation lower than  $1.5mm$  for the median and lower than  $5mm$  for the  $95^{th}$  quantile of TREs for the four datasets considered, with no need for a subject-specific calibration scan. Recalling that an estimation accuracy of  $5mm$  is desirable in many catheterisation procedures (see Section 2.3), the population-based Bayesian motion estimation techniques (A) and (B) have been shown to fulfil the clinical requirements without further complications of the clinical workflow. In this context, the population-based Bayesian techniques represent

suitable and viable solutions for the uptake of respiratory motion modelling techniques in the clinical routine.

For the three Bayesian techniques compared in this Chapter, the empirical formulation for the optimal  $\sigma_l^2$  devised in Chapter 4 was used. However, this empirical formulation was obtained for subject-specific prior probability functions, and therefore, the derived  $\sigma_l^2$  might not be optimal for the population-based and personalised prior probability functions. Better accuracy results for these Bayesian motion models could be achieved by adapting the empirical formulation for  $\sigma_l^2$  to the different prior probability functions.

The input to the personalisation framework is a high resolution 3D MRI image of the heart, while the Bayesian motion estimation technique requires a reference 3D echo image and live 3D echo images for the formation of the likelihood term. As mentioned in Section 7.2.2, the Bayesian motion estimates could be computed without the acquisition of a surrogate signal, simplifying further the acquisition protocol. An interesting future direction would be to use 3D echo images to personalise and drive the population-based Bayesian motion estimation, eliminating the need for the high resolution MRI image. Robust multi-modality registration algorithms (Penney et al., 2008; King et al., 2009b; Hu et al., 2012; Heinrich et al., 2013; Kuklisova-Murgasova et al., 2013) and compounding algorithms for the echo images (Yao et al., 2011) could be employed to derive the anatomical deformations used to personalise the prior probability function.

In the next Chapter, a summary of the methods and the findings presented in this thesis is provided, along with a discussion on clinical applications of the proposed techniques and future directions. Finally, some conclusions are drawn on the contributions brought by this thesis and its possible clinical impact.

## Chapter 8

# Conclusions

### Contents

---

<b>8.1</b>	<b>Summary . . . . .</b>	<b>121</b>
<b>8.2</b>	<b>Clinical Impact . . . . .</b>	<b>123</b>
<b>8.3</b>	<b>Current Limitations and Future Directions . . . . .</b>	<b>124</b>
<b>8.4</b>	<b>Conclusions . . . . .</b>	<b>127</b>

---

A summary of the original contributions introduced in this thesis is presented in Section 8.1. Although examples of clinical applications of the proposed methods have been given in each of the corresponding Chapters, Section 8.2 summarises the impact that the proposed techniques could have on clinical practice. In Section 8.3, an analysis of the current limitations of the proposed methods is provided, along with possible future directions to address such limitations. Finally, some overall conclusions are drawn in Section 8.4.

### 8.1 Summary

This thesis focused on the problem of respiratory motion in image-guided cardiac interventions (IGIs). Respiratory motion causes misalignments between the static pre-procedure information used for guidance and the intra-procedure moving anatomy, resulting in misleading guidance information. A viable solution to this problem is represented by respiratory motion modelling techniques. However, to date these techniques remain mostly a research topic with very limited clinical uptake. The main reasons behind this lack of clinical translation lie in the poor accuracy and robustness

of the techniques proposed to date, and to the extra burden they impose on the clinical workflow.

This thesis aimed to address the limitations of previously proposed motion modelling techniques by devising novel and effective methods that address the lack of accuracy/robustness and facilitate the clinical application of respiratory motion models. The subject-specific Bayesian respiratory motion model proposed in Chapters 4 and 5 has proven to be more accurate than state-of-the-art motion estimation techniques. The gain in accuracy is due to the probabilistic formulation that allows the robustness of a direct correspondence motion model to be combined with the rich and real-time information provided by 2D/3D echo imaging. The Bayesian formulation allows the uncertainty in motion estimation to be modelled and subsequently resolved using real-time intra-procedure information. A novel automatic echo acquisition system was also proposed as a proof of concept for the use of echo images as intra-procedure imaging in routine IGIs. The proposed framework uses a respiratory motion model to control the acquisition of 2D echo images, thus providing compensation for respiratory motion in the acquired images. The compensated images lead to more accurate motion model estimates and can be useful for continuous targeting of a specific anatomy in the heart.

The second major contribution of this thesis is represented by the personalisation framework proposed in Chapter 6. The method provides accurate motion model estimates with no need for the subject-specific dynamic calibration scan that often interrupts and complicates the clinical workflow. The personalisation framework selects a set of subjects from an already available population sample that best represents the respiratory motion of the subject under investigation. The selection is based on static anatomical information only, without any need for subject-specific respiratory motion information. The promising results achieved suggest a correlation between the anatomical features of the heart and its respiratory motion. This finding needs further investigation but if confirmed could have a significant impact both on current knowledge of respiratory motion physiology and also in a range of clinical applications, as discussed in the next Section.

Finally, the personalised Bayesian motion model proposed in Chapter 7 combines the accuracy/robustness of the Bayesian formulation with the ease of formation of the personalisation framework, resulting in a more accurate/robust respiratory motion



model with no need for a dynamic calibration scan. This proof of principle shows what the future of respiratory motion modelling in routine IGIs could be.

## 8.2 Clinical Impact

The potential impact of the proposed methods in terms of clinical applications can be summarised as follows:

- the subject-specific and personalised Bayesian motion model presented in Chapter 4 and Chapter 7 could have a direct impact on standard electrophysiology (EP) studies and catheter ablation procedures, as well as on procedures with high accuracy requirements, such as stem cell implantation, or the mapping of ablated points following an ablation procedure. EP studies are normally carried out while the patient is sedated and freely breathing, so the Bayesian respiratory motion model could improve the accuracy of the measurements and shorten the overall time of the procedure, which usually lasts 1 to 4 hours ([www.heart.com](http://www.heart.com));
- the automatic motion model-driven echo acquisition framework proposed in Chapter 5 is a proof of principle of how information about respiratory motion can be used not only for motion correction but also to improve image acquisition. The resulting motion compensated images can be used for more robust motion estimation or for continuous imaging of regions of interest. This application could be particularly interesting for cardiac valve replacement procedures, where the valve plane could be continuously imaged despite the respiratory motion of the heart. In Chapter 5, automatic control using a robotic arm was proposed to steer the echo probe according to the respiratory motion model estimates. Medical robotics is a rapidly expanding field, and many successful clinical implementations have been reported (Lanfranco et al., 2004). In Cleary (2005), an overview of the technological requirements for the operating room of the future is provided. Amongst these technological requirements, medical robotics and surgery-specific image acquisition, processing and displays are suggested as the cornerstones of the surgical systems of the next generation. The proposed model-driven image acquisition fits appropriately into such a scenario;

- the clinical applications for the personalisation framework proposed in Chapter 6 range from image acquisition to IGIs and radiotherapy (RT) treatment. For instance, in MRI acquisition, the personalised model could be used to improve imaging efficiency by estimating in real-time the respiratory motion of the heart. The anatomical features could be derived in a few seconds from the anatomical survey scan and the personalised model could be subsequently applied to any following sequence with no need for respiratory gating techniques, thus speeding up the acquisition and reducing costs. In IGIs and RT treatment, a high resolution image already available in the clinical record of the patient could be used to personalise the model, removing the need for any pre-procedure scan and exploiting the imaging information already available. Given the non-rigid formulation of the personalisation framework, any organ affected by respiratory motion could be modelled, thus widening its clinical application;
- the proposed personalisation framework has also shown how image processing and machine learning techniques can be used to investigate and provide insights into physiological processes. In this case, the correlation between the morphology and position of the heart and its respiratory motion was investigated for the first time, showing significant results that, if confirmed, could have a significant impact on current knowledge of respiratory motion.

### 8.3 Current Limitations and Future Directions

In this Section, the main limitations and simplifying assumptions that affect the proposed methods are analysed. For each limitation, possible solutions that could represent future investigations are discussed and presented.

**Clinical evaluation.** The motivation of this thesis was to devise novel techniques to foster the uptake of respiratory motion models in clinical practice. Even though the final aim would be the application of the proposed methods in clinical routine as summarised in the previous Section, it is necessary to point out that the focus of this thesis was the development and the feasibility evaluation of such novel techniques, rather than their clinical evaluation. In fact, the results presented constitute a preliminary evaluation on a rather small sample of healthy

volunteers. Further extensive evaluation on a patient cohort is required to test the robustness of the proposed methods. Such extensive evaluation was out of the scope of this thesis and might be the focus of future work.

**Impact of echo acquisition on the intra-procedure workflow.** The Bayesian motion estimation techniques used in Chapters 4, 5 and 7 make use of intra-procedure 2D/3D echo images to compute the respiratory motion model estimates. As mentioned in Section 2.2.2, echo imaging is not currently routinely employed as an intra-procedure imaging modality in IGIs. However, the United States Food and Drug Administration has recently approved for market a system to intra-operatively integrate X-ray fluoroscopy images with 3D transoesophageal echo images for cardiac IGIs (EchoNavigator system, Philips Healthcare). Moreover, significant results using echo imaging for guidance in EP studies have been reported (Wein et al., 2008, 2009). This represents an important step forward in the use of intra-procedure echo images in routine interventional procedures. In the foreseeable future, it is possible that intra-procedure echo images could be routinely acquired, making the proposed techniques suitable for application at no extra burden to the intra-procedure workflow.

**Affine formulation of the Bayesian motion model.** In its current formulation, the Bayesian respiratory motion estimation technique is able to model affine deformations only. An affine deformation model was chosen since it represented the best trade-off between modelling accuracy and computational efficiency. As reported in Section 2.1.2, most of the previous works on cardiac respiratory motion modelling showed an affine model to be accurate enough to represent the deformations of the heart due to respiration (Manke et al., 2002a; Shechter et al., 2004; King et al., 2009a). The optimisation of the posterior probability function (see Equation 4.2) can be expensive from a computational standpoint, requiring the computation of the likelihood and prior at each iteration of the optimisation algorithm. Therefore, an affine Bayesian motion model (with 12 degrees of freedom plus the surrogate signal) is much more computationally efficient than would be a non-rigid Free-Form Deformation (FFD) model (with thousands of degrees of freedom). However, in order to extend the Bayesian respiratory motion model to other organs, non-linear deformations would need to be included in

the modelling process. Initial investigations on this limitation have been carried out, employing dimensionality reduction techniques to allow the representation of high dimensional non-rigid deformations by means of a few degrees of freedom. In particular, supervised Principal Component Analysis (sPCA) (Barshan et al., 2011) showed promising results in reducing the high dimensional space of non-rigid respiratory deformations to a few ( $< 6$ ) Principal Components (PCs). The Bayesian formulation could be applied to the PCs, allowing modelling of more complex motion deformations. In this formulation, the likelihood function would need to be modified accordingly. Furthermore, the choice of an affine description for cardiac respiratory motion also depended on the field of view (FoV) of the MRI dynamic calibration scan. In fact, as described in Appendix A, the FoV of the dynamic images covered most, but not all, of the main chambers and vessels of the heart. Moreover, the FoV varied between subjects, depending on the size of the heart. Therefore, an affine transformation allowed the estimation of respiratory deformations also outside the imaged FoV, making it possible to estimate the respiratory motion of the whole heart. It is likely that for other organs, which are less affected by cardiac cycle motion, dynamic images of the whole organ could be acquired, making whole organ non-rigid motion estimates feasible.

**Real-time implementation of the Bayesian motion estimation.** In order to use the estimates of the respiratory motion model for intra-procedure guidance, such model estimates need to be produced in near real-time. In the current implementation of the Bayesian motion model, this requirement is not met. However, as mentioned in Section 4.5, code optimisation was not the focus of this work and would need to be considered for real-time application.

**Limitations of the personalisation framework.** The personalisation framework proposed in Chapter 6 currently requires a high resolution MRI image in order to compute the anatomical deformations and derive the  $K$  neighbours used to build the motion model. The same results could be achieved by using an image derived from pre-procedure CT or even possibly intra-procedure rotational X-ray angiography. The underlying assumption in deriving the anatomical features is that the position of the patient in the imaging scanner does not affect the

anatomical features used for classification. This assumption needs to be further investigated, but it seems plausible in the case of a MRI scanner, where the position of the subject is very constrained, and thus repeatable. As mentioned in Section 6.7, a very interesting future investigation would be to employ 3D echo images to derive the anatomical deformations, thus resolving many issues associated with MRI (compatibility with magnetic field, high acquisition time and costs) and CT (ionising radiation). However, a larger FoV for the echo images covering the whole heart and more robust registration techniques would be required. Furthermore, in a future extension of the personalisation framework, intra- and inter-cycle motion variability could be included in the motion similarity quantification step and in the final motion model building.

## 8.4 Conclusions

As pointed out in McClelland et al. (2013), several reasons can explain the current lack of translation of respiratory motion modelling techniques from research to the clinic. First, the clinicians do not trust this technology due to a lack of accuracy/robustness and proper validation on clinically realistic data. Second, the impact on the clinical workflow might still be too high to justify widespread use in routine cardiac IGIs. Third, clinicians have adopted other coping strategies to deal with respiratory motion and might be reluctant to switch to new unproven solutions. The novel methods proposed in this thesis go towards addressing the first and second reasons. The promising results reported in this work might stimulate the interest of clinicians and companies in the field of IGIs to further validate the proposed methods, thus addressing the third reason. Such validation could lead to the adoption and integration of the proposed respiratory motion modelling techniques in routine cardiac IGIs.

# Appendix A

## Data Acquisition

### Contents

---

<b>A.1 MRI Acquisition . . . . .</b>	<b>128</b>
<b>A.2 Echo Acquisition . . . . .</b>	<b>129</b>
<b>A.3 Datasets . . . . .</b>	<b>131</b>

---

To evaluate the methods proposed in this thesis, MRI and echo images of the hearts of adult healthy volunteers were acquired. For the sake of clarity, this Appendix reports details of the MRI and echo acquisition protocols and the datasets acquired. In particular, Section A.1 details the MRI sequences employed, while Section A.2 presents details of the echo acquisition. Finally, Section A.3 reports which datasets were used to evaluate the methods proposed in Chapters 4, 5, 6 and 7.

### A.1 MRI Acquisition

The MRI images were acquired using a 1.5T Philips Achieva MRI scanner (Philips, The Best, Netherlands). The sequence details of the dynamic calibration scan used for forming the motion models are:

**Dynamic 3D :** 3D TFEPI, ECG-triggered and gated at late diastole, typically 20 slices,  $TR = 10ms$ ,  $TE = 4.9ms$ , flip angle =  $20^\circ$ , acquired voxel size  $2.7 \times 3.6 \times 8.0mm^3$ , reconstructed voxel size  $2.22 \times 2.22 \times 4.0mm^3$ , TFE factor 26, EPI factor 13, TFE acquisition time  $267.9ms$ .

The dynamic 3D sequence was ECG-triggered and gated, so one volume was acquired for each heart beat. The images therefore represented the motion of the heart due to

respiration only. Compared to the dynamics of respiration, the short acquisition time ( $267.9ms$ ) allows acquisition of near motion-free 3D images. 2-4 dynamic volumes were typically acquired for each breathing cycle. The acquisition time for each dynamic image put restrictions on the coverage of the dynamic scans, therefore the field of view (FoV) covered most, but not all, of the four chambers of the heart.

In addition, for each dataset, a high resolution 3D image was acquired:

**High resolution 3D :** 3D balanced TFE, cardiac gated at late diastole, respiratory gated at end-exhale,  $5mm$  navigator window, typically 120 sagittal slices,  $TR = 4.4ms$ ,  $TE = 2.2ms$ , flip angle =  $90^\circ$ , acquired voxel size  $2.19 \times 2.19 \times 2.74mm^3$ , reconstructed voxel size  $1.37 \times 1.37 \times 1.37mm^3$ , the acquisition window was optimised for each volunteer and was on average  $100ms$ , scan time  $\sim 5$  minutes.

The high resolution MRI image is a standard pre-procedure acquisition in many clinical protocols and provides high spatial resolution information about the anatomy and pathology of the heart.

## A.2 Echo Acquisition

Experiments were carried out in an XMR catheterisation suite (Rhode et al., 2003, 2005). This system allows automatic determination of the MRI to patient rigid transformation, employing an Optotrak 3020 optical tracking system (Northern Digital Inc.) to track the patient bed. The acquisition setup is shown in Figure A.1.

Echo images were acquired using an iE33 3-D real-time echocardiography system with a X3-1 3 to 1 MHz broadband matrix array transducer (Philips Healthcare). Light emitting diodes attached to the echo probe were tracked using the Optotrak tracking system, allowing registration of the echo images to the physical space of the XMR suite (see Figure A.1). The image-to-probe calibration method proposed by Ma et al. (2009) was employed. Following the calibration/tracking based registration framework described in King et al. (2010a), the MRI to echo imaging rigid transformation was computed.

The geometric characteristics of the 3D live US beam, in pyramidal coordinate system, were: inclination angle =  $30^\circ$ , inclination offset =  $-1^\circ$ , azimuthal angle =  $55^\circ$ , azimuthal offset =  $-27.5^\circ$ , radial depth =  $140mm$ . For the echo machine employed, the standard 3D echo images are acquired over four beating cycles of the heart, i.e.



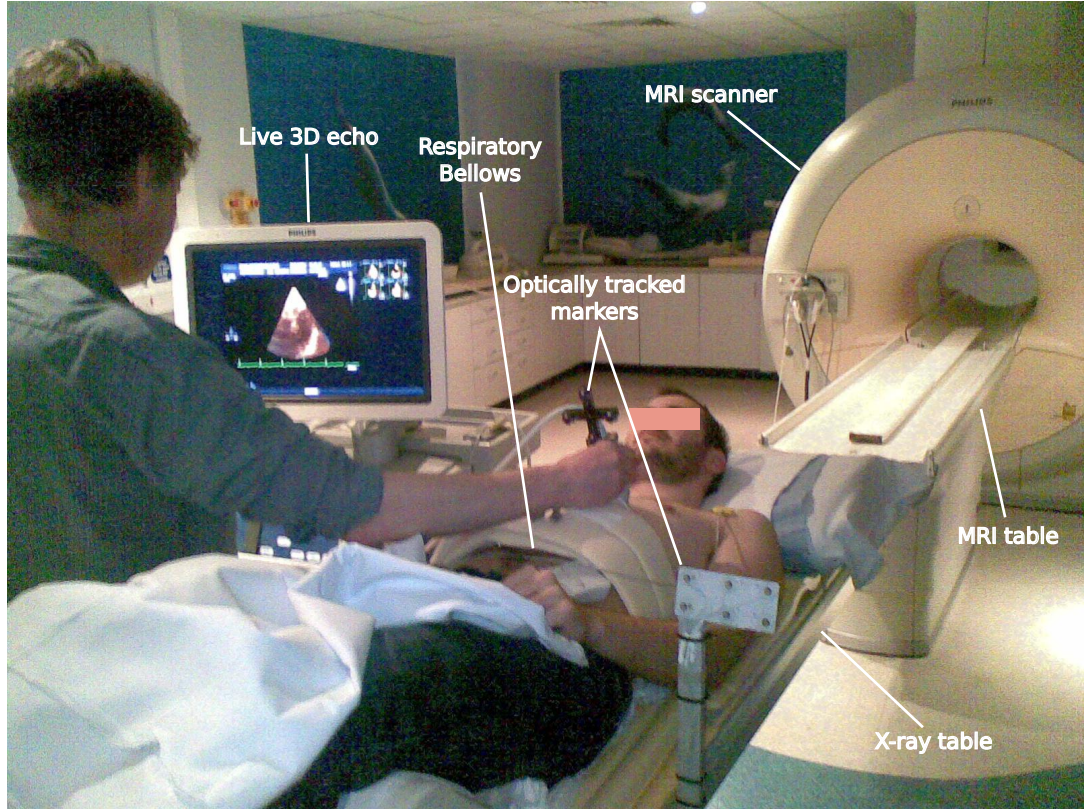


FIGURE A.1: Setup of the XMR suite for the acquisition of 3D echo images.

they are compounded from 4 smaller volumes, each acquired in a single heart beat. Therefore, the volume imaged by a standard echo image is four times bigger than the volume imaged by 3D live echo images.

Four volunteer datasets (see Table A.1) were acquired. For each dataset, 4 standard 3D echo images were acquired during end-exhale breath-hold and 12 sequences of free-breathing live 3D echo images were acquired. Of the 12 free-breathing sequences, 6 sequences were acquired during normal breathing, 3 during fast breathing and 3 during deep breathing. Each sequence lasted approximately 4 seconds and live echo images were streamed at a rate of 14 images per second. However, since the MRI-derived motion model describes the heart's position at end-diastole, the echo images were manually retrospectively gated at end-diastole, resulting in 4 to 6 live echo images per sequence. All images were acquired from modified parasternal acoustic windows. For details of the use of the standard and live 3D echo images for the evaluation of the proposed methods, please refer to the corresponding Chapters.



### A.3 Datasets

Table A.1 reports the datasets used to evaluate the methods proposed in this thesis and the number of dynamic images in the calibration scan used to build the motion models. Furthermore, the last column of Table A.1 reports whether or not real echo imaging data were available.

In Chapter 4, 9 datasets (Vol. 1-9) were used to evaluate the Bayesian motion estimation on simulated echo images and 4 datasets (Vol. 13-16) were used for the evaluation on real echo images. As reported in Table A.1, the dynamic calibration scan acquired 300 images for Vol. 1-4 and 120 images for Vol. 5-9 and Vol. 13-16. In order to capture the variability in respiratory motion, the volunteers were asked to breathe in three different ways: normal, shallow and deep breathing. For Vol. 1-4, 100 dynamic images were acquired for each different breathing pattern, while for Vol. 5-9 and Vol. 13-16 40 dynamic images were acquired for each breathing pattern. As reported in the last column of Table A.1, real echo images were acquired for Vol. 13-16.

To evaluate the model-driven echo acquisition framework proposed in Chapter 5, the datasets Vol. 13-16 were employed. To allow the modelling of respiratory variability, all 120 dynamic images acquired during normal, shallow and deep breathing were considered.

All 28 volunteer datasets were considered to evaluate the personalisation framework for population-based motion models proposed in Chapter 6. The framework was evaluated considering only 40 dynamic images acquired during normal breathing for each volunteer (the first 40 of the 100 images for datasets Vol. 1-4 were considered).

Given the availability of the echo images, datasets Vol. 13-16 were employed for the evaluation of the personalised Bayesian motion estimation. However, since the method employs the personalisation framework presented in Chapter 6, all 28 volunteer datasets were used to build the population-based model used for Vol. 13-16. Again, only the 40 dynamic images corresponding to normal breathing were utilised.

For details of how the echo images were processed and which respiratory surrogate was employed to build the motion models, please refer to the specific Chapters.

Vol.	Chapter 4		Chapter 5		Chapter 6		Chapter 7		Echo images
	Used	$P$	Used	$P$	Used	$P$	Used	$P$	
1	✓	300	—	—	✓	40	—	—	—
2	✓	300	—	—	✓	40	—	—	—
3	✓	300	—	—	✓	40	—	—	—
4	✓	300	—	—	✓	40	—	—	—
5	✓	120	—	—	✓	40	—	—	—
6	✓	120	—	—	✓	40	—	—	—
7	✓	120	—	—	✓	40	—	—	—
8	✓	120	—	—	✓	40	—	—	—
9	✓	120	—	—	✓	40	—	—	—
10	—	—	—	—	✓	40	—	—	—
11	—	—	—	—	✓	40	—	—	—
12	—	—	—	—	✓	40	—	—	—
13	✓	120	✓	120	✓	40	✓	40	✓
14	✓	120	✓	120	✓	40	✓	40	✓
15	✓	120	✓	120	✓	40	✓	40	✓
16	✓	120	✓	120	✓	40	✓	40	✓
17	—	—	—	—	✓	40	—	—	—
18	—	—	—	—	✓	40	—	—	—
19	—	—	—	—	✓	40	—	—	—
20	—	—	—	—	✓	40	—	—	—
21	—	—	—	—	✓	40	—	—	—
22	—	—	—	—	✓	40	—	—	—
23	—	—	—	—	✓	40	—	—	—
24	—	—	—	—	✓	40	—	—	—
25	—	—	—	—	✓	40	—	—	—
26	—	—	—	—	✓	40	—	—	—
27	—	—	—	—	✓	40	—	—	—
28	—	—	—	—	✓	40	—	—	—

TABLE A.1: Details of the datasets employed in this thesis. For each Chapter, the first column denotes whether or not the dataset was used for evaluation purposes, while the second column reports the number of dynamic images  $P$  used to build the motion models. The last column reports the availability of real echo imaging in the dataset.

## Appendix B

# Neighbourhood Approximation Forest

In the training phase, the training features were the anatomical deformation fields  $\mathbf{t}_{atlas \rightarrow n}^H \in \mathbb{R}^{H \times 3}$ ,  $n = 1, \dots, N$  defined over the  $H$  voxels of the binary mask covering the heart of the atlas. At each node of each tree in the forest, a small subset of these features  $\mathbf{t}_{atlas \rightarrow n}^h$ ,  $h \ll H$  was randomly selected to determine the optimal branching, splitting subjects into two sets (Konukoglu et al., 2013). The randomness of the feature selection created decorrelated trees and independent predictions.

The set of subjects  $\mathbf{I}_q$  at each node  $q$  were split into subsets  $\mathbf{I}_{q_l}$  and  $\mathbf{I}_{q_r}$ , corresponding to the left and right child nodes, respectively. This split was determined by using a binary test  $b_q(I_n; m, \boldsymbol{\tau})$

$$b_q(I_n; m, \boldsymbol{\tau}) = \begin{cases} I_n \in \mathbf{I}_{q_r}, & \text{if } \mathbf{t}_{atlas \rightarrow n}^m > \boldsymbol{\tau}, \\ I_n \in \mathbf{I}_{q_l}, & \text{if } \mathbf{t}_{atlas \rightarrow n}^m \leq \boldsymbol{\tau}, \end{cases} \quad \forall I_n \in \mathbf{I}_q, \quad (\text{B.1})$$

where  $\mathbf{t}_{atlas \rightarrow n}^m$  denotes the  $m^{th}$  vector of  $\mathbf{t}_{atlas \rightarrow n}^h$  and  $\boldsymbol{\tau} = [\tau_x, \tau_y, \tau_z] \in \mathbb{R}^3$ . Equation (B.1) corresponds to a vectorial extension of equation (1) in Konukoglu et al. (2013). In particular, the comparison  $\mathbf{t}_{atlas \rightarrow n}^m > \boldsymbol{\tau}$  was performed component-wise, which means that the right child node was chosen iff  $t_{atlas \rightarrow n_x}^m > \tau_x$  and  $t_{atlas \rightarrow n_y}^m > \tau_y$  and  $t_{atlas \rightarrow n_z}^m > \tau_z$ , otherwise the left child node was chosen.

The optimisation was carried out with respect to  $m$  and  $\boldsymbol{\tau}$  in order to achieve the most compact partitioning of  $\mathbf{I}_q$ . As proposed by Konukoglu et al. (2013), the cluster

size  $C_\rho(\mathbf{A})$  of a set  $\mathbf{A}$  with respect to  $\rho(\cdot, \cdot)$  was defined as

$$C_\rho(\mathbf{A}) = \frac{1}{|\mathbf{A}|^2} \sum_{I_i \in \mathbf{A}} \sum_{I_j \in \mathbf{A}} \rho(I_i, I_j), \quad (\text{B.2})$$

where  $|\mathbf{A}|$  was the number of samples in  $\mathbf{A}$ . Given  $m$  and  $\boldsymbol{\tau}$ , the gain in compactness due to the splitting was defined as

$$G(\mathbf{I}_q, m, \boldsymbol{\tau}) = C_\rho(\mathbf{I}_q) - \frac{|\mathbf{I}_{q_r}|}{|\mathbf{I}_q|} C_\rho(\mathbf{I}_{q_r}) - \frac{|\mathbf{I}_{q_l}|}{|\mathbf{I}_q|} C_\rho(\mathbf{I}_{q_l}). \quad (\text{B.3})$$

The best possible binary test at each node  $q$  was therefore determined by optimising

$$(m_q, \boldsymbol{\tau}_q) = \arg \max_{m, \boldsymbol{\tau}} G(\mathbf{I}_q, m, \boldsymbol{\tau}), |\mathbf{I}_{q_r}| \geq \Delta, |\mathbf{I}_{q_l}| \geq \Delta, \quad (\text{B.4})$$

where  $\Delta$  was the minimum allowed number of samples per node.

For each feature vector  $m$  in the subset  $h$ , the values of  $\tau_x, \tau_y, \tau_z$  were exhaustively optimised in the ranges of variation of the components of  $\mathbf{t}_{atlas \rightarrow n}^m, \forall I_n \in \mathbf{I}_q$ .

The best feature  $m_q$  and corresponding  $\boldsymbol{\tau}_q$  for each node  $q$  of each tree in the forest were stored for the personalisation of the out-of-sample subject. The set of  $m_q$  in the forest was used to infer correlation between anatomical features and cardiac respiratory motion (see Figure 6.7).

# Bibliography

- Ablitt, N.A., Gao, J., Keegan, J., Stegger, L., Firmin, D.N., Yang, G.Z., 2004. Predictive cardiac motion modeling and correction with Partial Least Squares Regression. *IEEE Transactions on Medical Imaging* 23, 1315–1324.
- Aljabar, P., Heckemann, R.A., Hammers, A., Hajnal, J.V., Rueckert, D., 2009. Multi-atlas based segmentation of brain images: Atlas selection and its effect on accuracy. *NeuroImage* 46, 726 – 738.
- Atkinson, D., Burcher, M., Declerck, J., Noble, J.A., 2001. Respiratory motion compensation for 3-D freehand echocardiography. *Ultrasound in Medicine & Biology* 27, 1615–1620.
- Barshan, E., Ghodsi, A., Azimifar, Z., Jahromi, M.Z., 2011. Supervised principal component analysis: Visualization, classification and regression on subspaces and submanifolds. *Pattern Recognition* 44, 1357 – 1371.
- Baun, J., 2010. Principles of General & Vascular Sonography.
- Benchetrit, G., 2000. Breathing pattern in humans: diversity and individuality. *Respiration Physiology* 122, 123–129.
- Blackall, J.M., Ahmad, S., Miquel, M.E., McClelland, J.R., Landau, D.B., Hawkes, D.J., 2006. MRI-based measurements of respiratory motion variability and assessment of imaging strategies for radiotherapy planning. *Physics in Medicine and Biology* 53, 4147–4169.
- Blackall, J.M., Penney, G.P., King, A.P., Hawkes, D.J., 2005. Alignment of sparse free-hand 3-D ultrasound with preoperative images of the liver using models of respiratory motion and deformation. *IEEE Transactions on Medical Imaging* 24, 1405–1416.

- Blanc, R., Syrkina, E., Székely, G., 2009. Estimating the confidence of statistical model based shape prediction. *Proc of IPMI* 21, 602–613.
- Brzozowski, L., Ganguly, A., Pop, M., Wen, Z., Bennett, R., Fahrig, R., Rowlands, J.A., 2006. Compatibility of interventional X-ray and magnetic resonance imaging: feasibility of a closed bore XMR (CBXMR) system. *Medical Physics* 33, 3033–45.
- Buerger, C., Schaeffter, T., King, A.P., 2011. Hierarchical adaptive local affine registration for fast and robust respiratory motion estimation. *Medical Image Analysis* 15, 551–564.
- Cleary, K., 2005. Medical robotics and the operating room of the future, in: *Engineering in Medicine and Biology Society, 2005. IEEE-EMBS 2005. 27th Annual International Conference of the*, pp. 7250–7253.
- Cleary, K., Peters, T.M., 2010. Image-guided interventions: Technology review and clinical applications. *Annual Review of Biomedical Engineering* 12, 119–142.
- Davidian, M., Carroll, R.J., 1987. Variance function estimation. *Journal of the American Statistical Association* 82, 1079–1091.
- De Buck, S., Maes, F., Ector, J., Bogaert, J., Dymarkowski, S., Heidbuchel, H., Suetens, P., 2005. An augmented reality system for patient-specific guidance of cardiac catheter ablation procedures. *IEEE Transactions on Medical Imaging* 24, 1512–1524.
- Dowsett, D., Kenny, P., Johnston, R., 2006. *The physics of diagnostic imaging*. A Hodder Arnold Publication, Hodder Arnold.
- Earley, M.J., Showkathali, R., Alzetani, M., Kistler, P.M., Gupta, D., Abrams, D.J., Horrocks, J.A., Harris, S.J., Sporton, S.C., Schilling, R.J., 2006. Radiofrequency ablation of arrhythmias guided by non-fluoroscopic catheter location: a prospective randomized trial. *European Heart Journal* 27, 1223–1229.
- Ector, J., Buck, S.D., Huybrechts, W., Nuyens, D., Dymarkowski, S., Bogaert, J., Maes, F., Heidbuechel, H., 2008. Biplane three-dimensional augmented fluoroscopy as single navigation tool for ablation of atrial fibrillation: Accuracy and clinical value. *Heart Rhythm* 5, 957–964.

- Edwards, P.J., Bello, F., 2010. Editorial. *Progress in Biophysics and Molecular Biology* 103, 157 – 158.
- Efros, A.A., Freeman, W.T., 2001. Image quilting for texture synthesis and transfer, in: ACM (Ed.), SIGGRAPH, Association for Computing Machinery., pp. 341–346.
- Ehman, R.L., Felmlee, J.P., 1989. Adaptive technique for high-definition MR imaging of moving structures. *Radiology* 173, 255–263.
- Ehrhardt, J., Werner, R., Schmidt-Richberg, A., Handels, H., 2009. Prediction of respiratory motion using a statistical 4D mean motion model, in: *Proceedings MICCAI Workshop on Pulmonary Image Processing*, pp. 3–14.
- Ehrhardt, J., Werner, R., Schmidt-Richberg, A., Handels, H., 2011. Statistical modeling of 4D respiratory lung motion using diffeomorphic image registration. *IEEE Transactions on Medical Imaging* 30, 251–265.
- Escolar, J.D., Escolar, A., 2004. Lung hysteresis: a morphological view. *Histology and Histopathology* 19, 159–66.
- Fayad, H., Clement, J., Pan, T., Roux, C., Le Rest, C., Pradier, O., Visvikis, D., 2009. Towards a generic respiratory motion model for 4D CT imaging of the thorax, in: *Nuclear Science Symposium Conference Record (NSS/MIC)*, 2009 IEEE, pp. 3975–3979.
- Fayad, H., Pan, T., Roux, C., Visvikis, D., 2010. A generic respiratory motion model for motion correction in PET/CT, in: *Nuclear Science Symposium Conference Record (NSS/MIC)*, 2010 IEEE, pp. 2455 –2458.
- Figl, M., Rueckert, D., Hawkes, D., Casula, R., Hu, M., Pedro, O., Zhang, D., Penney, G., Bello, F., Edwards, P., 2008. Image guidance for robotic minimally invasive coronary artery bypass, in: Dohi, T., Sakuma, I., Liao, H. (Eds.), *Medical Imaging and Augmented Reality*. Springer Berlin Heidelberg. volume 5128, pp. 202–209.
- Fitzpatrick, J., West, J., Maurer, C.R., J., 1998. Predicting error in rigid-body point-based registration. *IEEE Transactions on Medical Imaging* 17, 694 –702.

- Frangi, A., Rueckert, D., Schnabel, J., Niessen, W., 2002. Automatic construction of multiple-object three-dimensional statistical shape models: application to cardiac modeling. *IEEE Transactions on Medical Imaging* 21, 1151–1166.
- Gao, G., Penney, G., Gogin, N., Cathier, P., Arujuna, A., Wright, M., Caulfield, D., Rinaldi, A., Razavi, R., Rhode, K., 2010. Rapid image registration of three-dimensional transesophageal echocardiography and X-ray fluoroscopy for the guidance of cardiac interventions, in: *Proceedings of the First international conference on Information Processing in Computer-Assisted Interventions*, Springer-Verlag, Berlin, Heidelberg. pp. 124–134.
- Gao, G., Penney, G., Ma, Y., Gogin, N., Cathier, P., Arujuna, A., Mortona, G., Caulfield, D., Gild, J., Rinaldi, C.A., Hancock, J., Redwood, S., Thomas, M., Razavi, R., Gijsbers, G., Rhode, K., 2012. Registration of 3D trans-esophageal echocardiography to X-ray fluoroscopy using image-based probe tracking. *Medical Image Analysis* 16, 38–49.
- Geman, S., McClure, D.E., 1985. Bayesian image analysis: An application to single photon emission tomography., in: *1985 Proceedings of the American Statistical Association. Statistical Computing Section*, pp. 12–18.
- Guttman, M.A., Ozturk, C., Raval, A.N., Raman, V.K., Dick, A.J., DeSilva, R., Karmarkar, P., Lederman, R.J., McVeigh, E.R., 2007. Interventional cardiovascular procedures guided by real-time MR imaging: An interactive interface using multiple slices, adaptive projection modes and live 3D renderings. *Journal of Magnetic Resonance Imaging* 26, 1429–1435.
- Hajnal, J.V., Hill, D.L.G., Hawkes, D.J. (Eds.), 2001. *Medical Image Registration*. CRC Press.
- Hanson, K.M., 1993. Introduction to Bayesian image analysis, in: *SPIE, Medical Imaging : Image Processing*, pp. 716–731.
- Hawkes, D., Penney, G., Atkinson, D., Barratt, D., Blackall, J., Carter, T., Crum, W., McClelland, J., Tanner, C., Tarte, S., White, M., 2007. Motion and biomechanical models for image-guided interventions, in: *Biomedical Imaging: From Nano to Macro*, 2007. ISBI 2007. 4th IEEE International Symposium on.



- He, T., Xue, Z., Xie, W., Wong, S., 2010. Online 4-D CT estimation for patient-specific respiratory motion based on real-time breathing signals, in: *Medical Image Computing and Computer-Assisted Intervention - MICCAI 2010*. Springer Berlin Heidelberg, volume 6363, pp. 392–399.
- Heinrich, M.P., Jenkinson, M., Papież, B.W., Brady, S.M., Schnabel, J.A., 2013. Towards realtime multimodal fusion for image-guided interventions using self-similarities, in: *Medical Image Computing and Computer-Assisted Intervention - MICCAI 2013*. Springer Berlin Heidelberg, pp. 187–194.
- Hicks, G.H., 2000. *Cardiopulmonary Anatomy and Physiology*. W. B. SAUNDERS COMPANY.
- Holland, A.E., Goldfarb, J.W., Edelman, R.R., 1998. Diaphragmatic and cardiac motion during suspended breathing: preliminary experience and implications for breath-hold MR imaging. *Radiology* 209, 483–489.
- Housden, R., Basra, M., Ma, Y., King, A., Bullens, R., Child, N., Gill, J., Rinaldi, C., Parish, V., Rhode, K., 2013. Three-modality registration for guidance of minimally invasive cardiac interventions, in: *Functional Imaging and Modeling of the Heart*. Springer Berlin Heidelberg, volume 7945, pp. 158–165.
- Hu, Y., Ahmed, H.U., Taylor, Z., Allen, C., Emberton, M., Hawkes, D., Barratt, D., 2012. MR to ultrasound registration for image-guided prostate interventions. *Medical Image Analysis* 16, 687 – 703.
- Hub, M., Kessler, M.L., Karger, C.P., 2009. A stochastic approach to estimate the uncertainty involved in B-spline image registration. *IEEE Transactions on Medical Imaging* 28, 1708–1716.
- Hughes, S., McClelland, J., Tarte, S., Lawrence, D., Ahmad, S., Hawkes, D., Landau, D., 2009. Assessment of two novel ventilatory surrogates for use in the delivery of gated/tracked radiotherapy for non-small cell lung cancer. *Radiotherapy and Oncology* 91, 336–341.
- Keall, P.J., Mageras, G.S., Balter, J.M., Emery, R.S., Forster, K.M., Jiang, S.B., Kapatoes, J.M., Low, D.A., Murphy, M.J., Murray, B.R., Ramsey, C.R., Van Herk, M.B., Vedam, S.S., Wong, J.W., Yorke, E., 2006. The management of respiratory

- motion in radiation oncology, report of AAPM Task Group 76. *Medical Physics* 33, 3874+.
- King, A., Blackall, J., Penney, G., Hawkes, D., 2001. Tracking liver motion using 3-D ultrasound and a surface based statistical shape model, in: *Mathematical Methods in Biomedical Image Analysis*, 2001. MMBIA 2001. IEEE Workshop on, pp. 145–152.
- King, A.P., Boubertakh, R., Ng, K.L., Ma, Y.L., Chinchapatnam, P., Gao, G., Schaeffter, T., Hawkes, D.J., Razavi, R., Rhode, K.S., 2008. A technique for respiratory motion correction in image guided cardiac catheterisation procedures, in: *Medical Imaging 2008: Visualization, Image-guided Procedures, and Modelling*.
- King, A.P., Boubertakh, R., Rhode, K.S., Ma, Y.L., Chinchapatnam, P., Gao, G., Tangcharoen, T., Ginks, M., Cooklin, M., Gill, J.S., Hawkes, D.J., Razavi, R.S., Schaeffter, T., 2009a. A subject-specific technique for respiratory motion correction in image-guided cardiac catheterisation procedures. *Medical Image Analysis* 13, 419–431.
- King, A.P., Buerger, C., Tsoumpas, C., Marsden, P., Schaeffter, T., 2012. Thoracic respiratory motion estimation from MRI using a statistical model and a 2-D image navigator. *Medical Image Analysis* 16, 252–264.
- King, A.P., Jansen, C., Rhode, K.S., Caulfield, D., Razavi, R.S., Penney, G.P., 2010a. Respiratory motion correction for image-guided cardiac interventions using 3-D echocardiography. *Medical Image Analysis* 14, 21–29.
- King, A.P., Ma, Y.L., Yao, C., Jansen, C., Razavi, R., Rhode, K.S., Penney, G.P., 2009b. Image-to-physical registration for image-guided interventions using 3D ultrasound and an ultrasound imaging model, in: *Information Processing in Medical Imaging - IPMI 2009*.
- King, A.P., Rhode, K.S., Ma, Y., Yao, C., Jansen, C., Razavi, R., Penney, G.P., 2010b. Registering pre-procedure volumetric images with intra-procedure 3-D ultrasound using an ultrasound imaging model. *IEEE Transactions on Medical Imaging* 29, 924–937.

- King, A.P., Rhode, K.S., Razavi, R.S., Schaeffter, T.R., 2009c. An adaptive and predictive respiratory motion model for image-guided interventions: Theory and first clinical application. *IEEE Transactions on Medical Imaging* 28, 2020–2032.
- King, A.P., Tsoumpas, C., Buerger, C., Schulz, V., Marsden, P., Schaeffter, T., 2011. Real-time respiratory motion correction for simultaneous PET-MR using an MR-derived motion model, in: *Nuclear Science Symposium and Medical Imaging Conference (NSS/MIC)*, 2011 IEEE, pp. 3589–3594.
- Klinder, T., Lorenz, C., 2012. Respiratory motion compensation for image-guided bronchoscopy using a general motion model, in: *Biomedical Imaging (ISBI)*, 2012 9th IEEE International Symposium on, pp. 960–963.
- Klinder, T., Lorenz, C., Ostermann, J., 2010. Prediction framework for statistical respiratory motion modeling, in: *Medical Image Computing and Computer-Assisted Intervention - MICCAI 2010*.
- Knecht, S., Skali, H., O'Neill, M.D., Wright, M., Matsuo, S., Chaudhry, G.M., Haf-fajee, C.I., Nault, I., Gijssbers, G.H.M., Sacher, F., 2008. Computed tomography-fluoroscopy overlay evaluation during catheter ablation of left atrial arrhythmia. *Europace European Journal of Pacing Arrhythmias and Cardiac Electrophysiology* 10, 931–938.
- Kondermann, C., Mester, R., Garbe, C., 2008. A statistical confidence measure for optical flows, in: *Proceedings of the 10th European Conference on Computer Vision: Part III*, Springer-Verlag. pp. 290–301.
- Konno, K., Mead, J., 1967. Measurement of the separate volume changes of rib cage and abdomen during breathing. *Journal of Applied Physiology* 22, 407–422.
- Konukoglu, E., Glocker, B., Zikic, D., Criminisi, A., 2013. Neighbourhood approximation using randomized forests. *Medical Image Analysis* 17, 790–804.
- Kremkau, F.W., Taylor, K.J., 1986. Artifacts in ultrasound imaging. *Journal of Ultrasound in Medicine* 5, 227–237.
- Kuklisova-Murgasova, M., Cifor, A., Napolitano, R., Papageorgiou, A., Quaghebeur, G., Rutherford, M.A., Hajnal, J.V., Noble, J.A., Schnabel, J.A., 2013. Registration of 3D fetal neurosonography and MRI. *Medical Image Analysis* 17, 1137 – 1150.

- Lanfranco, A.R., Castellanos, A.E., Desai, J.P., Meyers, W., 2004. Robotic surgery. a current perspective. *Annals of Surgery* 239, 14–21.
- Larrabide, I., Omedas, P., Martelli, Y., Planes, X., Nieber, M., Moya, J., Butakoff, C., Sebastian, R., Camara, O., Craene, M.D., Bijmens, B., Frangi, A., 2009. GIMIAS: an open source framework for efficient development of research tools and clinical prototypes. *Functional Imaging and Modeling of the Heart*, ser. Lecture Notes in Computer Science 5528, 417–426.
- Linte, C., Lang, P., Rettmann, M., Cho, D., Holmes, D., Robb, R., Peters, T., 2012. Accuracy considerations in image-guided cardiac interventions: experience and lessons learned. *International Journal of Computer Assisted Radiology and Surgery* 7, 13–25.
- Linte, C., Moore, J., Peters, T., 2010. How accurate is accurate enough? A brief overview on accuracy considerations in image-guided cardiac interventions, in: *Engineering in Medicine and Biology Society (EMBC), 2010 Annual International Conference of the IEEE*, pp. 2313 –2316.
- Linte, C., Moore, J., Wiles, A., Wedlake, C., Peters, T., 2008. Virtual reality-enhanced ultrasound guidance: a novel technique for intracardiac interventions. *Computer Aided Surgery* 13, 82–94.
- Linte, C.A., Davenport, K.P., Cleary, K., Peters, C., Vosburgh, K.G., Navab, N., Edwards, P., Jannin, P., Peters, T.M., III, D.R.H., Robb, R.A., 2013. On mixed reality environments for minimally invasive therapy guidance: Systems architecture, successes and challenges in their implementation from laboratory to clinic. *Computerized Medical Imaging and Graphics* 37, 83 – 97.
- Low, D.A., Parikh, P.J., Lu, W., Dempsey, J.F., Wahab, S.H., Hubenschmid, J.P., Nystrom, M.M., Handoko, M., Bradley, J.D., 2005. Novel breathing motion model for radiotherapy. *International Journal of Radiation Oncology, Biology, Physics* 63, 921–929.
- Lu, W., Low, D.A., Parikh, P.J., Nystrom, M.M., Naqa, I.M.E., Wahab, S.H., Handoko, M., Fooshee, D., Bradley, J.D., 2005. Comparison of spirometry and abdominal

- height as four-dimensional computed tomography metrics in lung. *Medical Physics* 32, 2351–2357.
- Ma, Y., Penney, G.P., Bos, D., Frissen, P., Rinaldi, C.A., Razavi, R., Rhode, K.S., 2010. Hybrid echo and X-ray image guidance for cardiac catheterization procedures by using a robotic arm: a feasibility study. *Physics in Medicine and Biology* 55, N371.
- Ma, Y., Penney, G.P., Rinaldi, C.A., Cooklin, M., Razavi, R., Rhode, K.S., 2009. Echocardiography to magnetic resonance image registration for use in image-guided cardiac catheterization procedures. *Physics in Medicine and Biology* 54, 5039–5055.
- Manke, D., Nehrke, K., Bornert, P., 2003. Novel prospective respiratory motion correction approach for free-breathing coronary MR angiography using a patient-adapted affine motion model. *Magnetic Resonance in Medicine* 50, 122–131.
- Manke, D., Nehrke, K., Bornert, P., Rosch, P., Dossel, O., 2002a. Respiratory motion in coronary magnetic resonance angiography: A comparison of different motion models. *Journal of Magnetic Resonance Imaging* 15, 661–671.
- Manke, D., Rosch, P., Nehrke, K., Bornert, P., Dossel, O., 2002b. Model evaluation and calibration for prospective respiratory motion correction in coronary MR angiography based on 3-D image registration. *IEEE Transactions on Medical Imaging* 21, 1132–1141.
- Markelj, P., Tomazevic, D., Likar, B., Pernus, F., 2012. A review of 3D/2D registration methods for image-guided interventions. *Medical Image Analysis* 16, 642–661.
- Masamune, K., Fichtinger, G., Patriciu, A., Susil, R.C., Taylor, R.H., Kavoussi, L.R., Anderson, J.H., Sakuma, I., Dohi, T., Stoianovici, D., 2001. System for robotically assisted percutaneous procedures with computed tomography guidance. *Computer Aided Surgery* 6, 370–383.
- McClelland, J., Hawkes, D., Schaeffter, T., King, A., 2013. Respiratory motion models: A review. *Medical Image Analysis* 17, 19–42.
- McClelland, J.R., Blackall, J.M., Tarte, S., Chandler, A.C., Hughes, S., Ahmad, S., Landau, D.B., Hawkes, D.J., 2006. A continuous 4D motion model from multiple respiratory cycles for use in lung radiotherapy. *Medical Physics* 33, 3348–3358.

- McClelland, J.R., Chandler, A.G., Blackall, J.M., Ahmad, S., Landau, D.B., Hawkes, D.J., 2005. 4D motion models over the respiratory cycle for use in lung cancer radiotherapy planning, in: *Medical Imaging 2005: Visualization, Image-Guided Procedures and Display*.
- McClelland, J.R., Hughes, S., Modat, M., Qureshi, A., Ahmad, S., Landau, D.B., Ourselin, S., Hawkes, D.J., 2011. Inter-fraction variations in respiratory motion models. *Physics in Medicine and Biology* 56, 251–272.
- McGlashan, N., King, A.P., 2011. Capturing breathing motion variability using two signal motion models of the heart, in: *Proceedings of Medical Imaging Understanding and Analysis 2011*.
- McLeish, K., Hill, D.L.G., Atkinson, D., Blackall, J.M., Razavi, R., 2002. A study of the motion and deformation of the heart due to respiration. *IEEE Transactions on Medical Imaging* 21, 1142–1150.
- Metz, C., Baka, N., Kirisli, H., Schaap, M., Klein, S., Neefjes, L., Mollet, N., Lelieveldt, B., De Bruijne, M., Niessen, W., Van Walsum, T., 2012. Regression-based cardiac motion prediction from single-phase CTA. *IEEE Transactions on Medical Imaging* 31, 1311–1325.
- Moorthy, K., Munz, Y., Dosis, A., Hernandez, J., Martin, S., Bello, F., Rockall, T., Darzi, A., 2004. Dexterity enhancement with robotic surgery. *Surgical Endoscopy And Other Interventional Techniques* 18, 790–795.
- Nehrke, K., Bornert, P., Manke, D., Bock, J.C., 2001. Free-breathing cardiac MR imaging: Study of implications of respiratory motion - initial results. *Radiology* 220, 810–815.
- Noble, A.J., Boukerroui, D., 2006. Ultrasound image segmentation: A survey. *IEEE Transactions on Medical Imaging* 25, 987–1010.
- Noble, A.J., Navab, N., Becher, H., 2011. Ultrasonic image analysis and image-guided interventions. *Interface Focus* 1, 673–685.
- Orth, R.C., Wallace, M.J., Kuo, M.D., 2009. C-arm Cone-beam CT: General principles and technical considerations for use in interventional radiology. *Journal of Vascular and Interventional Radiology* 20, S538 – S544.

- Parthasarathy, V., Hatt, C., Stankovic, Z., Raval, A., Jain, A., 2011. Real-time 3D ultrasound guided interventional system for cardiac stem cell therapy with motion compensation, in: *Proceedings of the 14th International Conference on Medical Image Computing and Computer-Assisted Intervention - Volume Part I*.
- Pavani, S.K., Subramanian, N., Gupta, M., Annangi, P., Govind, S., Young, B., 2012. Quality metric for parasternal long axis B-mode echocardiograms, in: *Medical Image Computing and Computer-Assisted Intervention – MICCAI 2012*. Springer Berlin Heidelberg. volume 7511, pp. 478–485.
- Penney, G.P., Griffin, L.D., King, A.P., Hawkes, D.J., 2008. A novel framework for multi-modal intensity-based similarity measures based on internal similarity, in: *Proceedings of SPIE Medical Imaging*.
- Peressutti, D., Penney, G., Kolbitsch, C., Housden, R., Gomez, A., Rhode, K., King, A., 2013a. A framework for automatic model-driven 2D echocardiography acquisition for robust respiratory motion estimation in image-guided cardiac interventions, in: *Biomedical Imaging (ISBI), 2013 IEEE 10th International Symposium on*, pp. 29–32.
- Peressutti, D., Penney, G.P., Housden, R.J., Kolbitsch, C., Gomez, A., Rijkhorst, E.J., Barratt, D.C., Rhode, K.S., King, A.P., 2013b. A novel bayesian respiratory motion model to estimate and resolve uncertainty in image-guided cardiac interventions. *Medical Image Analysis* 17, 488–502.
- Peressutti, D., Penney, G.P., Kolbitsch, C., King, A.P., 2013c. Personalising cross-population respiratory motion models using anatomical features, in: *Proceedings of the 17th Conference on Medical Image Understanding and Analysis*.
- Peressutti, D., Rijkhorst, E.J., Barratt, D., Penney, G., King, A., 2012. Estimating and resolving uncertainty in cardiac respiratory motion modelling, in: *Biomedical Imaging (ISBI), 2012 9th IEEE International Symposium on*, pp. 262–265.
- Perrin, D.P., Vasilyev, N.V., Novotny, P., Stoll, J., Howe, R.D., Dupont, P.E., Salgo, I.S., del Nido, P.J., 2009. Image guided surgical interventions. *Current Problems in Surgery* 46, 730 – 766.
- Peters, T., Cleary, K. (Eds.), 2008. *Image-Guided Interventions. Technology and Applications*. Springer.

- Peters, T.M., 2006. Image-guidance for surgical procedures. *Physics in Medicine and Biology* 51, 505–540.
- Preiswerk, F., Arnold, P., Fasel, B., Cattin, P., 2012. Robust tumour tracking from 2D imaging using a population-based statistical motion model, in: *Mathematical Methods in Biomedical Image Analysis (MMBIA)*, 2012 IEEE Workshop on, pp. 209–214.
- Rao, A., Chandrashekara, R., Sanchez-Ortiz, G., Mohiaddin, R., Aljabar, P., Hajnal, J., Puri, B.K., Rueckert, D., 2004. Spatial transformation of motion and deformation fields using nonrigid registration. *IEEE Transactions on Medical Imaging* 23, 1065–1076.
- Rao, A., Sanchez-Ortiz, G., Chandrashekara, R., Lorenzo-Valdés, M., Mohiaddin, R., Rueckert, D., 2002. Comparison of cardiac motion across subjects using non-rigid registration, in: *Medical Image Computing and Computer-Assisted Intervention - MICCAI 2002*. Springer Berlin Heidelberg. volume 2488, pp. 722–729.
- Razavi, R., Hill, D.L., Keevil, S.F., Miquel, M.E., Muthurangu, V., Hegde, S., Rhode, K., Barnett, M., van Vaals, J., Hawkes, D.J., Baker, E., 2003. Cardiac catheterisation guided by MRI in children and adults with congenital heart disease. *The Lancet* 362, 1877 – 1882.
- Rhode, K., Hill, D., Edwards, P., Hipwell, J., Rueckert, D., Sanchez-Ortiz, G., Hegde, S., Rahunathan, V., Razavi, R., 2003. Registration and tracking to integrate X-ray and MR images in an XMR facility. *IEEE Transactions on Medical Imaging* 22, 1369–1378.
- Rhode, K., Ma, Y., Housden, J., Karim, R., Rinaldi, C., Cooklin, M., Gill, J., O'Neill, M., Schaeffter, T., Relan, J., Sermesant, M., Delingette, H., Ayache, N., Kruger, M., Schulze, W., Seemann, G., Dossel, O., Razavi, R., 2012. Clinical applications of image fusion for electrophysiology procedures, in: *Biomedical Imaging (ISBI)*, 2012 9th IEEE International Symposium on, pp. 1435–1438.
- Rhode, K., Sermesant, M., 2011. Modeling and registration for electrophysiology procedures based on three-dimensional imaging. *Current Cardiovascular Imaging Reports* 4, 116–126.



- Rhode, K.S., Sermesant, M., Brogan, D., Hegde, S., Hipwell, J., Lambiase, P., Rosenthal, E., Bucknall, C., Qureshi, S.A., Gill, J.S., Razavi, R., Hill, D.L.G., 2005. A system for real-time XMR guided cardiovascular intervention. *IEEE Transactions on Medical Imaging* 24, 1428–1440.
- Rijkhorst, E.J., Heanes, D., Odille, F., Hawkes, D., Barratt, D., 2010. Simulating dynamic ultrasound using MR-derived motion models to assess respiratory synchronisation for image-guided liver interventions, in: *Proceedings of the First international conference on Information Processing in Computer-Assisted Interventions*.
- Risholm, P., Janoos, F., Norton, I., Golby, A.J., III, W.M.W., 2013. Bayesian characterization of uncertainty in intra-subject non-rigid registration. *Medical Image Analysis* 17, 538–555.
- Risholm, P., Pieper, S., Samset, E., Wells, W. M., I., 2010a. Summarizing and visualizing uncertainty in non-rigid registration, in: *Medical Image Computing and Computer-Assisted Intervention – MICCAI 2010*. Springer Berlin Heidelberg. volume 6362 of *Lecture Notes in Computer Science*, pp. 554–561.
- Risholm, P., Samset, E., Wells, W., I., 2010b. Bayesian estimation of deformation and elastic parameters in non-rigid registration, in: *Biomedical Image Registration*. Springer Berlin Heidelberg. volume 6204, pp. 104–115.
- Rueckert, D., Frangi, A., Schnabel, J., 2003. Automatic construction of 3-D statistical deformation models of the brain using nonrigid registration. *Medical Imaging, IEEE Transactions on* 22, 1014–1025.
- Samei, G., Tanner, C., Székely, G., 2012. Predicting liver motion using exemplar models, in: *Abdominal Imaging. Computational and Clinical Applications*. Springer Berlin Heidelberg. volume 7601, pp. 147–157.
- Santelli, C., Nezafat, R., Goddu, B., Manning, W.J., Smink, J., Kozerke, S., Peters, D.C., 2011. Respiratory bellows revisited for motion compensation: preliminary experience for cardiovascular MR. *Magnetic Resonance in Medicine* 65, 1098–1103.

- Savill, F., Schaeffter, T., King, A., 2011. Assessment of input signal positioning for cardiac respiratory motion models during different breathing patterns, in: *Biomedical Imaging: From Nano to Macro*, 2011 IEEE International Symposium on, pp. 1698–1701.
- Schneider, M., Sundar, H., Liao, R., Hornegger, J., Xu, C., 2010. Model-based respiratory motion compensation for image-guided cardiac interventions, in: *Computer Vision and Pattern Recognition*, 2010 IEEE Conference on.
- Schweikard, A., Glosser, G., Bodduluri, M., Murphy, M.J., Adler, J.R., 2000. Robotic motion compensation for respiratory movement during radiosurgery. *Computer Aided Surgery* 5, 263–277.
- Scott, A.D., Keegan, J., Firmin, D.N., 2009. Motion in cardiovascular MR imaging. *Radiology* 250, 331–351.
- Seber, G.A.F., Lee, A.J., 2003. *Linear Regression Analysis*, 2nd edition. Wiley.
- Sharp, J.T., Goldberg, N.B., Druz, W.S., Danon, J., 1975. Relative contribution of rib cage and abdomen to breathing in normal subjects. *Journal of Applied Physiology* 39, 608–618.
- Shechter, G., Ozturk, C., Resar, J.R., McVeigh, E.R., 2004. Respiratory motion of the heart from free breathing coronary angiograms. *IEEE Transactions on Medical Imaging* 23, 1046–1056.
- Shechter, G., Shechter, B., Resar, J.R., Beyar, R., 2005. Prospective motion correction of X-ray images for coronary interventions. *IEEE Transactions on Medical Imaging* 24, 441–450.
- Simpson, I.J., Schnabel, J.A., Groves, A.R., Andersson, J.L., Woolrich, M.W., 2012. Probabilistic inference of regularisation in non-rigid registration. *NeuroImage* 59, 2438–2451.
- Sra, J., Narayan, G., Krum, D., Malloy, A., Cooley, R., Bhatia, A., Dhala, A., Blanck, Z., Nangia, V., Akhtar, M., 2007. Computed tomography-fluoroscopy image integration-guided catheter ablation of atrial fibrillation. *Journal of Cardiovascular Electrophysiology* 18, 409–414.

- Taron, M., Paragios, N., Jolly, M.P., 2005. Uncertainty-driven non-parametric knowledge-based segmentation : the corpus callosum case, in: IEEE Workshop on Variational and Level Set Methods in Computer Vision, pp. 1–24.
- Thijssen, J.M., 2003. Ultrasonic speckle formation, analysis and processing applied to tissue characterization. *Pattern Recognition Letters* 24, 659–675.
- Tobin, M.J., Chadha, T.S., Jenouri, G., Birch, S.J., Gazeroglu, H.B., Sackner, M.A., 1983. Breathing patterns. 1. Normal subjects. *Chest* 84, 202–205.
- Troyer, A.D., Estenne, M., 1984. Coordination between rib cage muscles and diaphragm during quiet breathing in humans. *Journal of Applied Physiology* 57, 899–906.
- Vellody, V.P., Nassery, M., Druz, W.S., Sharp, J.T., 1978. Effects of body position change on thoracoabdominal motion. *Journal of Applied Physiology: respiratory, environmental and exercise physiology.* 45, 581–589.
- Wang, Y., Riederer, S.J., Ehman, R.L., 1995. Respiratory motion of the heart: Kinematics and the implications for the spatial resolution in coronary imaging. *Magnetic Resonance in Medicine* 33, 713–719.
- Wein, W., Brunke, S., Khamene, A., Callstrom, M.R., Navab, N., 2008. Automatic CT-ultrasound registration for diagnostic imaging and image-guided intervention. *Medical Image Analysis* 12, 577 – 585.
- Wein, W., Camus, E., John, M., Diallo, M., Duong, C., Al-Ahmad, A., Fahrig, R., Khamene, A., Xu, C., 2009. Towards guidance of electrophysiological procedures with real-time 3D intracardiac echocardiography fusion to C-arm CT, in: *Medical Image Computing and Computer-Assisted Intervention - MICCAI 2009*.
- Wolz, R., Aljabar, P., Hajnal, J.V., Hammers, A., Rueckert, D., 2010. LEAP: Learning embeddings for atlas propagation. *NeuroImage* 49, 1316 – 1325.
- Yang, D., Lu, W., Low, D.A., Deasy, J.O., Hope, A.J., Naqa, I.E., 2008. 4D-CT motion estimation using deformable image registration and 5D respiratory motion modeling. *Medical Physics* 35, 4577–4590.

- Yao, C., Simpson, J.M., Schaeffter, T., Penney, G.P., 2011. Multi-view 3D echocardiography compounding based on feature consistency. *Physics in Medicine and Biology* 56, 6109.
- Yu, H., Fahrig, R., Pelc, N., 2005. Co-registration of X-ray and MR fields of view in a hybrid XMR system. *Journal of Magnetic Resonance Imaging* 22, 291–301.
- Yuen, S.G., Kesner, S.B., Vasilyev, N.V., Nido, P.J., Howe, R.D., 2008. 3D ultrasound-guided motion compensation system for beating heart mitral valve repair, in: *Proceedings of the 11th international conference on Medical Image Computing and Computer-Assisted Intervention*, pp. 711–719.
- Yuen, S.G., Kettler, D.T., Novotny, P.M., Plowes, R.D., Howe, R.D., 2009. Robotic motion compensation for beating heart intracardiac surgery. *The International Journal of Robotics Research* 28, 1355–1372.
- Zhang, Q., Pevsner, A., Hertanto, A., Hu, Y.C., Ling, C.C., Mageras, G.S., Rosenzweig, K.E., 2007. A patient-specific respiratory model of anatomical motion for radiation treatment planning. *Medical Physics* 34, 4772–4781.